FABRICATION OF THROUGH-HOLES FOR THE INTERCONNECTION OF POLYMER MICROFLUIDIC DEVICES

by

Juan Andres Gomez Ortega, M.S.

A dissertation submitted to the Graduate Council of
Texas State University in partial fulfillment
of the requirements for the degree of
Doctor of Philosophy
with a Major in Materials Science, Engineering, and Commercialization
December 2015

Committee Members:

Byoung Hee You, Chair

Tongdan Jin, Co-Chair

Yoo Jae Kim

Vedaraman Sriraman

In-Hyouk Song

COPYRIGHT

by

Juan Andres Gomez Ortega

2015

FAIR USE AND AUTHOR'S PERMISSION STATEMENT

Fair Use

Duplication Permission

ACKNOWLEDGEMENTS

Many people deserve my gratitude for their contribution to this research. I would like to start by offering my most sincere gratitude to my advisor, Dr. Byoung Hee You and co-advisor, Dr. Tongdan Jin, for their encouragement, assistance, and patience. They gave me the opportunity to develop the project that allowed me to shape my academic and professional career. It is with great appreciation that I acknowledge my dissertation committee members, Dr. Yoo Jae Kim, Dr. Vedaraman Sriraman, and Dr. In-Hyouk Song, for their advice and guidance throughout the development of this project.

I would like to express the deepest appreciation to my parents, Esperanza and Guillermo; my sister, Maria Angelica; and my cousins, Andrea, Malena, and Rosangela, for their support and care. All this would not have been possible without the support from the people I love the most.

I also want to acknowledge the Materials Science, Engineering, and Commercialization (MSEC) program, especially Dr. Thomas Myers, Dr. Jennifer Irvin, and Dr. Clois Powell who provided guidance and inspiration during my doctoral degree.

Finally, I would like to express my sincere gratitude to the following people for their encouragement and assistance: Shane Arabie, Ted Cera, Sean Moore, Chelsea Torres, Dr. Sooyeon Park, Devanda Lek, and Ash Kotwal.

TABLE OF CONTENTS

Page

LIST OF TABLES

Table **Page**

LIST OF FIGURES

Figure **Page**

LIST OF ABBREVIATIONS

Abbreviation	Description
C&L	Normalized Cockcroft & Latham Model
CAE	Computer-Aided Engineering
CDV	Critical Damage Value
CNC	Computer Numerical Control
COC	Cyclic Olein Copolymer
FEA	Finite Element Analysis
FEM	Finite Element Method
LOC	Lab-on-a-Chip
MEMS	Microelectromechanical Systems
PE	Polyethylene
PMMA	Polymethyl Methacrylate
POCD	Point of Care Diagnostics
PS	Polystyrene
PSU	Polysulfone
S/N Ratio	Signal-to-noise Ratio
T_g	Glass Transition Temperature
T_d	Demolding Temperature

ABSTRACT

In the past decade, there has been an increasing interest in the implementation of microfluidic devices such as, Lab-on-a-Chip (LOC). The ability to interconnect microfluidic devices would scale the functionality of modular systems, thus fulfilling the gap between research and the consumer market. Therefore, replication technology is a critical feature in turning expensive microstructures into cost effective polymer devices. Hot embossing has been proposed in the fabrication of through-holes. This would allow a fluidic sample to be transferred between multiple interconnected Point-of-Care diagnostics (POCD) systems. The hot embossing process was modified to increase the durability of a mold insert by using a Polysulfone (PSU) buffer layer to reduce the potential wear. This buffer acted as a residual layer receptor by removing it from the polymer during molding. Through-hole fabrication could be analyzed via Finite Element Analysis (FEA) to determine the appropriate process parameters to achieve high replication quality. FEA was used to investigate the process parameters and their effects on molded patterns. Experimental testing was used concurrently with simulation results to determine the accuracy of the numerical model. The results of experiments as well as the numerical model showed the proper combination of parameters, making it viable for a production process. Therefore, understanding the effect of process parameters could be applied in the development of through-hole manufacturing tools. Compared to previous fabrication techniques, this process of hot embossing

does not require alignment tools and introduces the capability of simultaneous through-hole fabrication.

1. INTRODUCTION

1.1. Motivation

Through-hole fabrication has been a technical challenge since the initial description of the hot embossing process for the manufacturing of microfluidic devices (Chuo et al. 2013). Through-holes can be rapidly fabricated on a millimeter scale using conventional processes due to the machinability of the polymer substrates. However, fabricating through-holes at a microscale is a complex process as a result of the polymer flow behavior (Zhu et al. 2011). Several techniques have been investigated for the fabrication of through-holes such as mechanical drilling, punching, and laser ablation. Mechanical drilling is a common technique used to fabricate through-holes with a constant diameter. The minimum diameter available in some commercial drilling tools reaches 50 μm (Horng et al. 2005). However, mechanical drilling requires extended periods of time and additional equipment for the fabrication process. Punching has been used in various materials including polymers and metals due to their flexible capabilities (Pan et al. 2008; Joo et al., 2005; Joo et al., 2001). Laser ablation is directly related to the size and energy of the laser. Commercial lasers can fabricate through-holes with a minimum diameter of 10 μm and a maximum of 120 μm (Joudkazis. Et al., 2004; Dyer et al., 1997). These techniques need further improvements for mass fabrication. Otherwise, it is difficult for mechanical and laser drilling to fabricate through-holes simultaneously.

Hot embossing is a promising low-cost, medium to high-volume manufacturing technology that provides several advantages such as process simplicity and mold

exchange along with high replication accuracy for polymer microstructures (Gomez et al. 2014). One of the main challenges of through-hole fabrication via hot embossing is the removal of a residual layer that remains at the bottom of the polymer substrate, without affecting the structure of the mold pins (Gurung et al. 2007). The residual layer could be removed using fly cutting to open interconnecting holes, thus removing a layer thicker than the residual layer (Juang et al. 2002). The technique presented by Gurung (2007) introduced the ability to fabricate simultaneous through-holes. However, it required post-hot embossing processing which could make it not suitable for mass fabrication volumes.

Analysis of the flow behavior of molten polymer has been widely used in the fabrication of microfluidic devices via hot embossing (Gomez et al. 2012; He et al. 2007; Juang et al. 2002; Yao et al. 2002). Numerical analysis was used to understand the flow behavior of the polymer substrate during the filling process of the mold cavity (He et al. 2007; Juang et al. 2002; Yao et al. 2002). The effect of individual process parameters on the mold filling could be analyzed through parametric studies (Gomez et al. 2012; Chun et al. 2012). Process parameters such as molding temperature, mold displacement, embossing force, and holding time directly affect the advance of flow front of the polymer substrate to fill the mold cavity during molding (Yao et al. 2005; Juang et al. 2002; Heyderman et al. 2000). Understanding the flow behavior might give an insight in the selection of the process parameters. The effects of the process parameters during mold filling can be analyzed for the design and development of manufacturing processes. Process parameters can be controlled to achieve high replication quality by assuring a

complete filling of the mold cavity. Thus, understanding the polymer flow behavior could be used as a stepping-stone in the development of a through-hole manufacturing tool in hot embossing.

1.2. Statement of the problem.

The problem of the present study was to analyze the effect of the process parameters including molding temperature, embossing force, and the thickness of the polymer on the fabrication of through-hole sin hot embossing. Hot embossing experiments and FEA were used to analyze the effect of the process parameters on the polymer substrate.

1.3. Statement of the purpose

The purpose of the present study was to develop information, specifically on the process parameters for the fabrication of through-holes in hot embossing, which could be utilized for the development of through-hole fabrication processes as an alternative to post-processing techniques. Compared to previous hot embossing processes, this technique requires no alignment tools, which facilitates the manufacturing process, and introduces the capability of simultaneous through-hole fabrication in a single-operation process

1.4. Statement of the objective

The objective of this study was to analyze the process parameters required for the reliable fabrication of through-holes in hot embossing via FEA and hot embossing experiments. The following factors were investigated:

- Molding temperature
- Embossing force

- Thickness of the polymer layer

1.5. Outline of the dissertation

A general introduction about the study will be presented in Chapter 1 along with its contribution and objectives. Chapter 2 covers a literature review on previous studies about the hot embossing process, experimental analysis, and finite element models. Numerical analysis using Finite Element Method (FEM) software DEFORM 2D (Scientific Forming Technologies Corp., Columbus, OH) will be included in Chapter 3. Boundary conditions, material properties, governing equations, and assumptions and limitations of the numerical model are discussed in this chapter. In Chapter 4, through-hole fabrication via hot embossing experiments will be discussed. Mold design and fabrication, material properties, and process parameters will be covered in this chapter. In Chapter 5, a correlation between experimental and simulation results is performed to determine the validity of the numerical analysis. The market opportunity of this study, which includes the target market and a business summary is presented in Chapter 6. A summary of the study along with future work recommendations and conclusions are listed in Chapter 7.

2. LITERATURE REVIEW

2.1. Introduction

The interconnection of microfluidic devices is one of the critical components in microelectromechanical systems (MEMS) for the development of point-of-care diagnostic systems, bio-chips, and light-emitting devices. Interconnecting ports on a millimeter scale can be easily fabricated by high quality conventional techniques, due to the high machinability of polymer materials (Li et al., 2013). However, the fabrication of interconnecting through-holes at the microscale has become an important challenge, increasing the research interest over the past years. Through-holes can be fabricated using post-processing techniques, including mechanical drilling, punching, and laser ablation. Mechanical drilling is often limited by the diameter of the drill bit, requiring extended cycle times and additional equipment. Punching has been used on various materials including polymers and metals due to their flexible capabilities. However, ensuring a highly accurate straight motion and effective tool alignment is a critical challenge. Laser ablation is directly related to the diameter and intensity of the laser beam.

There has been increasing interest in the fabrication of interconnecting ports without the need of additional post-processing and alignment methods (Taylor et al., 2011). Hot embossing offers the possibility to fabricate through-holes for the interconnection of polymer microfluidic devices in a single-operation process. Micro-molding techniques for such as hot embossing are considered to be appropriate manufacturing processes to achieve these requirements. Hot embossing is a low-cost, low to medium-volume manufacturing technology that

provides several advantages including process simplicity and mold exchange along with high replication accuracy for polymer microstructures (Gomez et al., 2014). One of the main challenges in the fabrication of interconnecting through-holes for microfluidic devices is the removal of the residual layer, in contact with the polymer substrate, without affecting the mold pins. Although, hot embossing is a low-cost manufacturing technique, it may require extensive testing for the selection of the proper process parameters and mold insert. To reduce testing, Computer Aided Engineering (CAE) has been applied to investigate the effect of process parameters in molded patterns.

By utilizing finite element simulations, a process can be studied repeatedly with different combinations of process parameters reducing the amount of experimental testing (Gomez et al., 2012; He et al., 2007; Yao et al., 2005; Juang et al., 2002). Two-dimensional and three-dimensional finite element models have been used to understand the flow behavior of a polymer substrate during the molding process combining the effect of thermal stress and sidewall friction (He et al., 2007; Yao et al., 2005; Juang et al., 2002). Process parameters such as molding temperature, mold displacement, embossing force, and holding time directly affect the behavior of the polymer substrate (Yao et al., 2005; Juang et al., 2002; Heyderman et al., 2000). The effect of individual process parameters during mold filling could be analyzed through parametric studies to validate simulation results (Chun et al. 2012; Gomez et al. 2012). These results could be used to support the design and development of manufacturing processes. Therefore, understanding the polymer

flow behavior could be used as a stepping-stone in the development for interconnecting ports in polymer microfluidic devices.

2.2. The hot embossing process

Hot embossing is a manufacturing technology used to transfer features from a mold insert into a polymer substrate. It has been widely used to fabricate polymer microstructures where high precision and quality are important (Dirckx et al. 2011; Luo et al. 2006; Heckele et al. 2004). Simplicity of mold exchange, manufacturing flexibility for different substrates, high replication quality, and low temperature cycles are typical advantages of hot embossing, compared with micro-injection molding, as well as replicating delicate microstructures with a higher aspect ratio due to its low material flow and low flow rates, which reduces internal stress (Dirckx et al. 2011; Park et al. 2009; Worgull et al. 2009; Song et al. 2008; Luo et al. 2006; Heckele et al. 1998) It is well suited for low and medium-volume production due to long cycle times.

Typical components of a hot embossing equipment, presented in Figure 2.1, include a mold insert containing the pattern design needed to transfer, heating and cooling units, a press unit in charge of the molding force and relative mold displacement, and the control unit with a user interface to enter the process parameters. In the case of one-sided hot embossing a plate is located opposite to the mold, called the substrate plate. (Worgull et al. 2009; Worgull et al. 2006; Heckele et al. 1998)

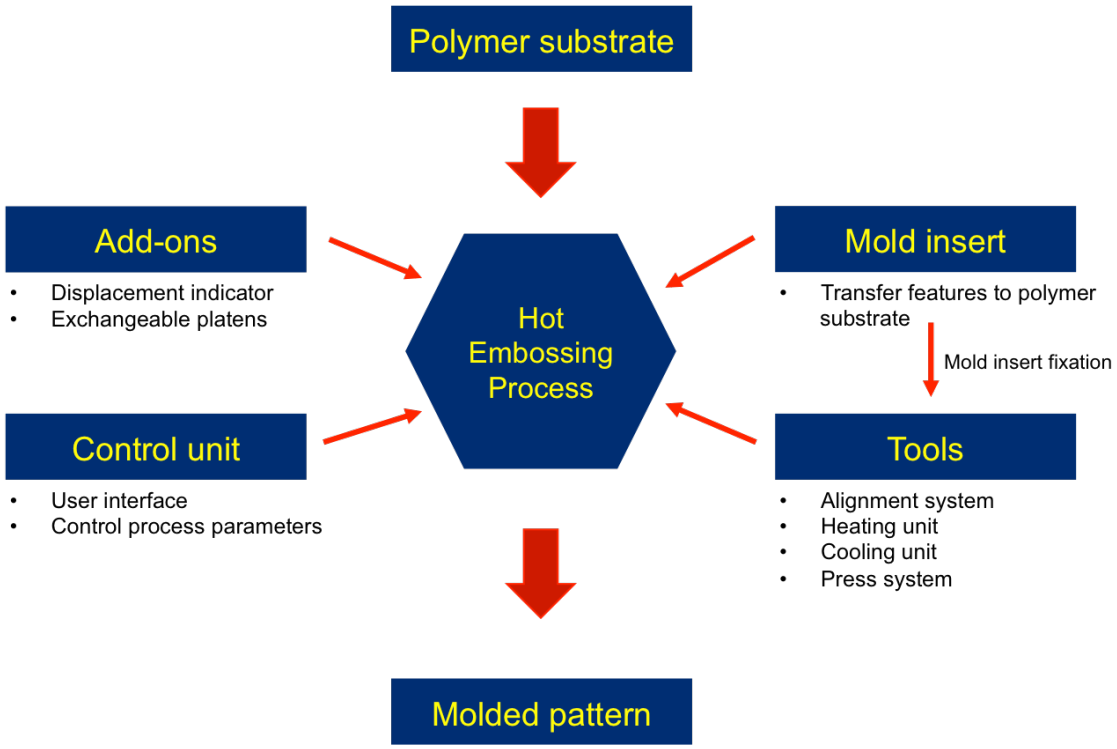

Figure 2.1. Schematic representation of the typical components of a hot embossing system including Machine, control unit, mold insert, tools, and a polymer substrate.

Hot embossing can be divided into three steps including embossing, cooling, and demolding as illustrated in Figure 2.2 (Gomez et al. 2014; Song et al. 2008; Heckele et al. 2004; Juang et al. 2002; Heyderman et al. 2000). During the first step, the mold and the substrate plate are heated up to a temperature above the T_g of the polymer substrate. Once the temperature is reached, the substrate plate moves towards the mold insert until making contact, and the embossing force is reached (Li et al., 2008). The embossing force will be maintained constant for a period of time defined as the holding time, as illustrated by the diagram in Figure 2.3 (Worgull et al. 2009; Heckele et al. 1998).

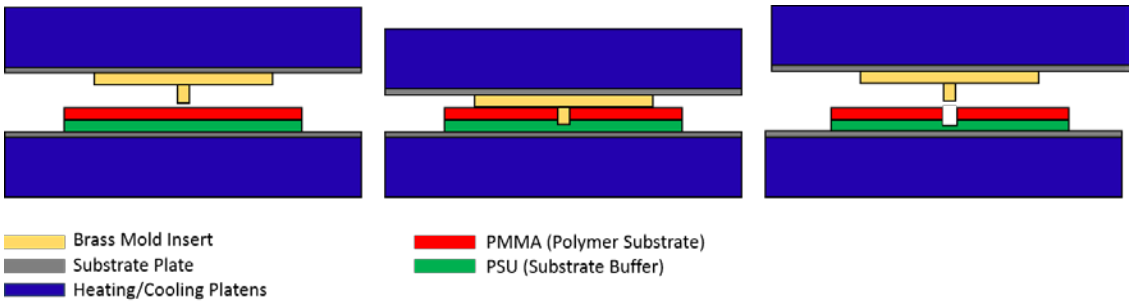

(a) (b) (c)

Figure 2.2. The hot embossing process: (a) embossing, (b) cooling, and (d) demolding. The process is characterized by the adhesion generated between the polymer substrate and the lower platen allowing vertical demolding.

During the holding time, the polymer substrate flows in a radial direction and the residual layer thickness is reduced due to the embossing force (Jin et al. 2009; You et al. 2009; Worgull et al. 2006). The mold insert and the substrate plate will continue to move closer, as the thickness of the residual layer decreases, to maintain constant embossing force. Temperature remains constant during the embossing step, as any variations in temperature could affect the fluidic resistance of the polymer substrate resulting in product defects (He et al. 2007; Yao et al. 2005; Juang et al. 2002; Juang et al. 2002). Upon the end of the holding time, cooling of the hot embossing system initiates. The temperature of the mold insert and the substrate plate is allowed to drop below T_g under constant pressure.

Embossing force should be maintained constant during cooling to avoid the formation of pattern defects. The higher thermal shrinkage rate of the polymer substrate, compared to the mold insert generates thermal stress at the interfacial layers of the polymer and the mold (Jin et al. 2009; Worgull et al. 2006).

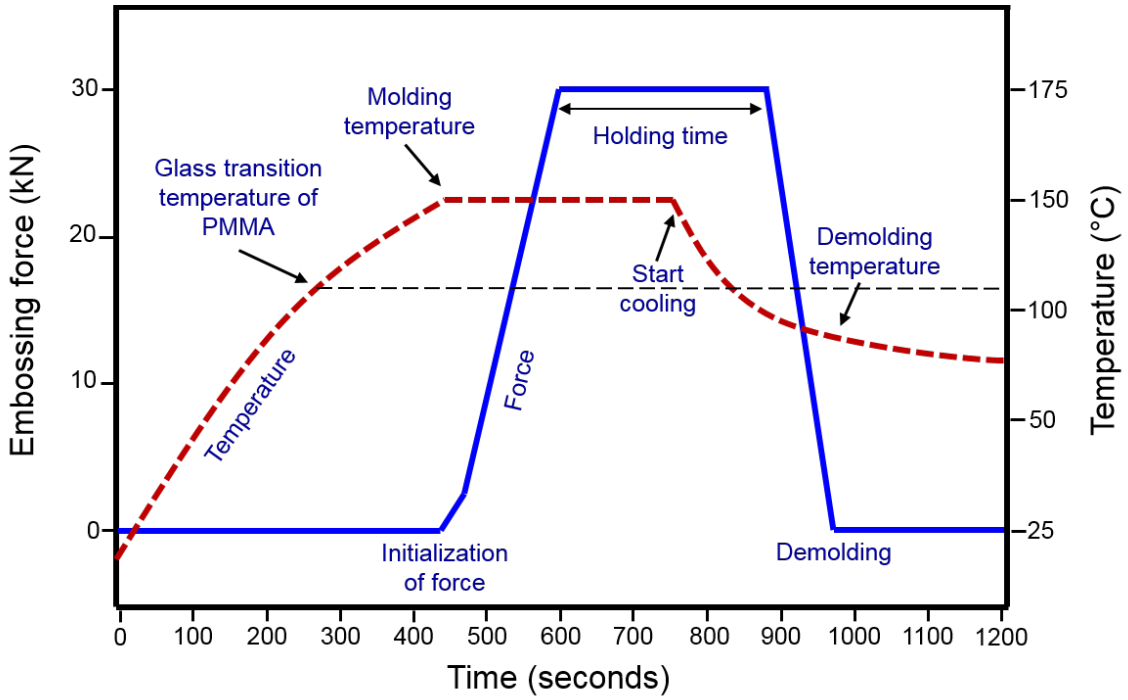

Figure 2.3. Representation of the process parameters embossing force, time, and molding temperature in hot embossing.

When the demolding temperature is reached, the molded substrate is separated from the mold by the relative displacement of the mold and the substrate plate. Demolding forces can damage molded patterns. Therefore, minimizing its effect is another critical aspect to fabricate reliable polymer microstructures (Jin et al. 2009; You et al. 2009; Song et al. 2008; Young et al. 2005). Complete cavity filling is a critical aspect to achieve high replication fidelity in a molded pattern.

Cooling of a molded pattern is a critical step for the reliable fabrication of polymer microstructures (Matthew et al., 2011; Song et al., 2008; Jeong et al., 2002). Most of the defects could be attributed to the cooling or demolding steps (Song et al., 2008; Guo et al., 2007; Jeong et al., 2002). Typical cooling defects include distorted, deformed, and broken microstructures. The shrinkage of the

polymer substrate during cooling induces thermal stress in the molded patterns. Thermally induced mechanical stress is a principal contributor for defects (Song et al., 2008; Worgull et al., 2008; Schift et al., 2001).

Demolding can be achieved due to the adhesion force of the polymer substrate to the substrate plate, this force is transferred homogeneously and vertical to the molded part (Jin et al. 2009; You et al., 2009). An important aspect of the molding step is the behavior of the molten polymer substrate (Worgull et al., 2006). Some analyses have been performed to describe the flow behavior of the molten polymer in hot embossing (Guo et al., 2006).

2.3. Theoretical models

Analysis of the flow behavior of molten polymer has been widely studied in the fabrication of microdevices using hot embossing. Numerical analysis can be used to understand the flow behavior of the polymer substrate during the hot embossing process. The effect of individual process parameters can be investigated through parametric studies. The appropriate process parameters can be selected to ensure the fabrication of complete through-holes in hot embossing.

The plastic response of PMMA was analyzed using a tensile test. PMMA was almost rubbery below the glass transition temperature and was hardened with large strains as the temperature increases (G'Sell et al. 1997). Juang and Yao used the developed material properties of PMMA. Flow front of the polymer substrate and the flow stress was simulated and compared with experimental results to validate the proper gate location for a needle cover. Results showed that higher temperatures were recommended to achieve successful molding. Injecting

the polymer substrate for extended periods, 1.2 seconds, lead to a significant increase in flow stress (Chun et al. 2012). Flow behavior parameters such as pressure and temperature were obtained by analyzing the residual stress in the mold cavity and the residual stress distribution in the injection-molded product. The layer-removal method was used to calculate the residual stress distribution of the molded structure. Results were used as input data of the numerical stress analysis to calculate a more accurate gap-wise temperature field (Kwon et al. 2001). Worgull et al. (2004) proposed a reliable computer model and numerical analysis tool to study the process parameters on the hot embossing process. Hot embossing was divided into molding and demolding which were analyzed separately. For the molding step, finite element software MOLDFLOW (Autodesk, San Rafael, CA) was used to analyze the flow behavior in a hot embossing cycle. For demolding, ANSYS (ANSYS, Inc. Cecil Township, PA) was applied (Worgull et al. 2004). Results demonstrated that the process parameters, calculated in the numerical analysis, showed an improvement in the quality of the molded patterns.

Numerical models for hot embossing were developed by Gomez et al. (2014) to analyze the advance of the flow front of the molten polymer using commercial software DEFORM-2D. Simulation results were correlated with hot embossing experiments to validate the feasibility of the numerical models. A hemisphere tipped post, used as an alignment structure in the assembly of micro devices (Gomez et al. 2012; You et al. 2009; Song et al. 2008), was modeled to demonstrate the flow behavior of the molten polymer during cavity filling. Most of the simulations showed agreement with experiments. The mold filling was

estimated with the heights of the embossed posts in the analysis. No significant mold filling with the molten polymer was observed below the glass transition temperature of 105°C. The mold cavity was completely filled with the polymer at the molding temperatures of 137.5°C and 150°C while the embossing forces were 300, 600, and 900 N. The molding temperature significantly affected the advance of the flow front of the polymer substrate during molding. It showed that the proper process parameters can be selected by analyzing the flow behavior of the molten polymer during mold filling. The developed models were applicable to the design of a micro hot embossing process (Gomez et al. 2014).

A theoretical model was introduced to compute the required embossing time to fill a micro square cavity with polymer (Heyderman et al. 2000). The analysis was based on a simple two-dimensional squeeze flow theory of polymers to determine the embossing time required to completely fill a defined geometry. The study reflected a hydrostatic pressure applied on the polymer in the numerical analysis. The model was not expanded to the mold filling with complicated mold geometrics. Juang et al. (2002) studied the flow behavior of polymers in both isothermal and non-isothermal embossing using a commercial finite element simulation code, DEFORM-2D (Juang et al. 2002). During non-isothermal embossing, the polymer flowed along the sidewall of the mold until it reached the top of the mold cavity. The predicted flow patterns of isothermal embossing agreed with the experimental results, but simulations did not consider the effect of backup pressure on the polymer due to an air entrapment the software was not able to simulate. A weld line appeared in non-isothermal embossing due to the collision of two molten and

solidified layers. The study concluded that besides process parameters and material properties, heat transfer plays an important role in non-isothermal hot embossing.

Numerical analyses of non-isothermal embossing were performed by Yao et al., (2005). A commercial finite element simulation code, MARC (MSC Software Co.) was used to analyze the plane strain model (Yao et al. 2005). The advance of the flow front of PMMA was correlated with the ratio of heat transfer from the mold cavity to the polymer substrate, while the depth of the cavities varied from 200 to 0.5 μm. Simulation results reported uniform and non-uniform flow patterns depending on the depth of the microcavities, which also had a major effect on heat diffusion. Hot embossing experiments and numerical simulations were used to analyze the flow behavior of PMMA in isothermal hot embossing (He et al. 2007; Heyderman et al. 2000) the numerical analysis showed the effect of the number of cavities, distance between cavities, and surface tension of PMMA. Hot embossing experiments consisted of isothermal hot embossing at 130°C and constant values of pressure and a vacuum. Holding times of 10s, 20s, 30s, 1min, 2min, 3min, and 5min were used to observe flow behavior and capillary effects, where typical flow characteristics were determined. At the first moment, the polymer flows in the upward direction along the sidewall of the mold cavity followed by the center in the mod cavity. The predicted flow behavior was verified by showing the advance of flow front. Finite element analysis was performed using Computational Fluid Dynamics (CFD) code Flow-3D (Flow Science, Inc., Leland, North Carolina). Plane strain simulations with cavity ratios of depth and width between 0.5 and 200,

holding time of 6 min, and temperatures between 190 and 230°C were included in the analysis. In the analyses, polymers flowed up along the side wall first.

Young (2005) developed a numerical tool to predict polymer flow behavior based on a viscous model using Polystyrene (PS) as polymer substrate (Young et al. 2005). The first approach analyzed the molding process of a single feature. The dimensions of the feature were: 100 nm width and 500 nm height. Isothermal embossing was simulated at 160 and 180°C. Results demonstrated that flow behavior was relatively similar to the experimental observations made by Juang et al. (2002) and Yao et al., (2005). A second study was developed to analyze the polymer flow and cavity filling behavior in multi-feature imprint patterns. Pattern distances varied from 200 to 900 nm. High-pressure points were located around the embossed pattern. While the mold insert is compressing the polymer substrate, a significant increase in pressure was observed due to the existence of large polymer flow in the planar direction. As expected, the embossing pressure is higher at lower temperatures. Filling capacity of the polymer will depend on the cavity thickness and height (Yao et al. 2005; Young et al. 2005; Juang et al. 2002). Isothermal hot embossing was analyzed to estimate the height of molded polymers with concave and convex features to improve product quality. The numerical analysis was performed to study the embossing, cooling, and demolding steps in hot embossing. DEFORM-2D was used to analyze the hot embossing process (He et al. 2007). The heights were evaluated with the movement of the flow front of PMMA as functions of embossing time and the location of features from a center of the mold. The hot embossing process was optimized, and an automatic

demolding device was proposed based on the results obtained from the numerical analysis.

Luo et al. (2006) studied the effect of embossing time on the viscoelastic behavior of PMMA during mold filling. The time dependence of a strain of PMMA was obtained from creep experiment, and it was coupled with numerical models using third order polynomial and first order exponential decay models. The mechanical properties of PMMA were characterized by creep curves and numerical fitting. The results of this study demonstrated that the first order exponential decay was the most accurate model, compared to the polynomial model, to predict the flow behavior of the polymer substrate.

A FEM model was proposed to characterize the flow behavior and recovery, the effects on stamp geometry, shear thinning, and imprinted speed of a polymer substrate (Jin et al. 2009). PMMA was defined as a non-Newtonian fluid during mold filling and a linear-elastic solid during demolding. The proposed model allowed the simulation to predict polymer recovery after demolding. Results showed that deformation depends on the cavity ratio width to height, the cavity ratio width to tool width and the temperature influence of embossing speed. Deformation followed different polymer behaviors, single and dual peaks. The recovery of the polymer substrate, obtained from the simulations, was correlated with hot embossing experiments resulting in a pattern depth error of 4%. The stress evolution of a polymer substrate was analyzed in isothermal hot embossing, while the mold had several geometries including a duty ratio, aspect ratio, width to thickness ratios, and cavity locations (Zhang et al. 2011). A stress barrier was

proposed to reduce the defects of replicated structures. The small ratio and high aspect ratio of the mold cavity significantly contributed to the stress concentration developed at the bottom edge of the replicated structure.

Thermal shrinkage and adhesion forces were analyzed by FEM to decrease the thermal stress of molded structures (Guo et al. 2007). The deformation of microstructures typically occurred during both the cooling and demolding steps. Demolding and cooling forces mainly consist of thermal shrinkage, thermal stress, adhesion, and sidewall friction. Numerical simulations estimated the friction force generated by adhesion and thermal stress (Guo et al. 2007; Song et al. 2008). Thermal stress was correlated with the geometry of the mold cavity. Auxiliary structures were suggested as thermal stress barriers to increase the replication accuracy of the molded pattern by protecting the molded pattern from converging stress (Worgull et al. 2006; Farschian et al. 2012). The effect of demolding an embossed microstructure was investigated by Drickx et al. (2009) to analyze the relation between pattern geometry, material properties, and process parameters in the replication accuracy of the demolded pattern. Similar finite element simulations by Song et al. (2008) and Park et al. (2009) were developed. It was found that both adhesion and sidewall friction play a critical role during demolding. Adhesion was reduced by thermals stress while sidewall friction increased as the polymer substrate cooled down.

2.4. Fabrication of through-holes

Passive alignment was proposed by Gurung (2007) as a design for vertically stacking microfluidic devices. The interconnection ports were made by through-

holes with diameters from 100 µm to 500 µm, thus an alignment better than 100 µm was required. Blind holes were fabricated via hot embossing leaving a residual layer. The residual layer was removed by fly cutting the chip to cut off the excess of polymer until the desired thickness was reached. The embossed patterns used for passive alignment were v-grooves and dowel pins embossed at the sidewalls of the pins and fixed to the base of the substrate, respectively (Gurung et al. 2007). Results showed a mean accuracy of 40 µm and repeatability of 60 µm. The alignment accuracy of the system was directly related with the number of contacts instead of the tolerances at each contact (You et al. 2009; Heckele et al. 2004). Low-density polyethylene (PE) was used as a polymer substrate in the fabrication of through-hole microarrays. The mold insert was fabricated by anisotropic etching of KOH in silicon wafers via standard photolithographic methods, such as reactive ion etching and exposure of protective layers (Chou et al. 2013). To protect the mold pins, an elastomer rubber with a durometer of 75 A, was used. Results showed that the methodology described to fabricate tapered, through-holes polymer devices achieved high replication accuracy. However, the technique presented was not cost effective, hence not feasible for mass production.

Through-hole fabrication by using the hot embossing process and a subsequent indentation process to remove the residual layer was discussed by Zhu and Cui (2011). PMMA sheets were placed on an Aluminum alloy buffer which was used to reduce damage to the pins. A stainless steel mold with an array of pins was used to fabricate blind holes, creating a thin residual layer. PMMA sheets were molded at 190ºC and an embossing force of 30 kN. The molding temperature

of 190ºC is above the T_g of PMMA, allowing it to become a viscous fluid. A metal frame was used to prevent polymer from escaping due to the reduced fluidic resistance of the polymer substrate. The subsequent indention process would complete the through hole by creating indents on the aluminum alloy buffer. The pins were pressed so that it contacted the aluminum alloy buffer material at the molding temperature. A hard-hitting squeeze and friction between pins and the indent sidewalls generated force to cut through the residual layer (Zhu et al. 2011). Time and molding force were analyzed to determine the optimal indention parameters. The process allowed the fabrication of an array of through holes with diameters from 100 μm to 1.0 mm.

Through-hole fabrication by a standard mechanical punching process was scaled down to produce 25 μm holes (Joo et al. 2005; Joo et al. 2001). The methodology discussed required the design and assembly of a micro punching tool able to meet the requirements of process accuracy for through-holes. Results were analyzed based on quality in relation with shear fracture behavior. Fabrication results presented that mechanical punching was capable of producing high quality through-holes at the micrometer scale (Pan et al. 2008; Joo et al. 2005; Joo et al. 2001). As the diameter of the through-hole was reduced fracture depth diminished and burnish depth became dominant. However, the mechanical punching process was presented as a post-processing technique not capable of simultaneous through-hole punching. A similar micro-punching system for the fabrication of thought-holes was developed by Xu et al. (2012). A punching system guided by double linear motors was developed for automatic micro-punching. The system

was driven by an electric linear motor that provided high speed, high acceleration, high precision, and free force and motion Results showed that through-holes fabricated with diameters of 600, 300, and 150 μm achieved high dimensional accuracy (Xu et al. 2012).

Werner (2005) developed a tool for fabricating through holes in cyclo-olefine copolymer (COC) in double-sided hot embossing as an initial approach of integrating through-hole fabrication during the molding step. Mold insert alignment was performed with the aid of two guided pins, which were effective for the fabrication of holes with a diameter of 200 μm. Results indicated the presence of a residual layer after demolding the samples. Several techniques were proposed to remove the residual layer including the application of high-pressure air to blow off the residual layer, applying vacuum to the hot embossing process, or removing the residual layer by penetrating a secondary pin into the blind hole after demolding (Werner et al. 2005).

3. HOT EMBOSSING SIMULATIONS

3.1. Introduction

Numerical simulations were performed to study the mechanical and thermal stress distribution during molding, cooling, and demolding. Mechanical and thermal stress play an important role in the fabrication of polymer interconnects. Excessive stress concentrations can reduce the replication accuracy of the structure generating defects (Song et al., 2008). Numerical models were developed to produce a simulation tool to investigate the stress distribution on the molded pattern by studying the process parameters. The development of a simulation tool could decrease the cost of re-engineering, and provide an in-depth understanding of the behavior of the polymer in the fabrication process.

The fabrication of polymer interconnects for micro fluidic devices could be analyzed via FEM to determine the appropriate process parameters. This may lead to a reliable replication of polymer microstructures. Commercially available finite element software have become a popular approach for process design and development (Yao et al., 2005). This can significantly increase the reliability of hot embossing by analyzing the polymer flow behavior in the simulation.

In this chapter, a commercial simulation code, DEFORM 2D (Scientific Forming Technologies Corp., Columbus, OH), was used to perform the simulations for the fabrication of polymer interconnects. Molding, cooling, and demolding were modeled independently to reduce calculation time. The boundary conditions were defined for each step, as well as the simulation conditions.

3.2. Flow stress and deformation behavior

DEFORM 2D has been widely used to study the behavior of a polymer substrate throughout the hot embossing process (Gomez et al., 2014; Heckele and Schomburg, 2004). Flow stress was defined as the relation between stress and strain under constant strain rates. The viscoplasticity of the polymer was expressed using material properties from previous studies (Juang et al., 2002; G'Sell and Souahi, 1997).

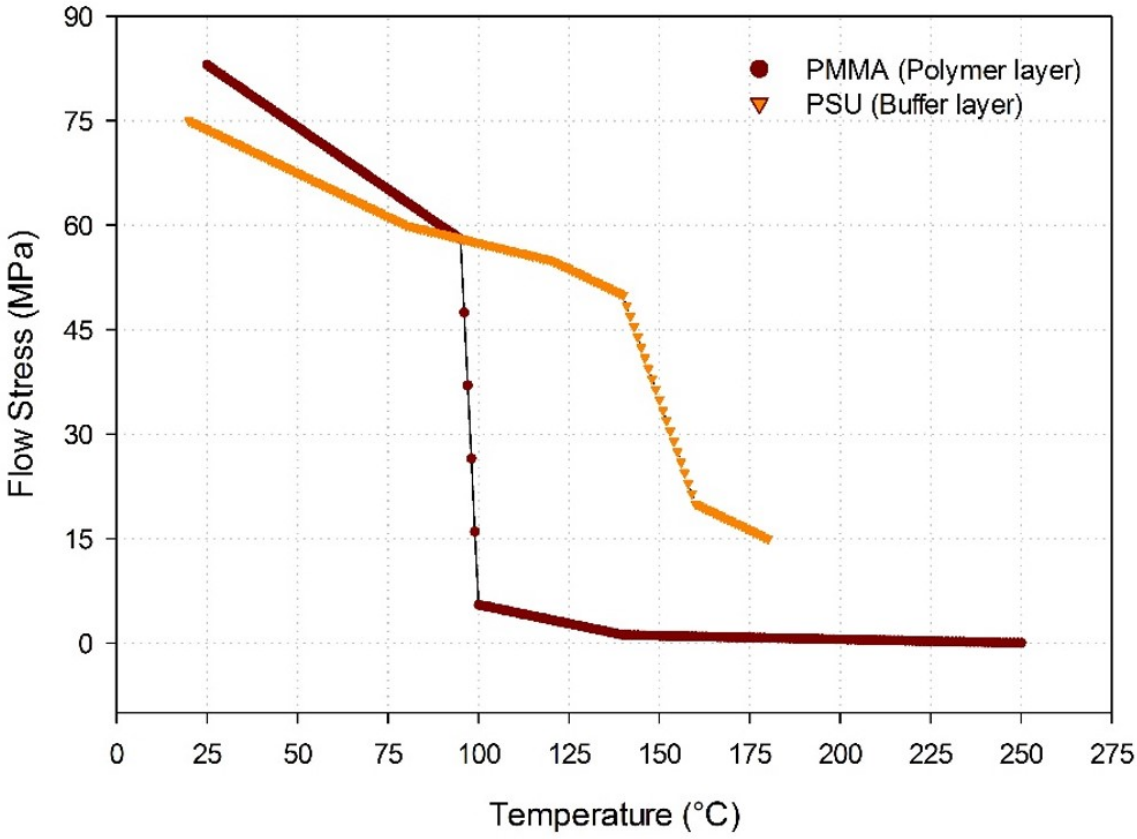

Figure 3.1. The flow stress-substrate temperature relation for PMMA and PSU was determined by experimental data obtained from Juang et al. (2002).

Experimental data was used to correlate the temperature change and the strain rate of the polymer substrate to generate the flow stress equation (Juang et al., 2002). The flow stress-polymer temperature relationship was defined by a segmented linearization obtained from experimental data, as shown in Figure 3.1. The flow stress for PMMA was obtained for the experiments made by Juang et al. (2002). Data for PSU was obtained from the data sheet provided by the manufacturer (Colorcomp™, Sabic plastics, Shanghai, China).

3.3. Heat transfer

Heat transfer between the boundaries of the polymer, the mold insert, and the aluminum plate were modeled using the thermal inter-object model in DEFORM 2D. The thermal inter-object definition establishes how the objects in the simulation interact with each other. Thermal conductivity in the analysis was defined in Equation 3.1. (SFTC, 2014). The model establishes the heat transfer rate between objects in thermal contact:

$$q_{cond} = -C_{cond}\frac{\partial T}{\partial X} \tag{3.1}$$

where q_{cond} is the heat flux generated by conduction, C_{cond} is the thermal conductivity coefficient, and $\frac{\partial T}{\partial X}$ is the temperature gradient.

The effect of heat transfer between the environment and the polymer substrate was defined as convection, as presented in Equation 3.2 (SFTC, 2014). The model establishes convective-cooling as the heat transfer relative to the difference in temperature between the polymer and the environment:

$$\frac{dq_{conv}}{dt} = h\,A\,(T(t) - T_{env}) = h\,A\,\Delta T(t) \tag{3.2}$$

where q_{conv} is the heat transfer associated with convection, h is the heat transfer coefficient, A is the surface area, T is the substrate temperature, T_{env} is the temperature of the environment, and $\Delta T(t)$ is the time-dependent thermal gradient between the environment and the polymer substrate.

3.4. Fracture criteria

It is desirable to investigate defects by analyzing the flow stress, thermal shrinkage, and displacement velocity of the polymer substrate in micro hot embossing. However, fracture is more complex to study due to the viscous state of the polymer. A numerical capable to model and predict the fracture behavior in the FEA model is required (Kim et al., 2004).

Fracture in both the polymer and the buffer layers were analyzed using the Normalized Cockcroft & Latham (C&L) model presented in Equation 3.3. The C&L damage model is defined as a function of maximum principal stress normalized with effective stress (SFTC, 2014). The C&L model describes fracture as the point where the maximum damage in the object exceeds the critical value (Kim et al., 2004). The critical damage value (CDV) can be considered constant to the yield stress or the tensile strength of the material for both PMMA and PSU.

$$\int_{\varepsilon}^{\bar{\varepsilon}} \frac{\sigma^*}{\bar{\sigma}} \tag{3.3}$$

where $\sigma^*$is the maximum principal stress and $\bar{\sigma}$ is the effective stress.

Numerical analyses were performed without the addition of the damage criterion to determine the damage distribution on the polymer substrate. The critical damage value could be considered as the maximum damage value for a polymer above T_g.

3.5. Boundary conditions

Boundary conditions define how an object would interact with other objects and the environment. The most common boundary condition include heat transfer, velocity to define symmetric boundaries, force, and contact between objects in the model. Boundary conditions are defined as element edge-based conditions in the finite element mesh. An edge-based definition is used to reduce ambiguity at corners in cases where the boundary conditions could not be clearly defined. Numerical simulations require boundary conditions to be defined including velocity, contact, heat transfer, and displacement.

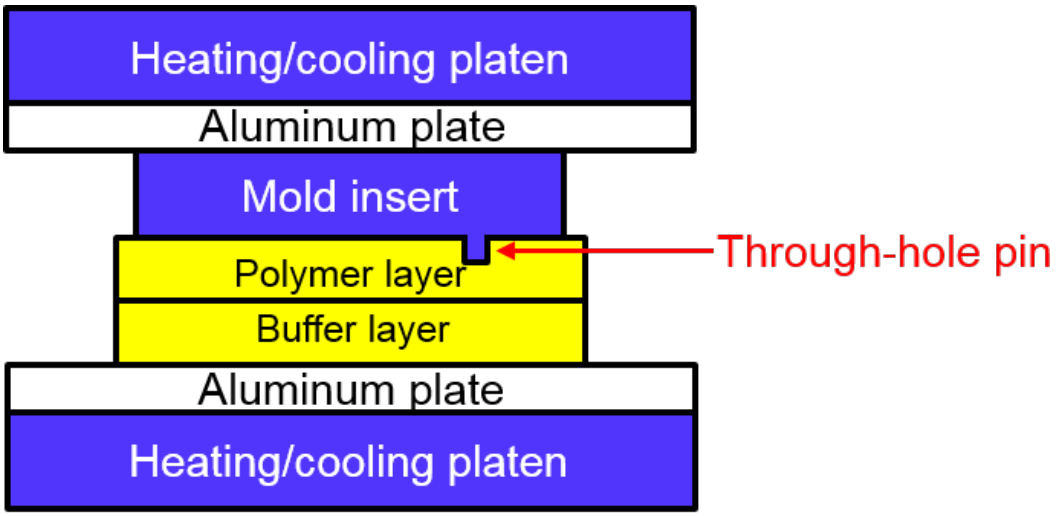

Figure 3.2. Schematic representation of the finite element simulation model for the fabrication of interconnects for polymer micro fluidic devices.

The proper selection of the boundary conditions could reduce the uncertainty of the simulation results. Boundary conditions were specified at the element edges of the finite element mesh to establish the behavior of every single object. The schematic representation of the hot embossing model used in the numerical analysis is shown in Figure 3.2. A buffer layer was placed between the aluminum plate and the polymer. The polymer was placed between the mold insert and the buffer layer for the fabrication of polymer interconnects. Both the mold insert and the aluminum plate had a width of 80 mm and a thickness of 5 mm.

Hot embossing was investigated as an axisymmetric geometric model to reduce computational resources. PMMA and PSU were be defined as a non-Newtonian fluids in the simulation. It was assumed that the molten polymer flowed identically in any cross-sectional area on the X- and Y- planes. The simulations were divided into three steps including molding, cooling, and demolding. Boundary conditions were defined for each of the different steps. An environment temperature of 100°C was defined for the numerical analysis. The environment temperature was used for the calculation of radiation and convection heat transfer in the simulation. The environment temperature represents the temperature of the surrounding area where the polymer, the buffer layer, the aluminum plate, and the mold insert were located.

3.5.1. Molding

The mold insert, polymer, buffer layer, and aluminum plate were set to the molding temperature throughout the molding step. The substrate plate moved towards the mold insert until the embossing force was reached and maintained

constant. The force-controlled simulation model applied the embossing force on the polymer for a predetermined period of time until the aluminum plate completed the total established displacement. The finite element model consisted initially of 7,570 and 6,623 brick elements for the polymer and the buffer layer, respectively. Brick elements reduce the uncertainty in the simulation results due to the smaller element edge compared to tetrahedral elements. The relative element size decreased from 200 to 25 μm as the polymer substrate reached the boundary of the mold pin.

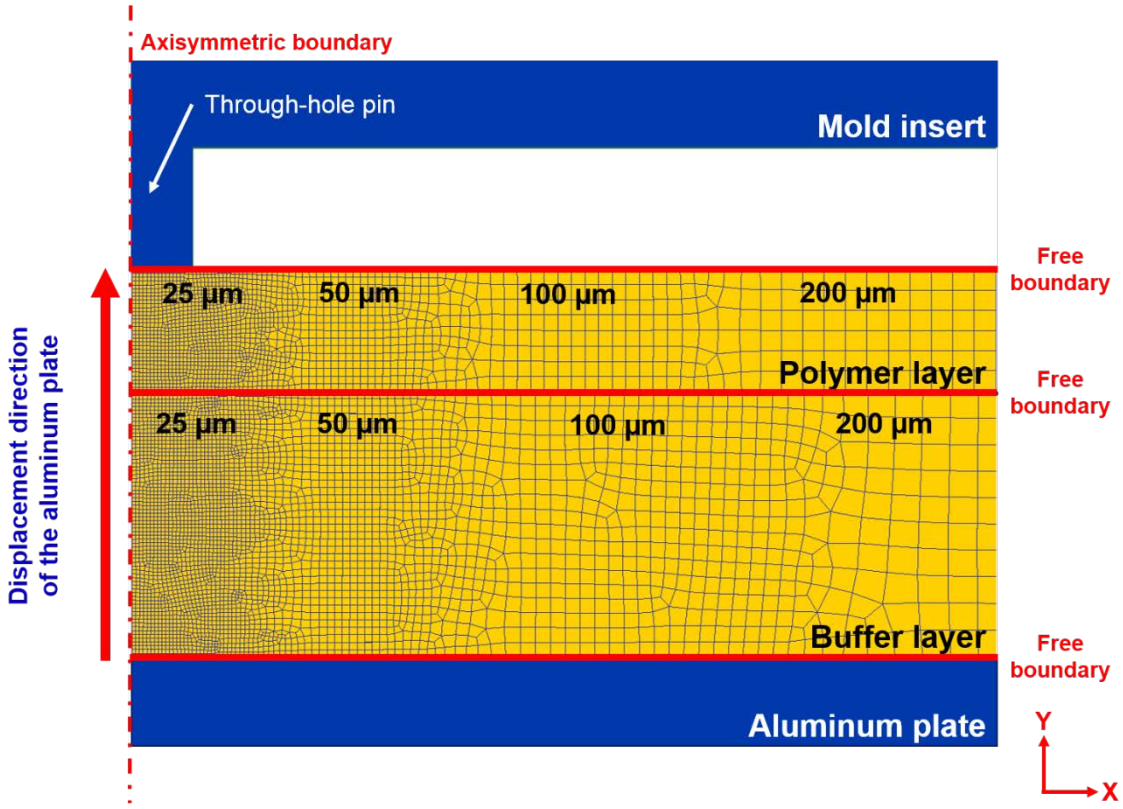

Figure 3.3. Finite element simulation model of the molding step in hot embossing. Both the substrate plate and the mold insert were considered rigid bodies.

The degrees of freedom along the edges of each object were not constrained to allow the flow of both the polymer and buffer layers as illustrated in Figure 3.3. The degrees of freedom along the axisymmetric boundary were constrained on the x-plane. The displacement of the substrate plate towards the mold insert was represented by the arrow. Surface tension, air entrapment, and adhesion forces were not taken into account in the analysis for simplification of the analysis.

3.5.2. Cooling

Cooling could be defined as the cool down of the hot embossing system to a demolding temperature (T_d). The coefficients of heat transfer for the polymer, the mold insert, the buffer layer, and the aluminum plate were assumed as constant.

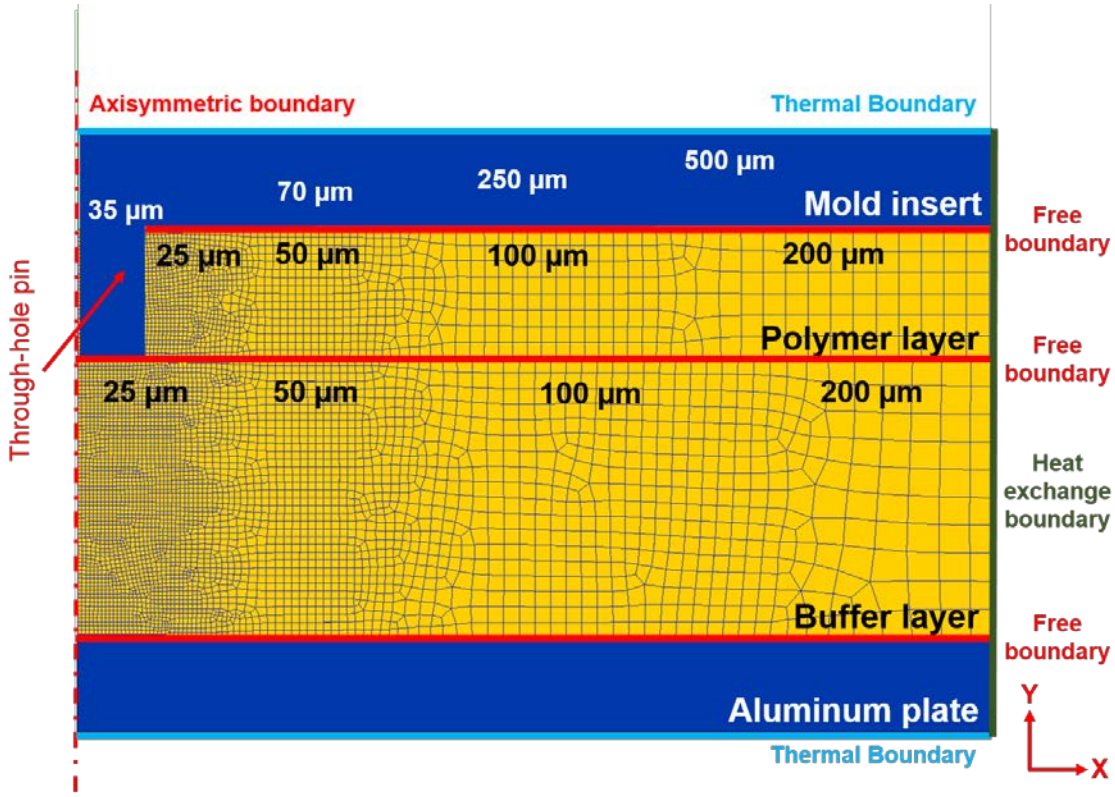

Figure 3.4. Finite element simulation model of the cooling step in hot embossing.

The cooling step was performed as a non-isothermal and axisymmetric model. All degrees of freedom on the bottom surface of the polymer substrate were not constrained to allow thermal shrinkage.

The mold insert was considered an elastic object. The elastic material behavior was defined by both the Young's modulus and Poisson's ratio to determine die stress during the numerical analysis. A finite element mesh consisting of 4450 brick elements was generated for the mold insert. The relative element size decreased from 500 to 35 μm as the brick elements reached the boundary of the pin. PMMA and PSU were considered as elasto-plastic objects.

A thermal boundary was added at the bottom edge of the aluminum plate and the top edge of the mold insert as shown in Figure 3.4. The thermal boundary was defined with a constant temperature of 80°C to allow heat transfer. No degrees of freedom were constrained, similar to the molding step, to study the displacement of the polymer and buffer layer due to thermal shrinkage. A heat exchange boundary condition were added to the edges of the mold insert, polymer, buffer, and aluminum plate. The heat exchange boundary condition determines whether heat transfer should with the environment or with an object in contact.

3.5.3. Demolding

The separation of the mold insert from the polymer layer could be achieve in the demolding step. Separation of the objects is achieved by the displacement of the mold and the substrate plate. A non-slip condition was added to the boundaries between the polymer and the buffer layer; and the buffer layer and the aluminum plate to model the force needed to separate the mold insert form the polymer

substrate. A demolding speed of 50 mm/min was used in the analysis to simulate the rapid opening of the hot embossing press as shown in Figure 3.5.

Demolding was analyzed as an isothermal model under the assumption that all the objects were at the demolding temperature. A static coefficient of friction of 0.3 was included in the analysis.

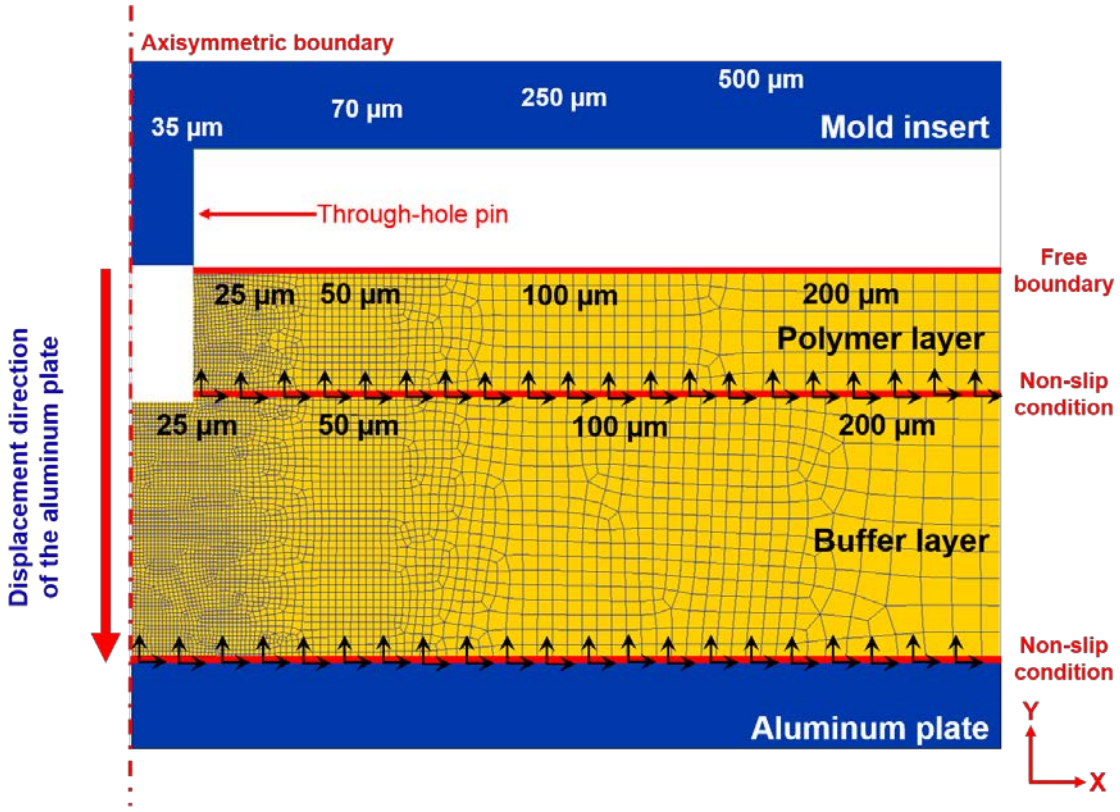

Figure 3.5. Finite element simulation model of the demolding step in hot embossing. The mold insert was defined as an elastic body to determine the effect of thermal stress.

Table 3.1. Design of experiment for the fabrication of through-holes in polymer microfluidic devices.

Run	Molding Temperature (°C)	Embossing Force (kN)	Substrate Thickness (mm)
1	100	10	0.8
2	100	30	1.5
3	100	50	3.0
4	125	10	1.5
5	125	30	3.0
6	125	50	0.8
7	150	10	3.0
8	150	30	0.8
9	150	50	1.5

3.6. Simulation Conditions

Process parameters play an important role in the replication accuracy for the fabrication of polymer microstructures. The effect of the process parameters on the molded pattern could be analyzed via parametric studies. Table 3.1 shows the combination of process parameters selected for the fabrication polymer interconnects. The combination of process parameter was selected based on the L_9 orthogonal array defined by Taguchi (Taguchi et al., 1993). Embossing forces of 10, 30, and 50 kN, molding temperatures of 100, 125, and 150°C, substrates thicknesses of 0.8, 1.5, and 3.0 mm, a constant embossing speed of 0.5 mm/min, and a holding time of 5 minutes were considered in the finite element simulations.

3.7. The results of simulation

Numerical analyses were performed to characterize micro hot embossing for the fabrication of through-holes. Simulations included the mold filling, cooling, and

demolding of hot embossing. Process parameters, such as molding temperature, embossing force, and the height of the pin, were considered in the simulation. The results of the analyses were represented by the advance of the polymer flow with the effective stress distribution. Flow stress was used to show the behavior of the polymer during embossing. The different colors in figures represented the effective stress of the polymer as a function of displacement or time.

3.7.1. Mold filling and fracture

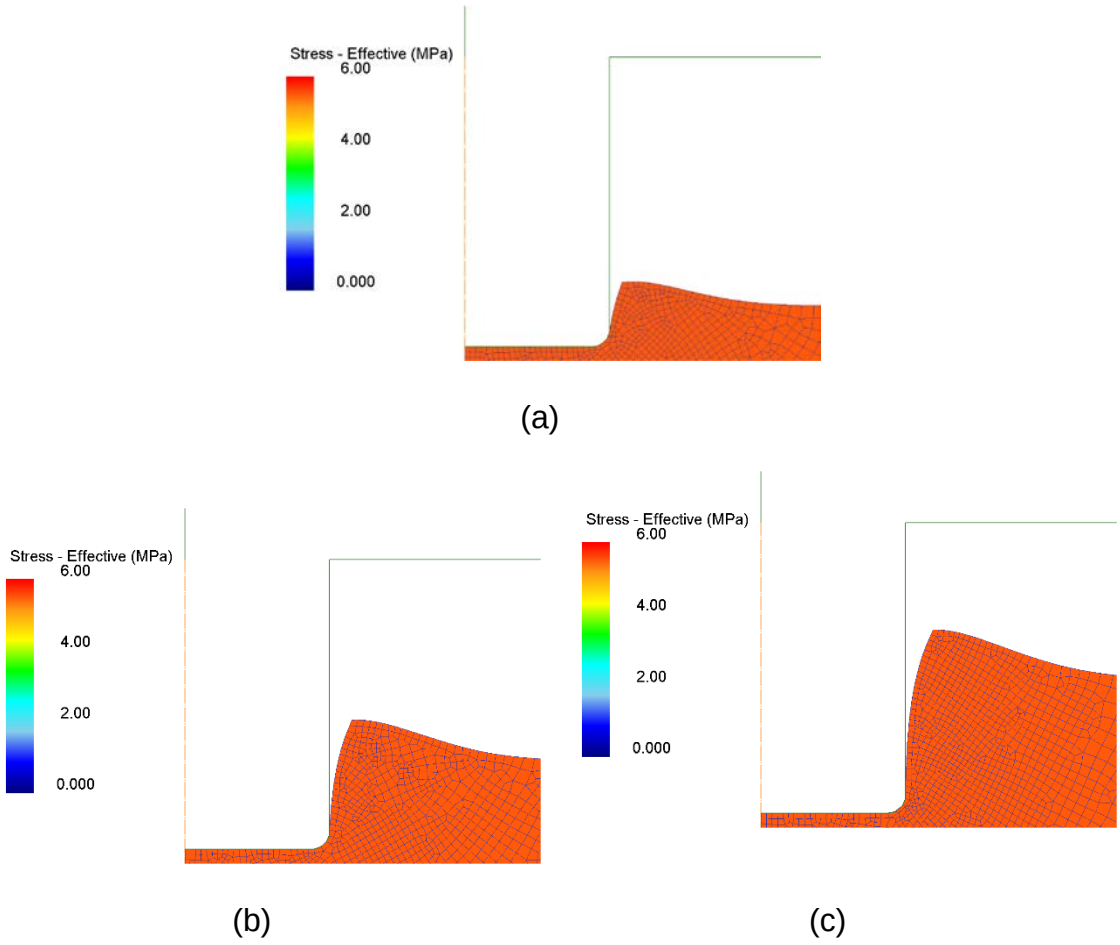

Figure 3.6. Flow stress of the pin located at the center, for the fabrication of polymer interconnects. The molding temperature was 100°C, the embossing force was 10 kN, and the polymer thickness was 0.8 mm, while the displacement was: (a) 120 µm, (b) 240 µm, and (c) 360 µm.

Figure 3.6 shows the evolution of flow stress while the displacement was 120, 240, and 360 µm. The molding temperature was 100°C, the embossing force was 10 kN, and the polymer thickness was 0.8 mm. A flow stress of 5.55 MPa was observed on the polymer during mold filling. The initial stage of mold filling is presented in Figure 3.6 (a). The polymer was squeezed and forced to flow out from the bottom of the pin. The effective stress of the polymer at a displacement of 240 µm is shown in Figure 3.6 (b).

The squeeze flow advanced along the sidewall of the pin. The advance of the flow front into the mold cavity is shown in Figure 3.6 (c). The fluidic resistance of the polymer reduced the advance of the flow front. Incomplete mold filling was observed at the end of the molding step. An in complete through-hole with a depth of 680 µm was measured in the polymer.

High stress concentration was expected at the bottom edge of the pin. However, the result of simulation below T_g was not consistent with the flow stress analyzed by Yao et al., (2007) where the flow stress at the bottom edge was significantly higher at the pattern corners due to the pressure generated by the displacement of the mold. The mold generated a contact area at the vicinity of the polymer generating a high stress concentration area between the edge of the mold cavity and the polymer.

The inconsistency between the results could be caused by displacement model defined in the simulation. The displacement direction of the polymer could cause uncertainty in the numerical model. Therefore, the cause of the numerical inconsistency is not clear and further study would be recommended.

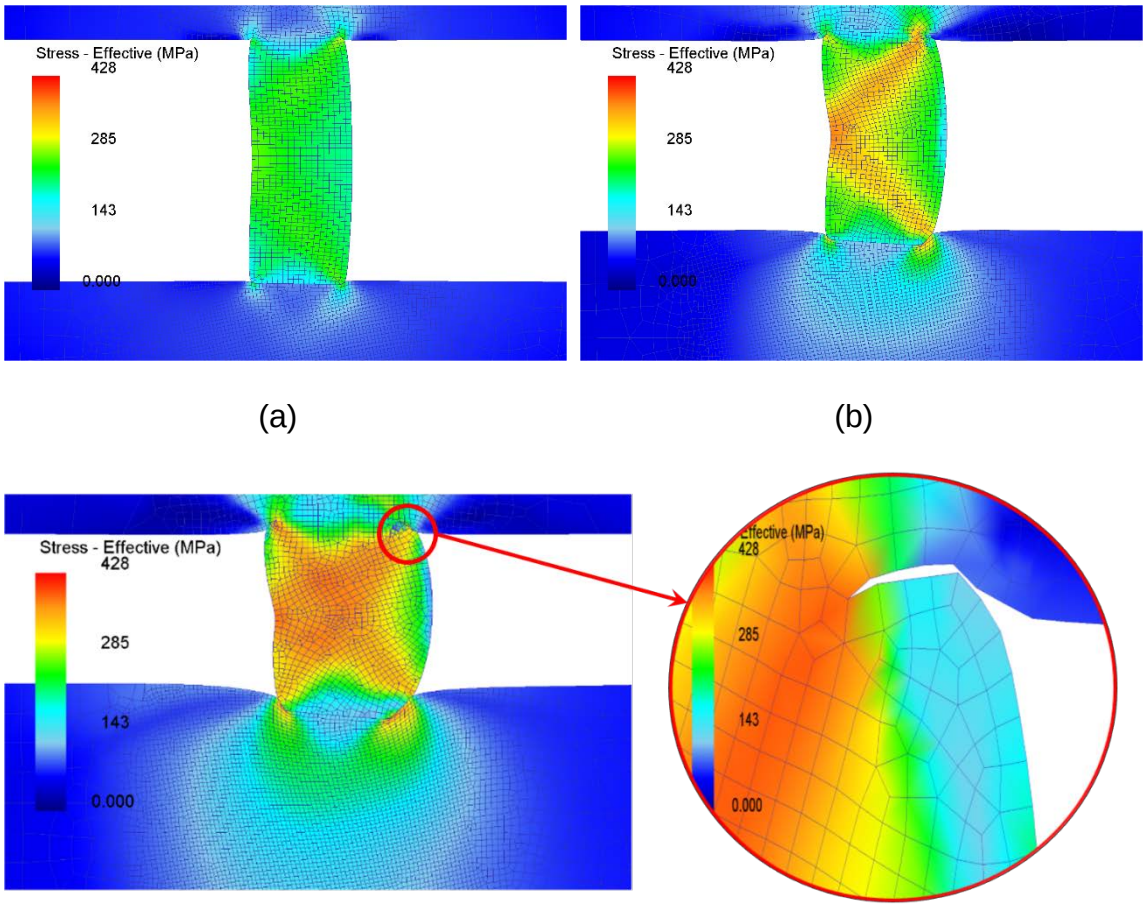

Figure 3.7. Flow stress of the pin located at 40 mm for the fabrication of polymer interconnects. The molding temperature was 100°C, the embossing force was 50 kN, and the polymer thickness was 3.0 mm, while the displacement was: (a) 0.5, (b), 0.98, and (c) 1.5 mm.

Damage of the pin at a molding temperature of 100°C, an embossing force of 50 kN, and a polymer thickness of 3.0 mm is shown in Figure 3.7. The increase in the embossing force, as well as the low molding temperature, caused the deformation of the pin. Figure 3.7 (a) represents a displacement of 0.5 mm. An effective stress of 418 MPa was estimated at the corner between the pin and the mold insert. Figure 3.7 (b) represents the high stress concentration areas at the

external top and bottom edges of the pin indicating effective stresses of 285.65 MPa and 286.17 MPa, respectively.

Fracture on the pin is shown in Figure 3.7 (c). The magnified area illustrates the fracture at the top edge of the pin at a displacement of 1.5 mm. At the corner, the stress exceeded the strength of the mold, 289.32 MPa. Figure 3.8 shows the stress evolution of the pin during mold filling. The elevated stress developed cracks on the mold (Hirai et al., 2004). Stress concentration at the internal sidewall of the pin increased due to the deformation behavior. After this point, the simulation stopped due to inconsistent step definition.

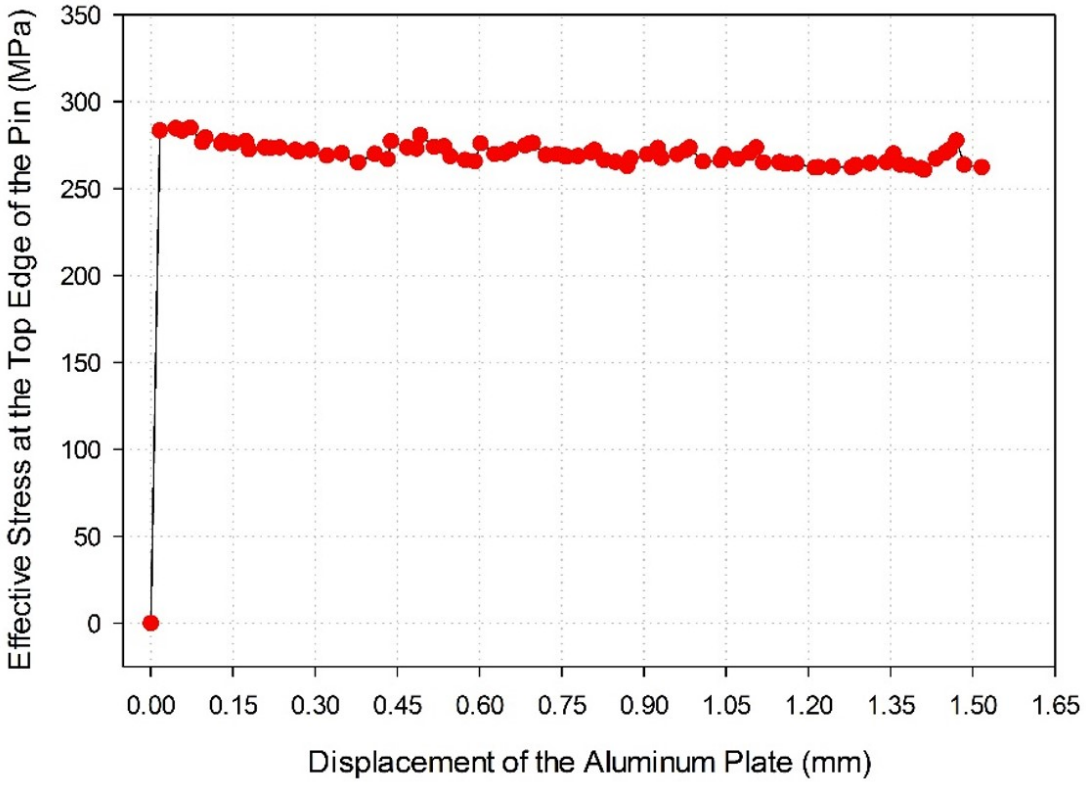

Figure 3.8. Flow stress at the pin located 40 mm from the thermal center at a molding temperature of 100°C, an embossing force of 50 kN, and a polymer thickness of 3.0 mm.

At a molding temperature of 100°C, an embossing force of 30 kN, and a polymer thickness of 1.5 mm, results of simulation did not show any significant variation in the behavior of the polymer. The increase in embossing force promoted the advance of the flow front. However, the fluidic resistance of the polymer, caused by the low molding temperature resulted in incomplete through-holes. An incomplete through-hole of 1.20 mm was estimated at the end of the molding step. Molding temperatures below the glass transition of the polymer proved to be ineffective in the fabrication of through-holes.

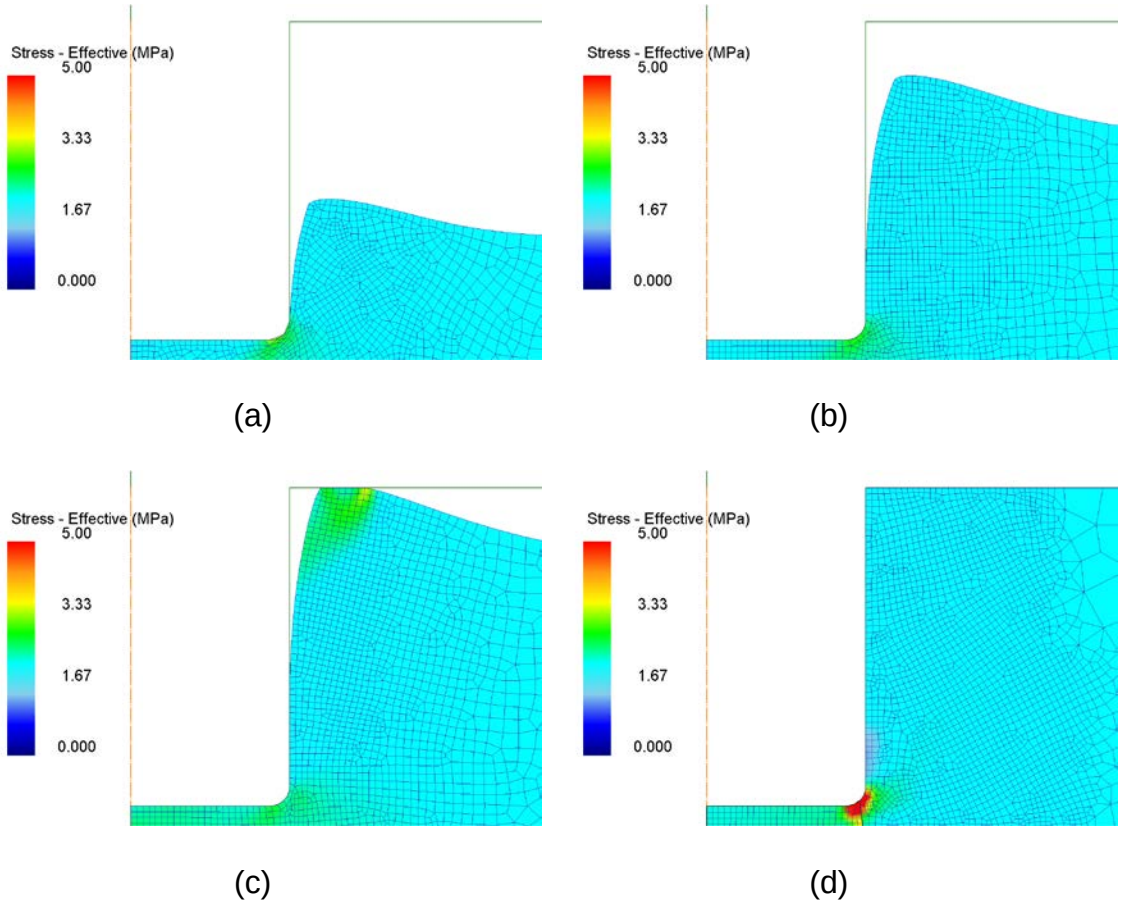

Figure 3.9. Flow stress of the polymer in the fabrication of through-holes, At a molding temperature of 150°C, and embossing force of 30 kN, and a polymer thickness of 0.8 mm. while the displacement was: (a) 260, (b) 520, (c) 650, and (d) 780 µm.

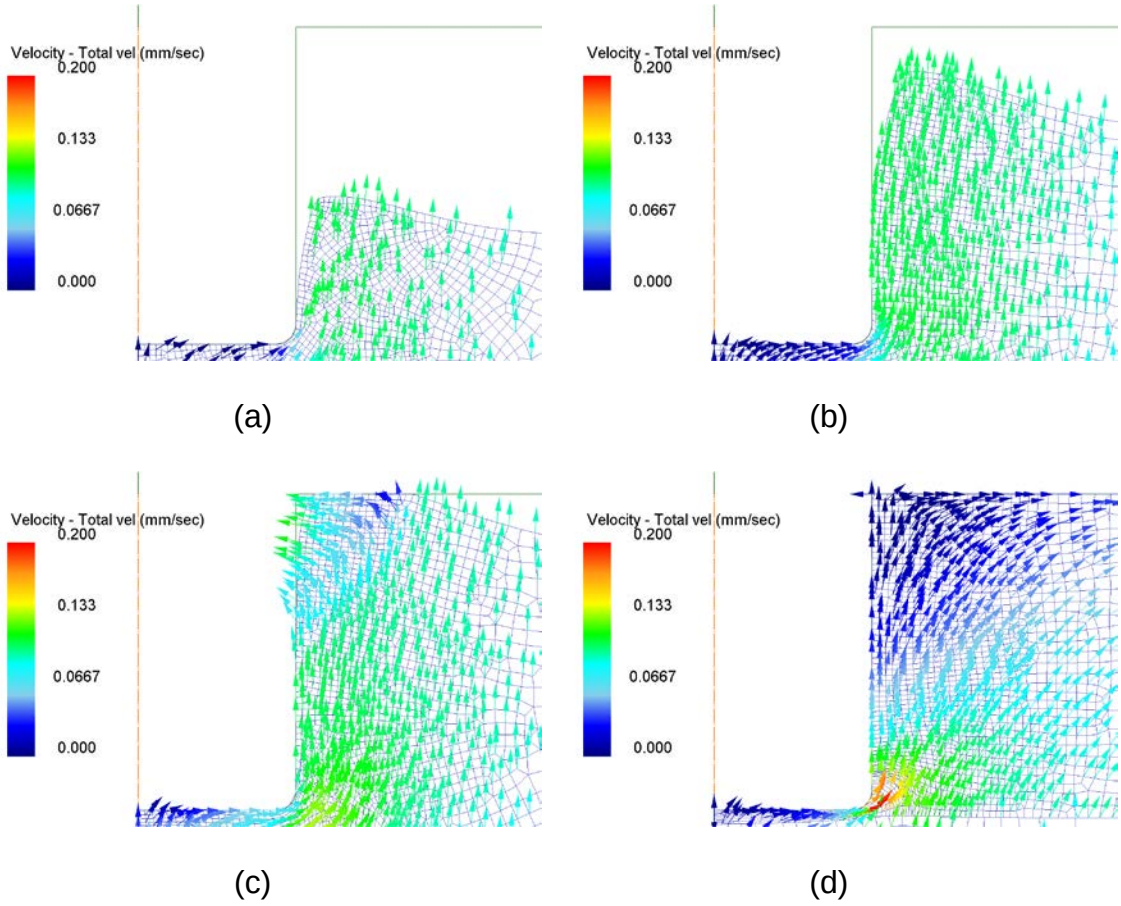

Figure 3.10. Displacement velocity of the polymer in the fabrication of through-holes, At a molding temperature of 150°C, and embossing force of 30 kN, and a polymer thickness of 0.8 mm. while the displacement was: (a) 260, (b) 520, (c) 650, and (d) 780 µm.

Figure 3.9 shows the flow stress of the polymer at the bottom edge of the pin when the molding temperature was 150°C, the embossing force was 30 kN, and the polymer thickness was 0.8 mm. The flow stress at the bottom edge of the pin and at the flow front was approximately 2.88 MPa and 1.53 MPa, respectively as shown in Figure 3.9 (a). The flow front of the polymer advanced further into the mold cavity when the displacement was 520 µm as illustrated in Figure 3.9 (b). An

increase in effective stress of 2.42 MPa was observed as the flow front of the polymer reached the boundary of the mold insert. Figure 3.9 (c) shows an effective stress of 2.71 MPa on the flow front of the polymer due to the contact with the mold insert. Complete mold filling was observed in Figure 3.9 (d). The stress around the bottom edge of the pin induced elevated stress on the polymer developing cracks (Yoshihiko et al., 2003). The crack propagated along the polymer substrate generating fracture of the residual layer. The fracture of the polymer removed the residual layer from the substrate completing the through-holes.

The flow behavior of the polymer represented by the vector of velocity is shown in Figure 3.10. Flow behavior was observed at the bottom edge of the pin and at the flow front of the polymer. A velocity of $1.17e^{-2}$ mm/sec and $1.03e^{-1}$ mm/sec was observed at the bottom edge of the pin and the flow front, respectively. The vector of velocity was significantly lower at the bottom edge of the pin than at the flow front pin due to the squeeze force applied by the pin as shown in Figure 3.10 (a). The highest velocity of $1.27e^{-1}$ mm/sec was observed at the flow front when the displacement was 520 µm as presented in Figure 3.10 (b). The advance of the flow front into the mold cavity while the displacement varied from 650 to 780 µm is shown in Figures 3.10 (c) and (d). As the displacement continued, the flow front reached the boundary of the mold cavity. The mold cavity pushed the polymer towards the sidewall of the pin at a velocity of $1.09e^{-1}$ mm/sec as illustrated in Figure 3.10 (c). The higher molding temperature softened the polymer so that the flow front could reach further into the cavity during mold filling.

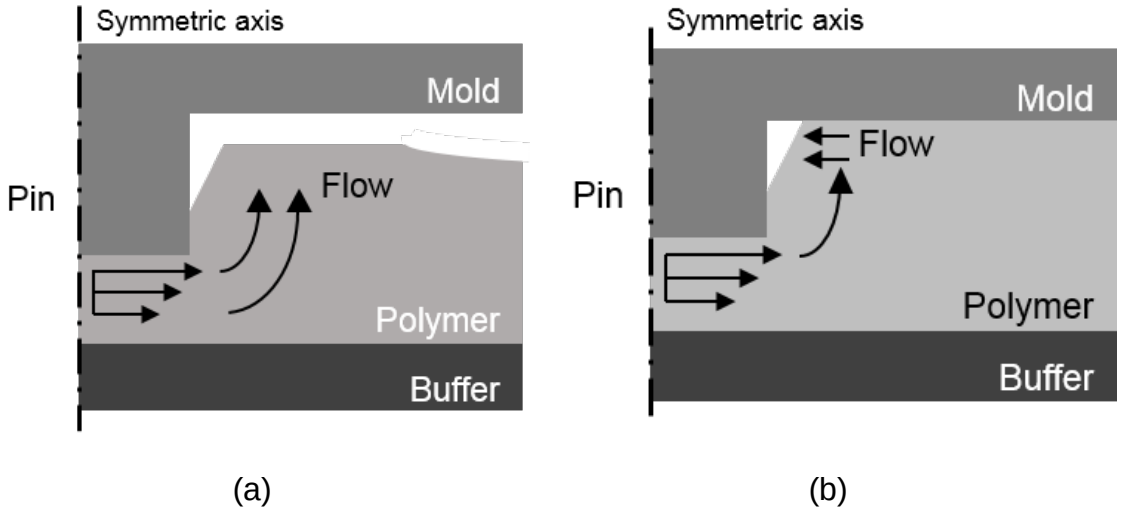

Figure 3.11. Schematic representation of the polymer deformation forces. (a) Initial stage when the flow front filled the cavity. (b) The flow front moves towards the sidewall of the pin eliminating the gap.

A schematic representation of the polymer flow behavior in the fabrication of through-holes is presented in Figure 3.11. The flow behavior of the polymer could be divided into two stages as shown in Figures 3.11 (a) and (b). At an early stage, the pin squeezed the polymer forcing it to compress, to flow out and along the sidewall of the pin. The flow front of the polymer advanced into the mold cavity due to the low resistance, until it reached the boundary of the mold insert as illustrated in Figure 3.11 (b). Mold filling was completed as the polymer flows towards the pin due to the pressure generated by the mold insert. The pressure produced by the boundary of the mold insert generated a lateral flow that reached the sidewall of the pin, reducing the gap between the polymer and the pin.

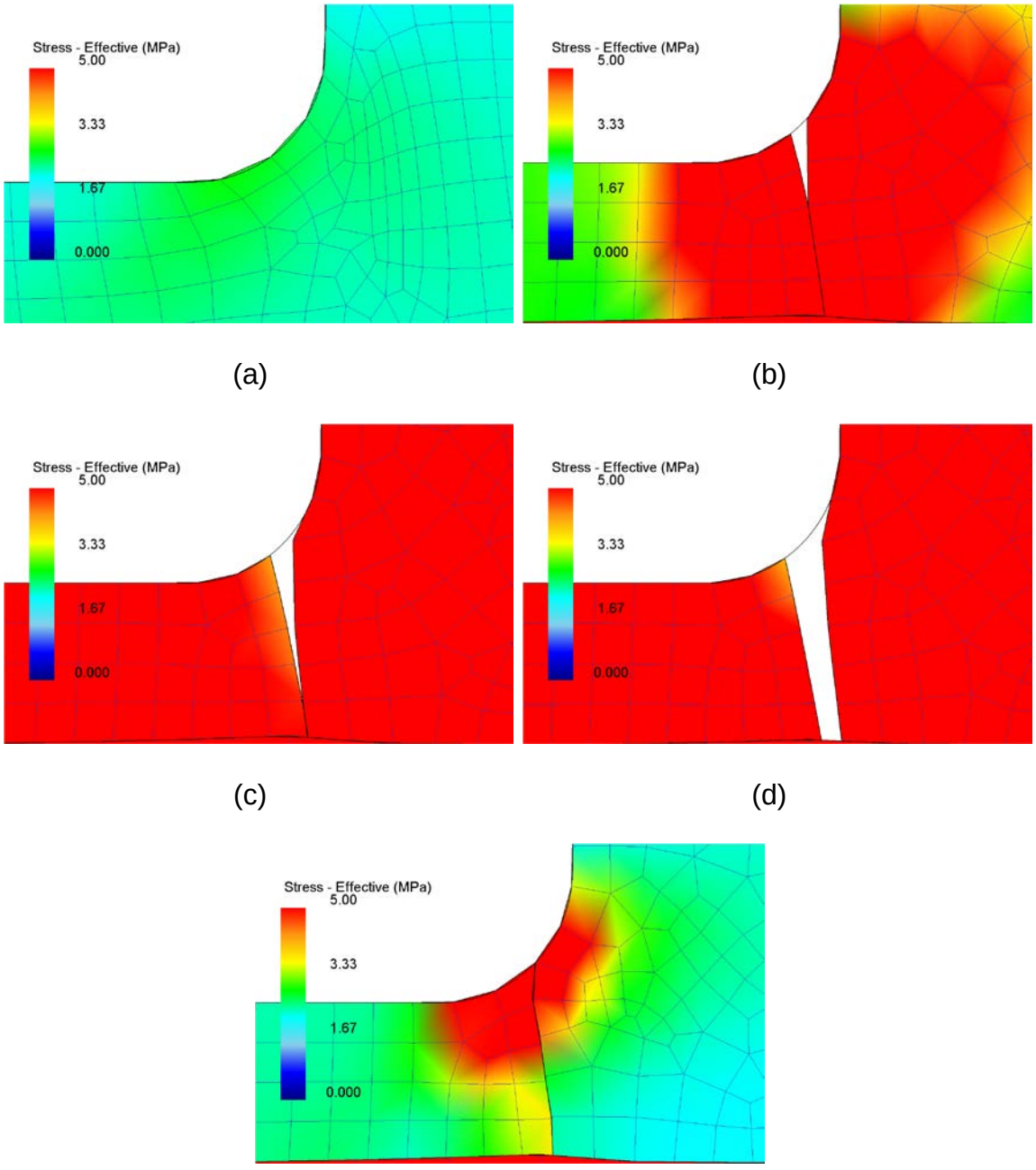

Figure 3.12. Flow stress of the polymer in the fracture process. Flow stress is represented by effective stress at displacements of: (a) 720, (b) 740, (c) 760, (d) 780, and (e) 800 µm.

The evolution of stress during fracture at a molding temperature of 150°C is shown in Figure 3.12. The flow stress was approximately 2.98 MPa at the edge of the pin when the displacement was 720 μm. Squeeze displacement form the pin caused an stress concentration area as shown in Figure 3.12 (b). The elevated stress at the corner exceeded the strength of the polymer generating a crack (Yao et al., 2007). The crack started at the interface between the bottom edge of the pin and the polymer. As the displacement continued, the crack propagated throughout the polymer until it reached the bottom surface generating fracture.

Fracture of the residual layer was caused by the stress concentration at the edge of the pin as represented in Figure 3.12 (c) and (d). Compression from both the pin and the buffer layer promoted the stress concentration area at the bottom edge of the pin. After fracture, a gap was generated between the polymer substrate and the residual layer as shown in Figure 3.12 (d).

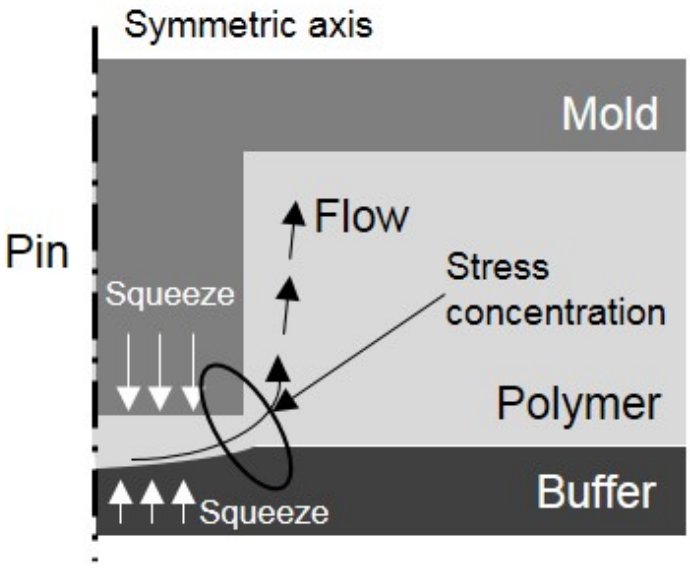

Figure 3.13. Schematic representation of the polymer squeezed flow indicating the high stress concentration zone due to the deformation of the buffer layer.

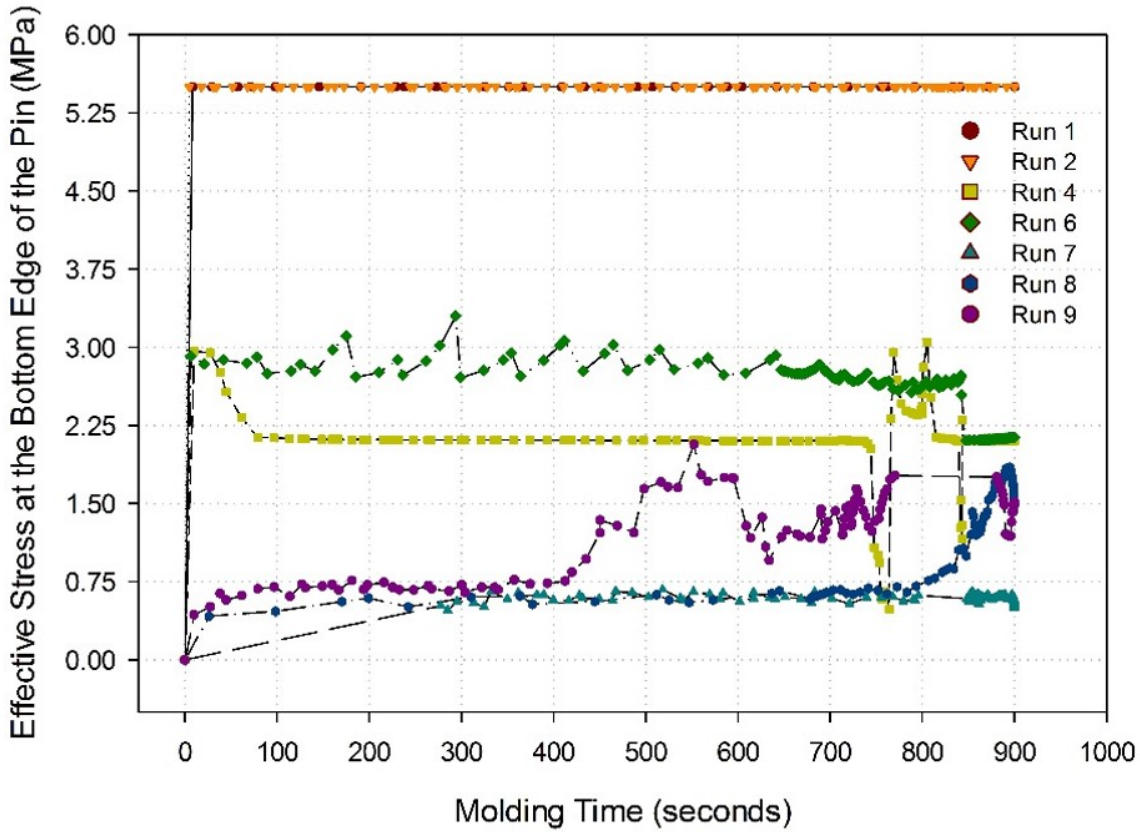

Figure 3.14. Flow stress of the polymer located at the center, at molding temperatures of 100, 125, and 150°C; embossing forces of 10, 30, and 50 kN; and polymer thicknesses of 0.8, 1.5, and 3.0 mm.

As the embossing force continued, the residual layer advanced until it reached the boundary of the polymer as shown in Figure 3.12 (e). A schematical representation of the fracture process is illustrated in Figure 3.13.

Figure 3.14 shows the effective stress of the polymer interconnect located at the center when the temperatures were 100, 125, and 150°C. The increase of molding temperature achieved complete fabrication of through-holes as higher temperatures decreased the fluidic resistance of the polymer.

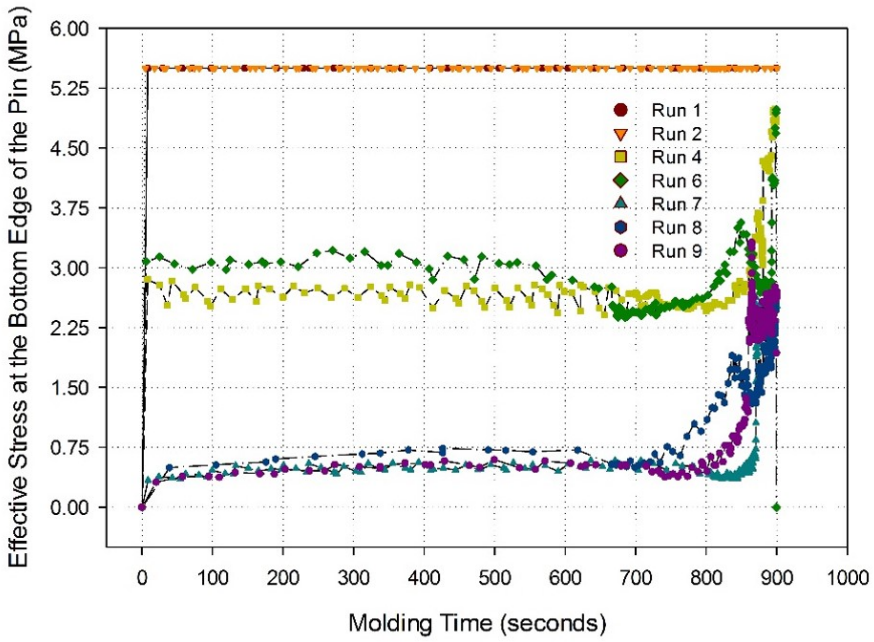

(a)

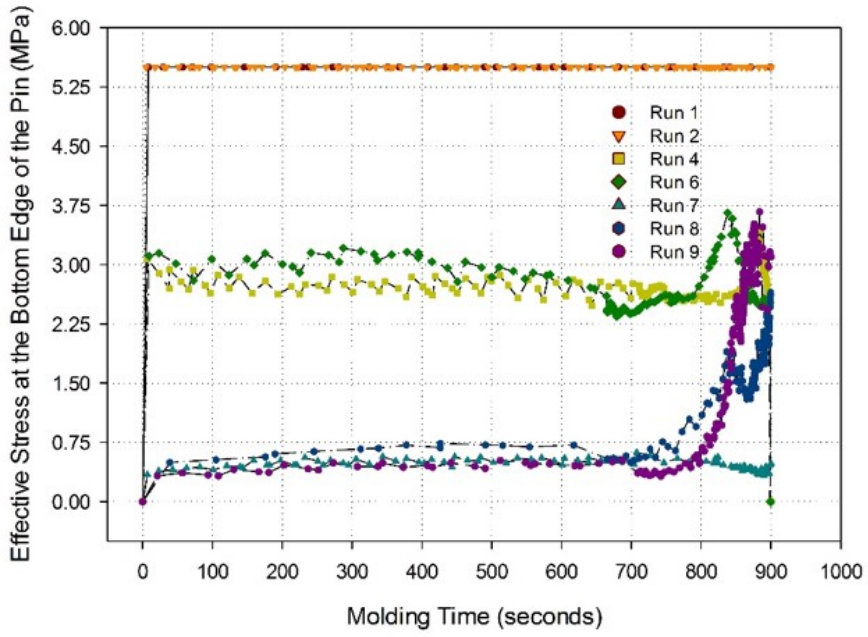

(b)

Figure 3.15. Flow stress of the polymer at molding temperatures of 100, 125, and 150°C; embossing forces of 10, 30, and 50 kN; and polymer thicknesses of 0.8, 1.5, and 3.0 mm. When the radial locations were: (a) 20 mm and (b) 40 mm.

The reduction in the fluidic resistance of the polymer could be observed by the decrease in effective stress as the molding temperature was increased. The pin could penetrate rapidly into the polymer during mold filling. This can be explained by the softening of the polymer as the molding temperature was increased which lead to a better replication fidelity.

Flow stress during mold filling at radial locations of 20 and 40 mm relative to the thermal center are shown in Figure 3.15. The evolution of stress for the pin located at 20 mm is presented in Figure 3.15 (a). There was not significant variation on the stress evolution when compared with the stress of the pin located at the center. Figure 3.15 (b) represents a similar trend on the effect of the molding temperature in the evolution of effective stress. Flow stress on the polymer was directly related with the molding temperature, the embossing force, and the height of the pin.

Complete through-holes were observed at molding temperatures above T_g. The results of the simulations showed the successful fabrication of through-holes on polymers with a thickness of 0.8, 1.5, and 3.0 mm, at molding temperatures of 125 and 150°C, and embossing forces of 10, 30, and 50 kN. The increase in molding temperature significantly affected the squeeze flow of the polymer, allowing it to advance further into the mold cavity to fabricate through-holes.

3.7.2. Cooling

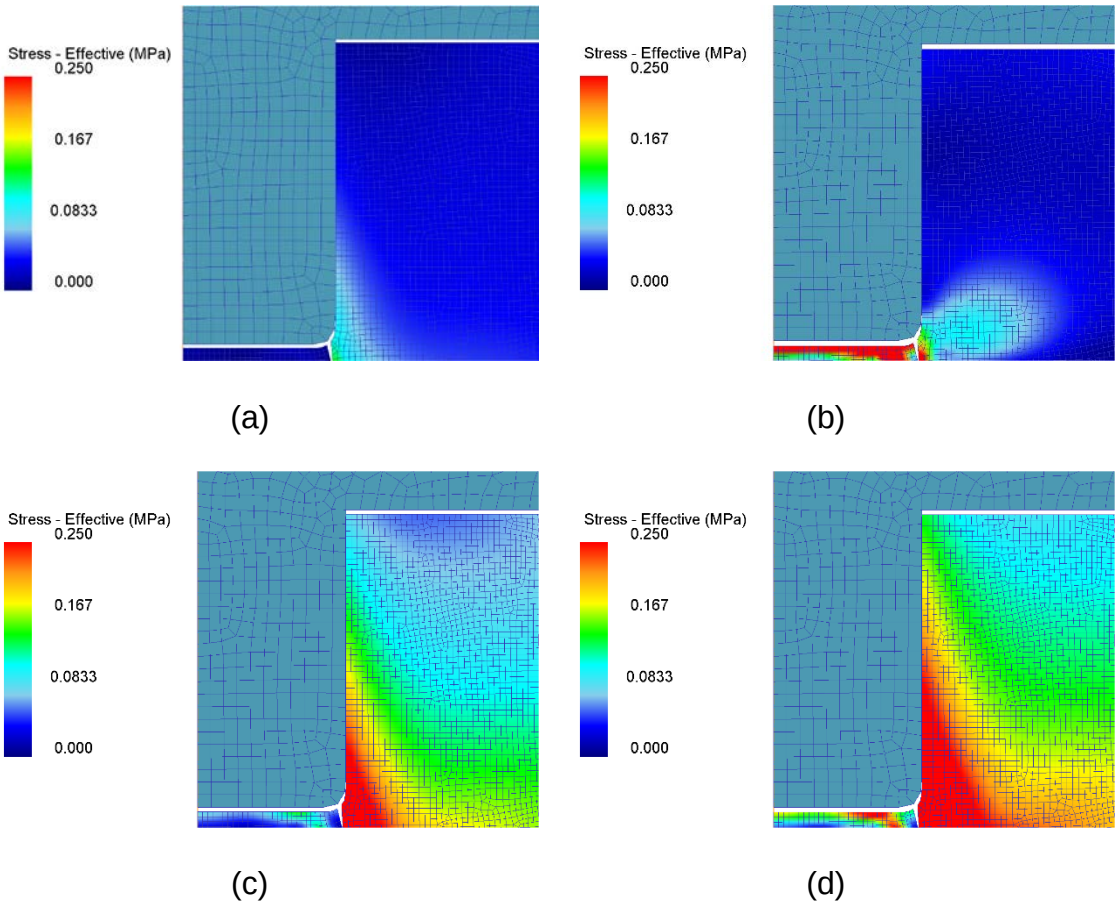

Figure 3.16. Flow stress of the through-hole at the center of the mold insert during the cooling step at cooling times of: (a) 25, (b) 316, (c) 616, and (d) 900 seconds.

The results of simulations showed the effective stress distribution around the interface of the pin and the polymer. Flow stress was used to represent thermal stress and shrinkage when the polymer was cooled from 125°C to a temperature

below T_g. Figure 3.16 shows the effective stress distribution of a through-hole located in the center. Cooling times of 25, 316, 616, and 900 seconds are presented.

Stress was localized near the bottom of the pin on the sidewall, due to thermal shrinkage. Figure 3.16 (a) shows the stress on the polymer after 25 seconds into the cooling step. An effective stress of 0.072 MPa and 0.17 was observed at the sidewall of the through hole and at the interface between the residual layer and the polymer, respectively.

The increase in stress concentration at the residual layer is shown in Figure 3.16 (b). The shrinkage of the polymer substrate compressed the residual layer generating an effective stress of 0.25 MPa at the interface between the polymer and the residual layer. After 316 seconds, the stress developed along the sidewall of the pin due to the contact between the polymer and the pin as shown in Figure 3.16 (c).

The effective stress at the contact area was generated by the difference in the coefficient of thermal expansion. This difference, caused the polymer to shrink at a higher rate compared to the mold insert. Figure 3.16 (d) shows an effective stress of 0.25 MPa across the sidewall of the pin after 900 seconds of cooling.

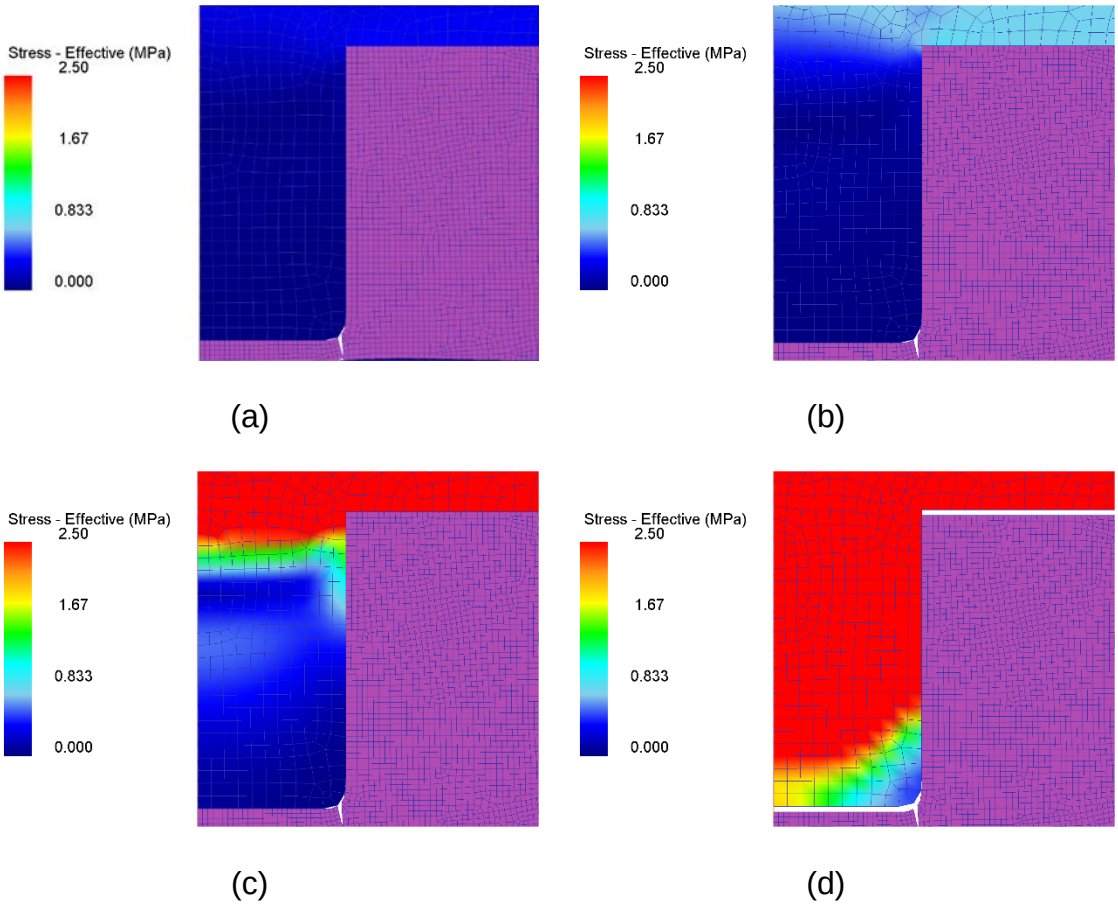

Figure 3.17. Flow stress of the pin located at the center of the mold insert during the cooling step at cooling times of: (a) 25, (b) 316, (c) 616, and (d) 900 seconds.

Figure 3.17 illustrates the effective stress on the pin located at the center as it was cooled from 125°C to the demolding temperature. Since the heat transfer initiated from the top of the mold insert, the base of the mold insert cooled before the pin. Therefore, the effective stress was localized at the base of the pin as shown in Figure 3.17 (a). The stress at the base of the mold continued to increase as the cooling time progressed as presented in Figure 3.17 (b). At 616 seconds, an effective stress of 2.50 MPa was observed at the base of the pin due to the shrinking polymer. Figure 3.17 (c) shows the increase in stress at the base of the pin caused by the pressure applied by the polymer near the bottom.

The shrinkage of the polymer caused the separation between the bottom of the pin, the residual layer, and the bottom base of the polymer. The separation generated reduced effective stress at the bottom edge of the pin as shown in Figure 3.17 (d). The effective stress on the cooling step of a through-hole located at 40 mm relative to the thermal center is shown in Figure 3.18. The stress developed from the top of the through-hole and propagated towards the bottom.

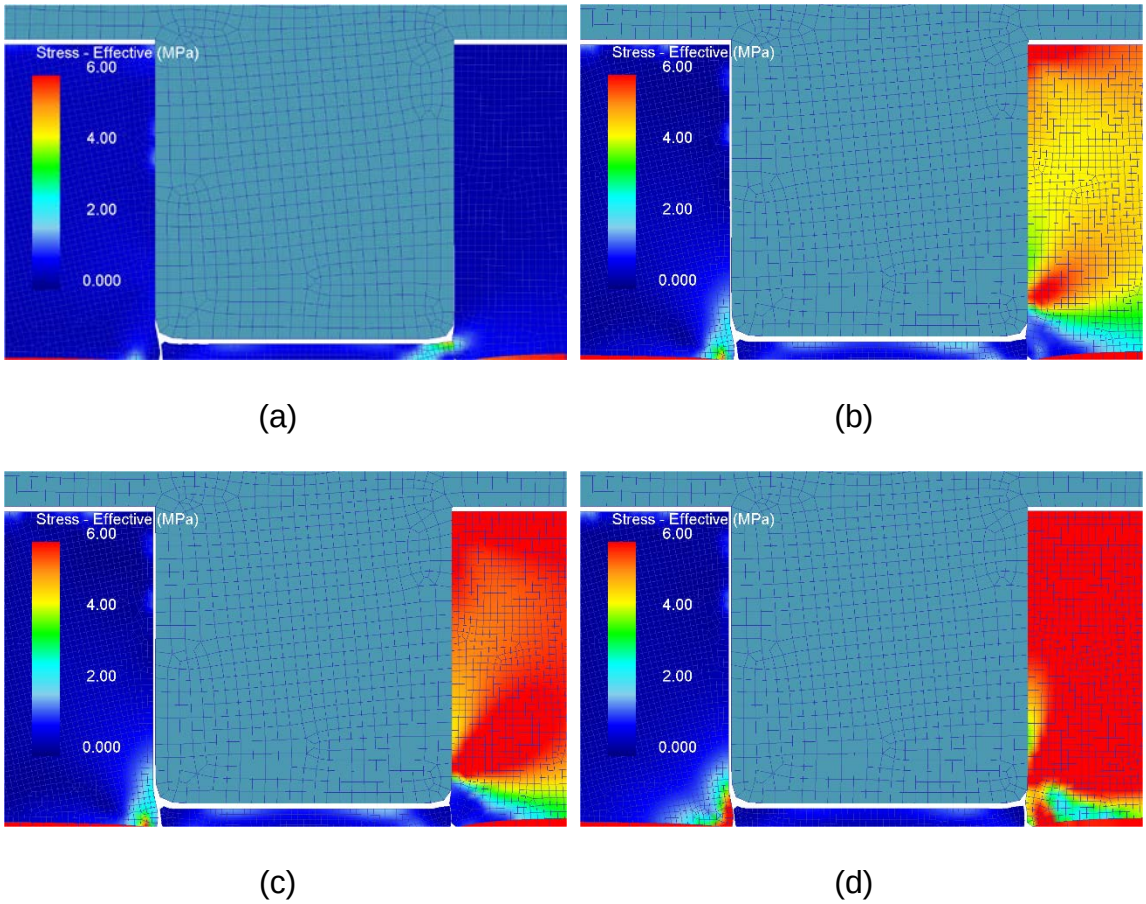

Figure 3.18. Flow stress of the polymer interconnect located at 40 mm from the thermal center during the cooling step at cooling times of: (a) 25, (b) 299, (c) 599, and (d) 900 seconds.

Figures 3.18 (b) and (c) illustrate the propagation of stress across the sidewall of the through-hole. The residual layer obstructed the shrinkage of the polymer causing reduced stress at the bottom of the through-hole.

Non-uniform stress distribution was observed due to the shrinkage of the residual layer. The stress distribution after 900 seconds into the cooling step is shown in Figure 3.18 (d). The shrinkage of the polymer and the residual layer generated the contact with the pin. An effective stress of 6.00 MPa was observed throughout the through-hole. The stress developed on the left bottom of the through-hole. The increase in effective stress could be caused by the bending of the pin during the cooling step.

Additionally, the pin located at 40 mm relative to the thermal center reduced the stress at the pins located closer to the thermal center. The location of an auxiliary structure between the edge of the polymer and the center could act as a stress barrier, which could significantly affect the stress distribution on the through-hole by sharing the converging thermal stress between patterns. Hence, adding a stress barrier could reduce defects of on the through-hole.

Figure 3.19 illustrates the stress of the pin located at 40 mm from the thermal center when the cooling times were 25, 299, 599, and 900 seconds. Stress was located at the top edges of the pin as shown in Figures 3.19 (a) and (b). Elevated stress at the top edges was caused by higher rate of shrinkage of the polymer. The shrinkage pushed the polymer into the pin generating stress at the edges and causing bending of the pin. Figures 3.19 (c) and (d) present the development of stress across the surface of the pin while the polymer continued to shrink.

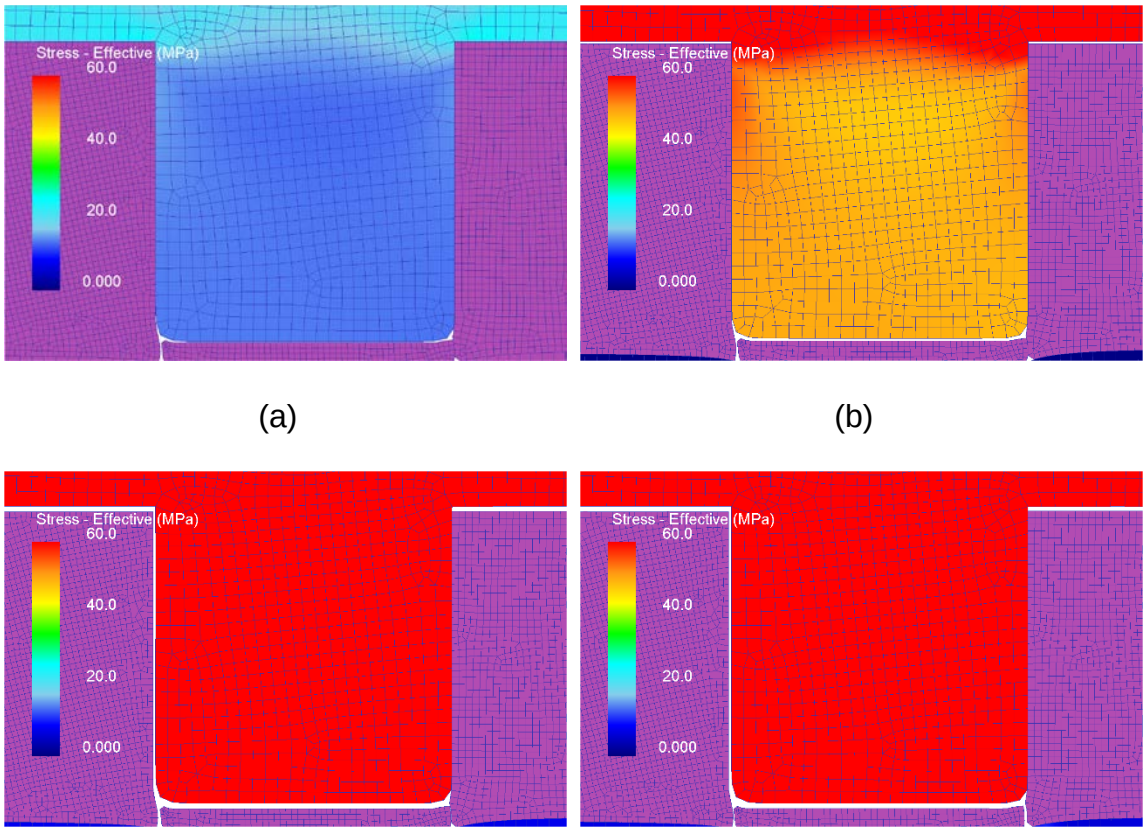

Figure 3.19. Flow stress of the pin located at 40 mm from the thermal center during the cooling step at cooling times of: (a) 25, (b) 299, (c) 599, and (d) 900 seconds.

The distribution of effective stress across the base of the pin located at 40 mm relative to the thermal center is shown in Figure 3.20. The first and last points on the figure represent the top left and right edges of the pin, respectively. An effective stress of 125 and 146 MPa was observed at this points due to the possible bending of the pin. The shrinking polymer pushed the right top edge of the pin generating higher stress concentration when compared to the left edge. Effective stress decreased while moving towards the center of the pin due to the increase in distance with the interfacing surfaces.

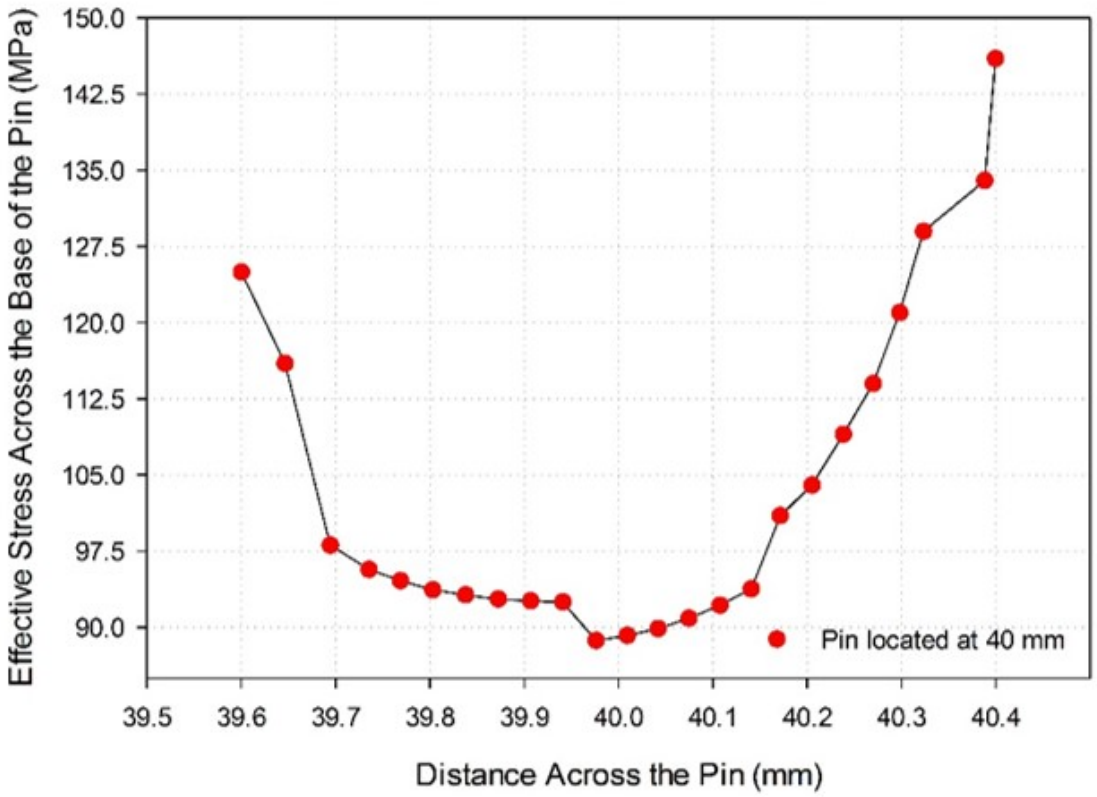

Figure 3.20. Effective stress distribution across the base of the pin located at 40 mm relative to the thermal center at 900 seconds of cooling.

The displacement of the polymer during cooling as function of the vector of velocity is shown in Figure 3.21. The polymer and the pin shrunk towards the thermal center as shown in Figure 3.21 (a). A displacement velocity of $1.78e^{-5}$ mm/sec was observed at the right sidewall of the polymer, while the displacement velocity at the right boundary of the pin was $1.08e^{-5}$ mm/sec. Elevated stress was caused by the difference in velocities, confirming that the polymer shrinks at a higher rate compared to the pin. Figure 3.21 (b) shows the highest velocity of the displacement of the cooling step.

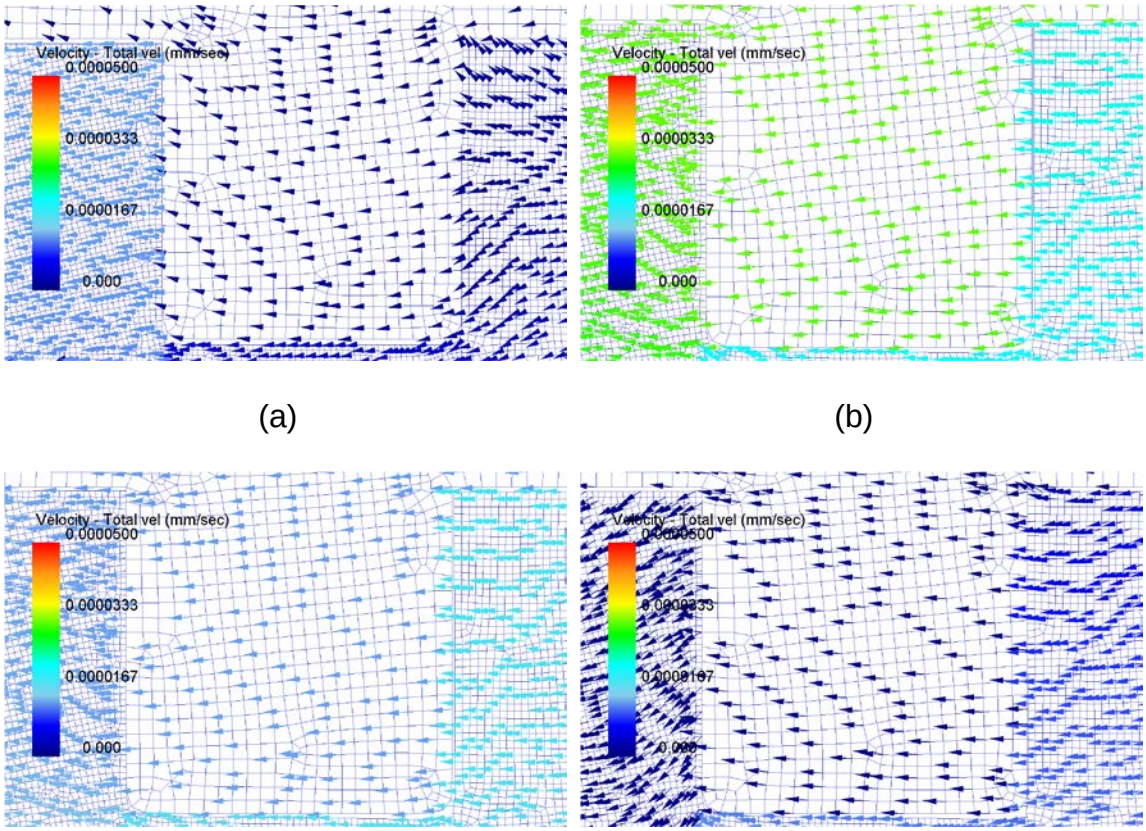

Figure 3.21. Thermal shrinkage of the polymer interconnect located at 40 mm relative to the thermal center, at cooling times of(a) 25, (b) 299, (c) 599, and (d) 900 seconds.

Displacement velocities of $2.42e^{-5}$ mm/sec and $1.96e^{-5}$ mm/sec were observed at the right boundaries of the polymer and the pin, respectively. The vector of velocity of both the polymer and the pin decreased due to the hardening of the material as the temperature continued to decrease. Figures 3.21 (c) and (d) illustrate the decrease in the vector of velocity as the cooling step progressed. After 900 seconds, the displacement velocity of the polymer was $7.62e^{-6}$ mm/sec while the pin had a displacement velocity of 0 mm/sec. The thermal shrinkage increased the rigidity of the pin reducing its displacement when the demolding temperature was reached.

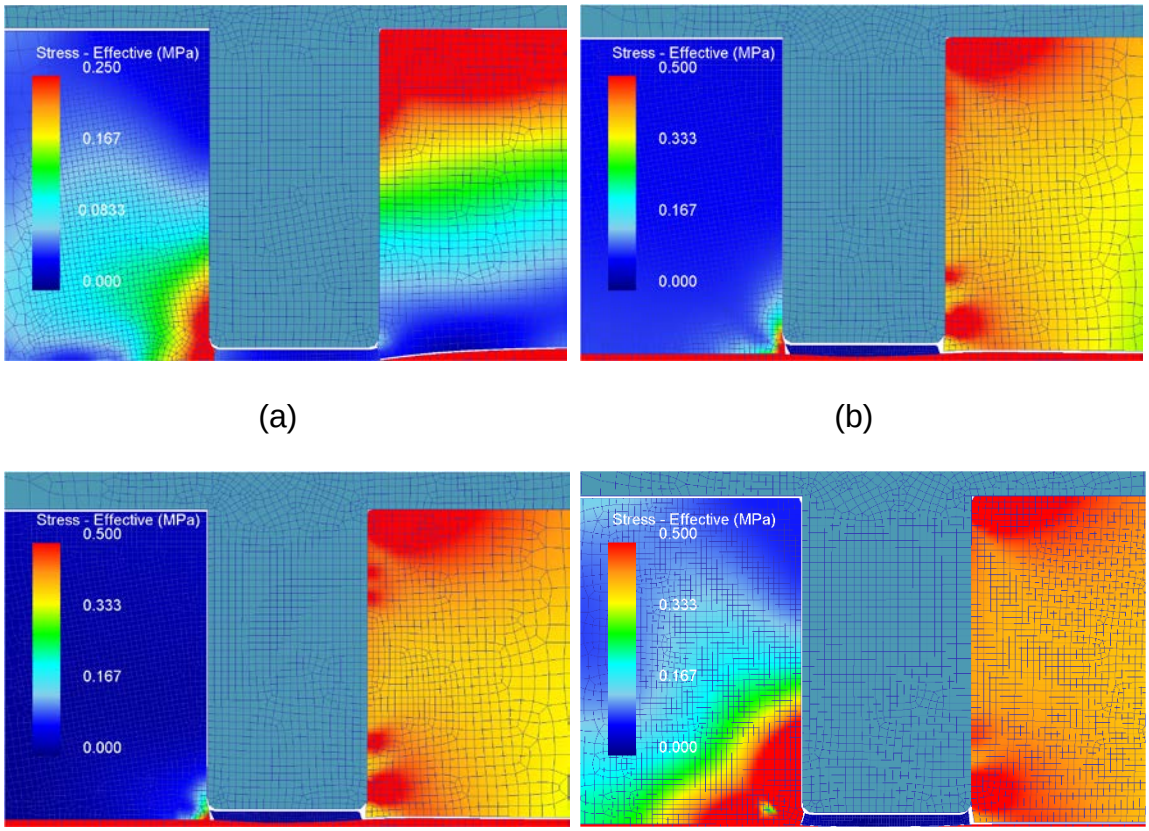

Figure 3.22. Flow stress of the through-hole at a radial location of 40 mm relative to the thermal center during the cooling step, at cooling times of: (a) 25, (b) 299, (c) 599, and (d) 900 seconds.

Figure 3.22 shows the stress distribution of a 1.5 mm through-hole as the polymer cooled to the demolding temperature. Effective stress was observed in both the left and right sidewalls of the through-hole. Figure 3.22 (a) shows the initial shrinkage of the polymer causing the pin to bend towards the center. The bending of the pin could be observed due to the stress concentration at the left bottom and top right edge of the polymer. Figures 3.22 (b) and (c) illustrate a decrease in effective stress at the left sidewall of the polymer due to the higher rates of

shrinkage. The pin continued to bend as the polymer shrunk causing higher stress on the right sidewall as shown in Figure 3.22 (d). The increase in the length of the pin caused it to be more susceptible to bending due to the increase in the pin moment at the top edge.

The stress evolution at the bottom edge of the pin can be seen in Figure 3.23. The stress evolution at the bottom edge of the pin was directly related with the radial locations from the thermal center during cooling.

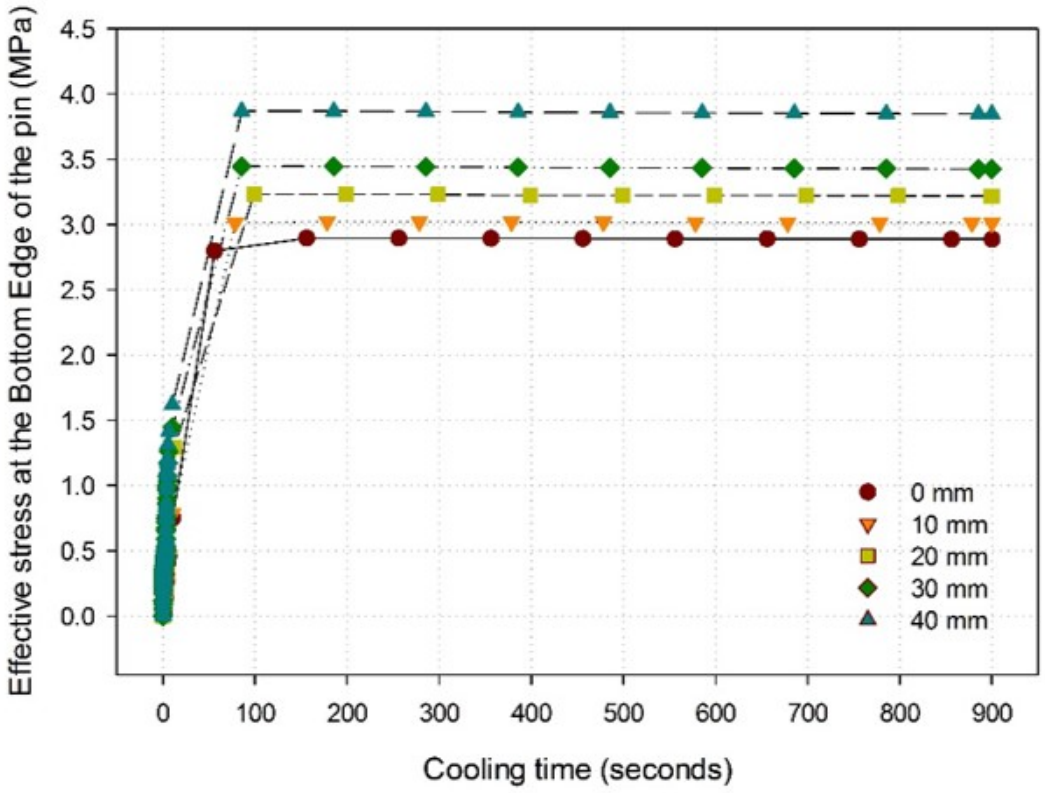

Figure 3.23. Effective stress distribution at the bottom edge of the pin during cooling, at pin locations of 0, 10, 20, 30, and 40 mm from the thermal center. When the molding temperature was 150°C, the embossing force was 30 kN, and the polymer thickness was 0.8 mm.

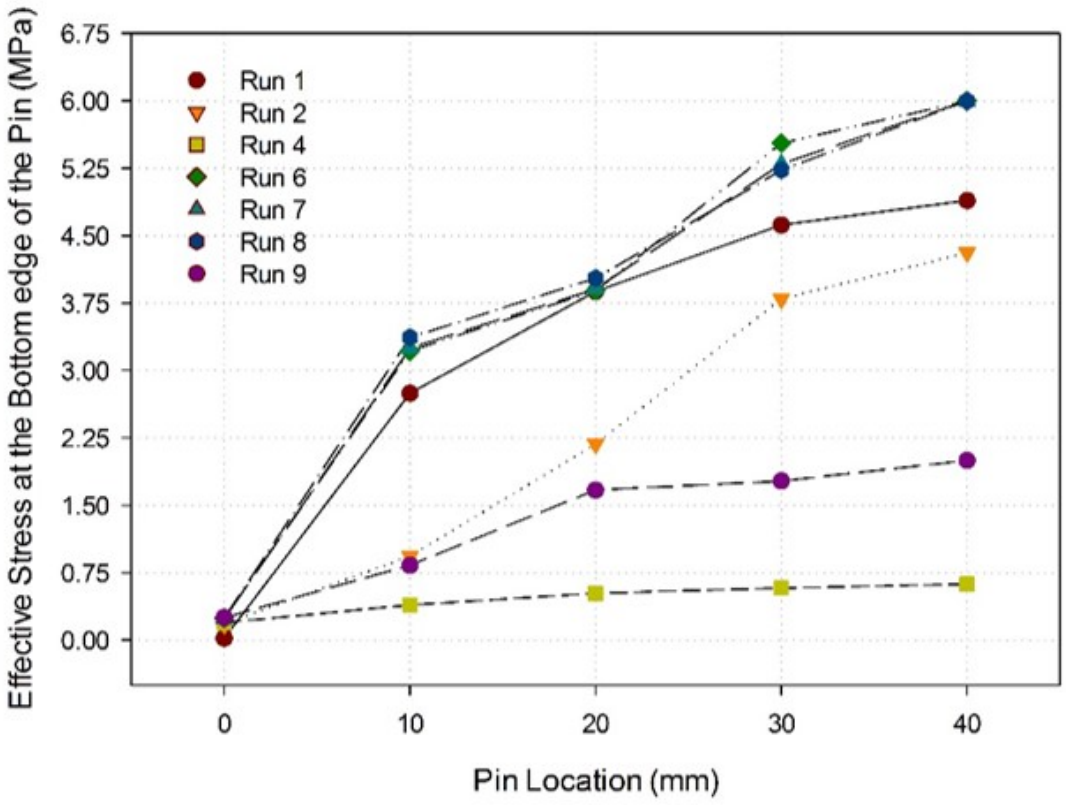

Figure 3.24. Flow stress at the bottom edge of the pin after 900 seconds of cooling, at radial locations of 0, 10, 20, 30, and 40 mm from the thermal center. When the molding temperatures were 100, 125, and 150°C, the embossing forces were 10, 30, and 50 kN, and the polymer thicknesses were 0.8, 1.5, and 3.0 mm.

The effective stress on the polymer increased with the increase in the radial location of the pin. During the first 100 seconds into the cooling step, the accelerated heat loss caused elevated effective stress. This could be explained by the thermal shrinkage generated by the decrease in temperature. Thermal shrinkage induced a rapid increase in stress by pushing the polymer into the right sidewall of the pin due to the difference displacement velocities.

Figure 3.24 shows the flow stress at the bottom edge of the pin after 900 seconds into the cooling step. As the distance of the pin increase in relation to the

thermal center, effective stress increased due to the higher shrinkage rates observed at the edges of the polymer.

The results of simulations showed the effect of the pin location on the effective stress distribution on the polymer during cooling. The higher the molding temperature the higher the effective stress observed at the pins due to the difference between the molding and demolding temperatures.

3.7.3. Demolding

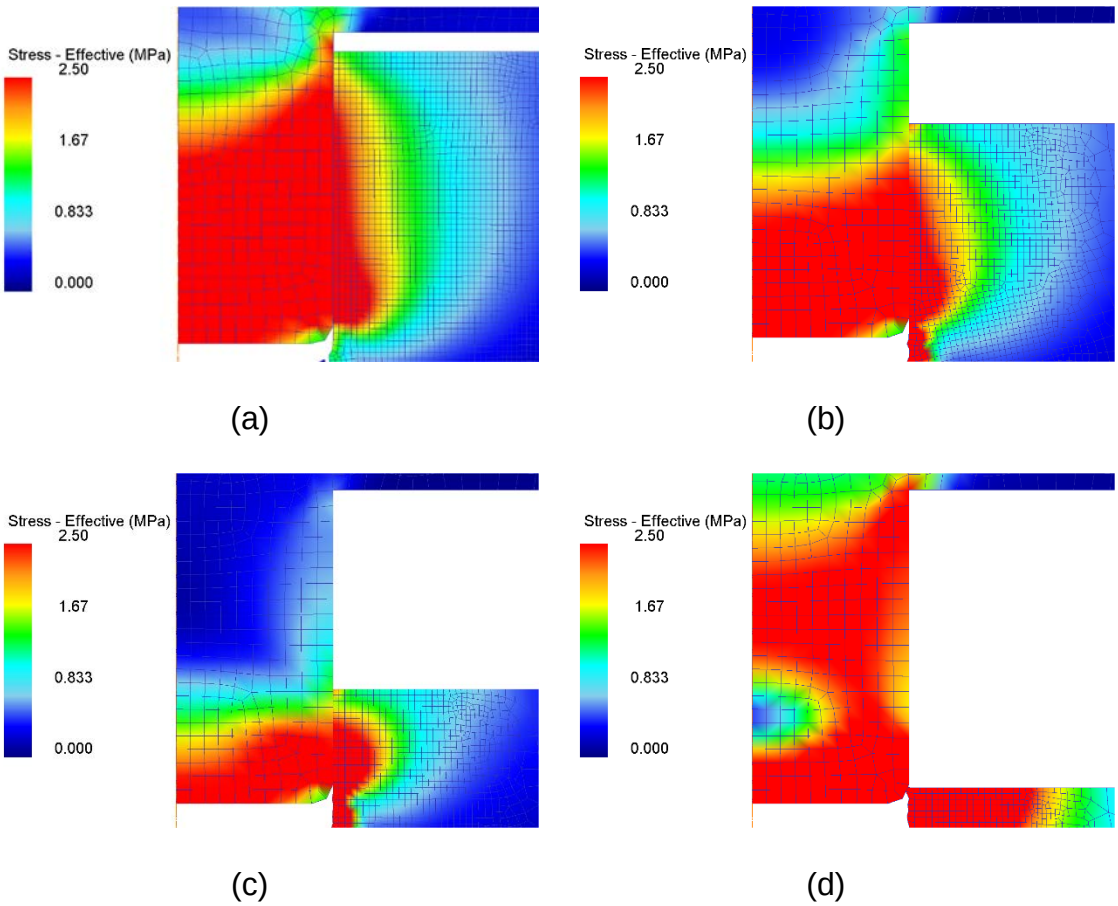

Figure 3.25. Effective stress distribution in the through-hole located in the center at a molding temperature of 125°C, when the displacement was (a) 25, (b) 250, (c) 500, and (d) 750 µm.

Stress distribution in the demolding process when the polymer was cooled from 125°C to the demolding temperature of 80°C is shown in Figure 3.25. The stress distribution after 25 µm of displacement is illustrated in Figure 3.25 (a). Stress was localized along the interface between the pin and the polymer sidewalls. An effective stress of 9.31 and 2.96 MPa was observed on the pin and the polymer, respectively.

The stress generated on the pin during demolding was significantly higher than it was on the polymer. Higher stress on the pin was caused by the displacement due to the shrinkage of the polymer. Figure 3.25 (b) illustrates the decrease in stress on pin due to the separation between the pin and the polymer after 250 µm of displacement.

The separation caused the increase of stress on the lower section of the pin and the polymer. Stresses of 11.57 and 3.10 MPa were observed at the bottom of the pin and the polymer, respectively. Figure 3.25 (c) shows the stress concentration localized at the bottom of the pin when the displacement was 500 µm. Figure 3.25 (d) illustrates the last point of contact between the pin and the polymer. At 750 µm of displacement, the contact between the edges of the polymer and pin caused the propagation of stress throughout the pin. Stress propagation was generated by reduced contact which generated higher pressure.

Figure 3.26 shows the stress of a through-hole located at a radial location of 40 mm while the displacements were 25, 250, 500, and 750 µm. There was no bending observed on the pin due to the reduced stress on the bottom left sidewall of the pin and the polymer.

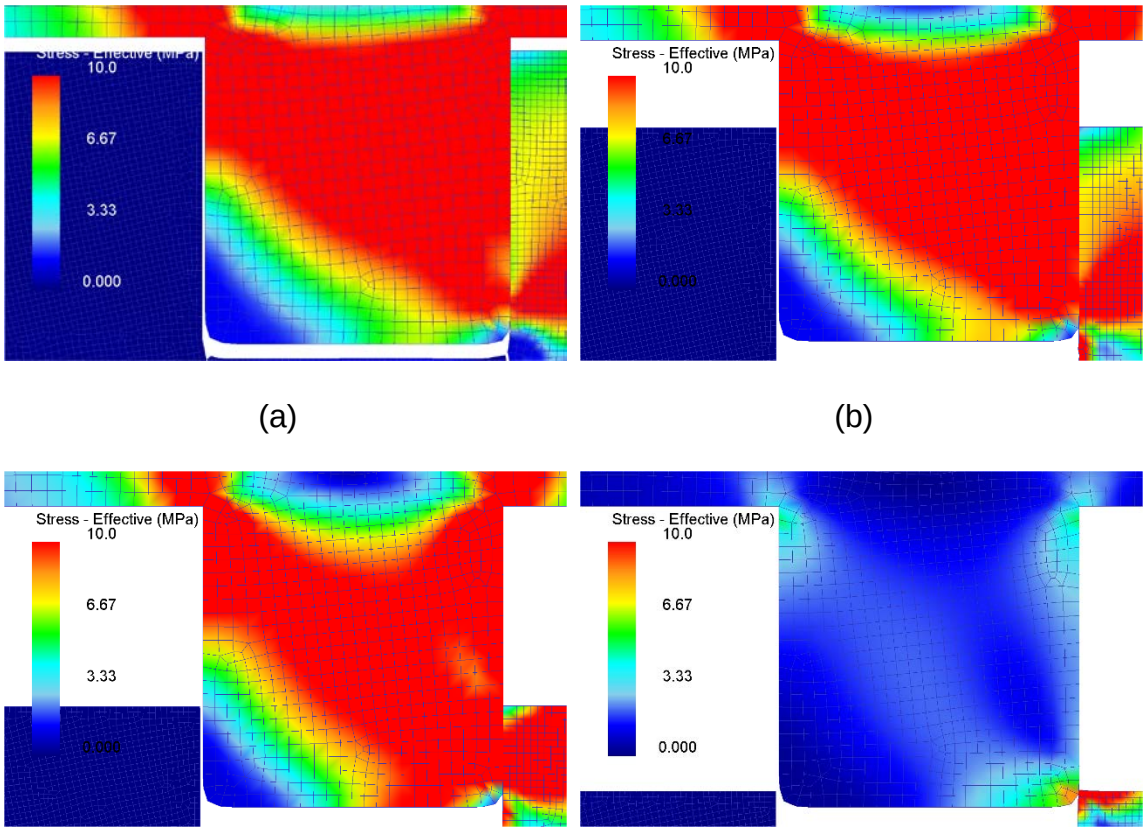

Figure 3.26. Effective stress distribution in the through-hole located at 40 mm from the thermal center at a molding temperature of 125°C, when the displacement was (a) 25, (b) 250, (c) 500, and (d) 750 µm.

Figures 3.26 (a), (b), and (c) illustrate the stress located across the right sidewall due to the contact between the polymer and the pin. Increased effective stress was observed when compared to the pin located in the center. The elevated stress was generated by the higher shrinkage rate of the polymer as the radial location increased. Reduced stress was observed at a displacement of 750 µm as shown in Figure 3.26 (d). The stress was concentrated at the contact between the bottom edge of the pin and the right top edge of the polymer.

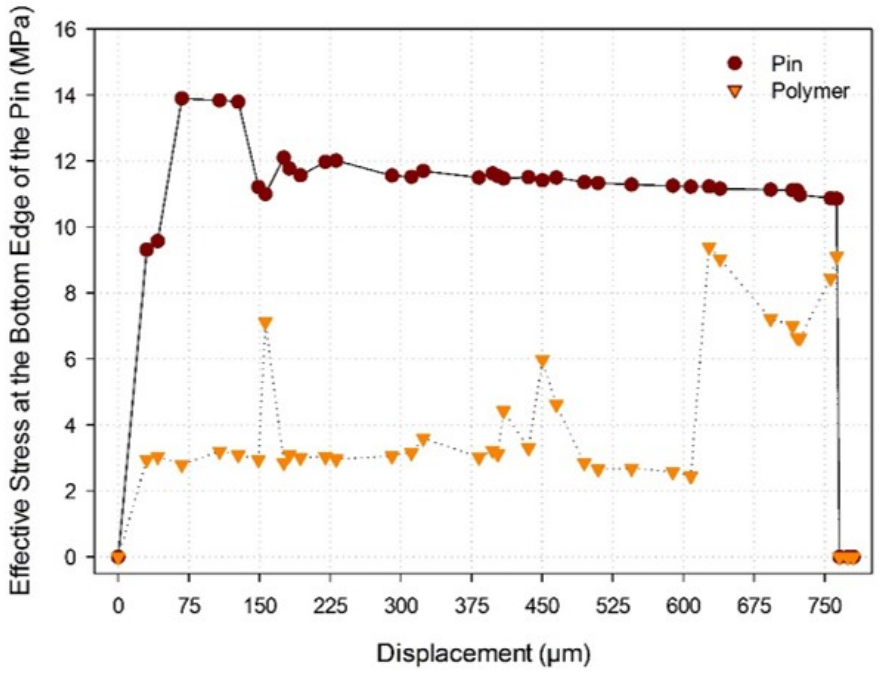

(a)

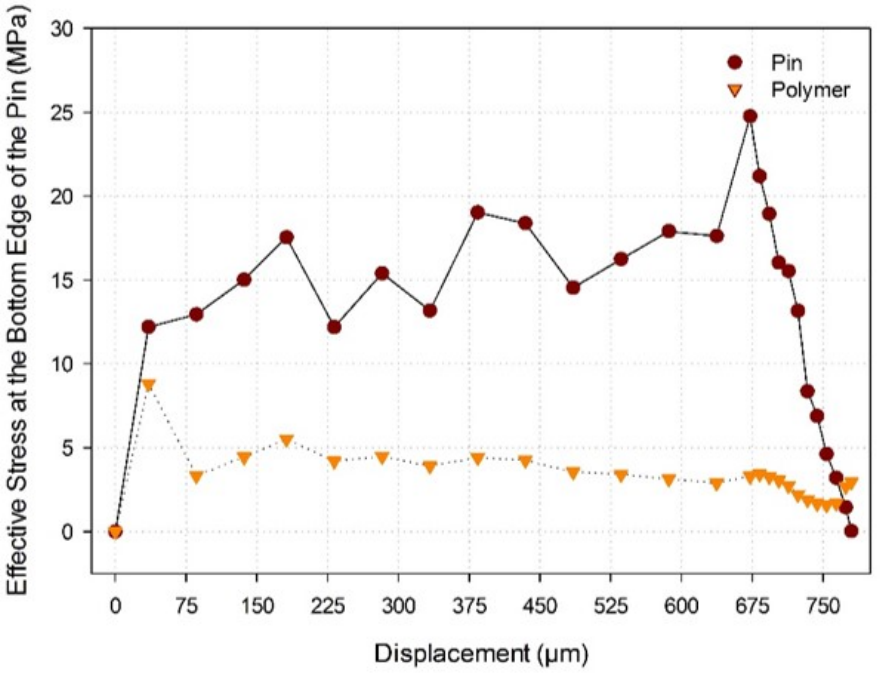

(b)

Figure 3.27. Evolution of stress at the bottom edge of the pin during demolding, at radial locations of (a) 0 and (b) 40 mm relative to the thermal center.

The evolution of effective on the pin and the polymer during demolding is presented in Figure 3.27. Effective stress increased after 25 µm of displacement as shown in Figure 3.27 (a). The increase in stress was caused by the friction generated at the interface between the pin and the polymer (Omar et al., 2014). The stress generated at the polymer was lower than the stress at the pin due to the difference in the thermal expansion which cooled down faster the pin.

The stress distribution on the pin reached a peak of 12.01 MPa at a displacement of 75 µm. After the peak was reached the stress decreased to approximately 11.14 MPa until the demolding step was completed. When the pin was separated from the polymer the effective stress was reduced to 0 MPa.

Figure 3.27 (b) illustrates the effective stress of a pin located at 40 mm from the thermal center. The stress on the pin during demolding was significantly higher as the radial location increased. The stress peak on the pin was observed at 675 µm of displacement. An effective stress concentration of 24.75 MPa was caused by the friction between the polymer and the pin.

The stress of a pin with a length of 1.5 mm located at the center is illustrated in Figure 3.28. The increased length of the pin caused higher stress concentration during demolding when the displacement ranged from 25 to 250 µm. The elevated concentration of stress was generated by the reduced aspect ratio of the pin when compared to the 0.8 mm pin. Figures 3.28 (a), (b), (c), and (d) show the effective stress localized at the contact area at the bottom edge of the pin as the demolding process continued. At a displacement of 750 µm, stress was observed at the bottom edge of the pin and the polymer. No signs of pin damage were observed.

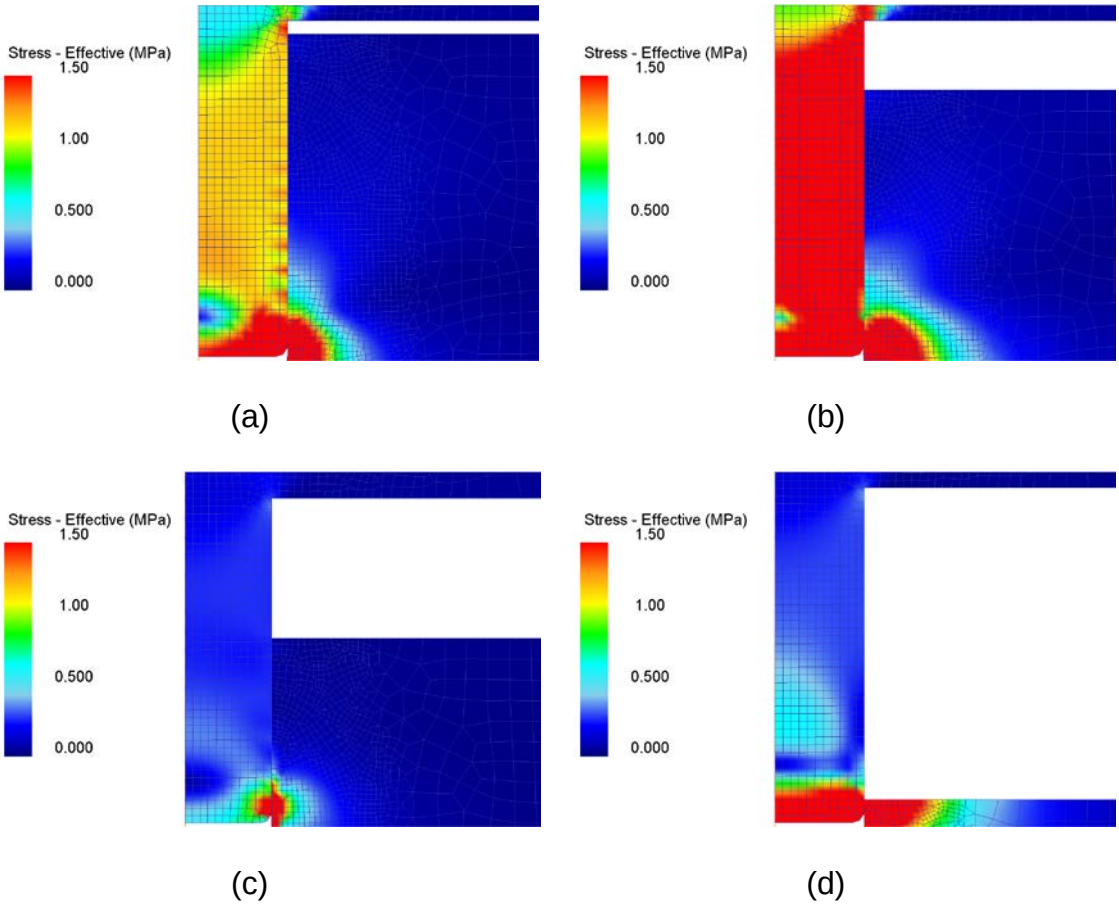

Figure 3.28. Effective stress distribution in the through-hole located in the center at a molding temperature of 150°C, when the displacement was (a) 25, (b) 250, (c) 500, and (d) 750 µm.

The distribution of effective stress in a through-hole located at 40 mm from the thermal center is illustrated in Figure 3.29.Effective stress concentration was observed at the left and right top edges of the pin as shown in Figures 3.29 (a), (b), (c), and (d). The stress propagated from the left and right top edges as the demolding process continued. The stress propagation at the mentioned locations was caused by the pressure applied from the moving polymer. Bending of the pin could be caused by the elevated stress generated by the contact between the pin and the polymer.

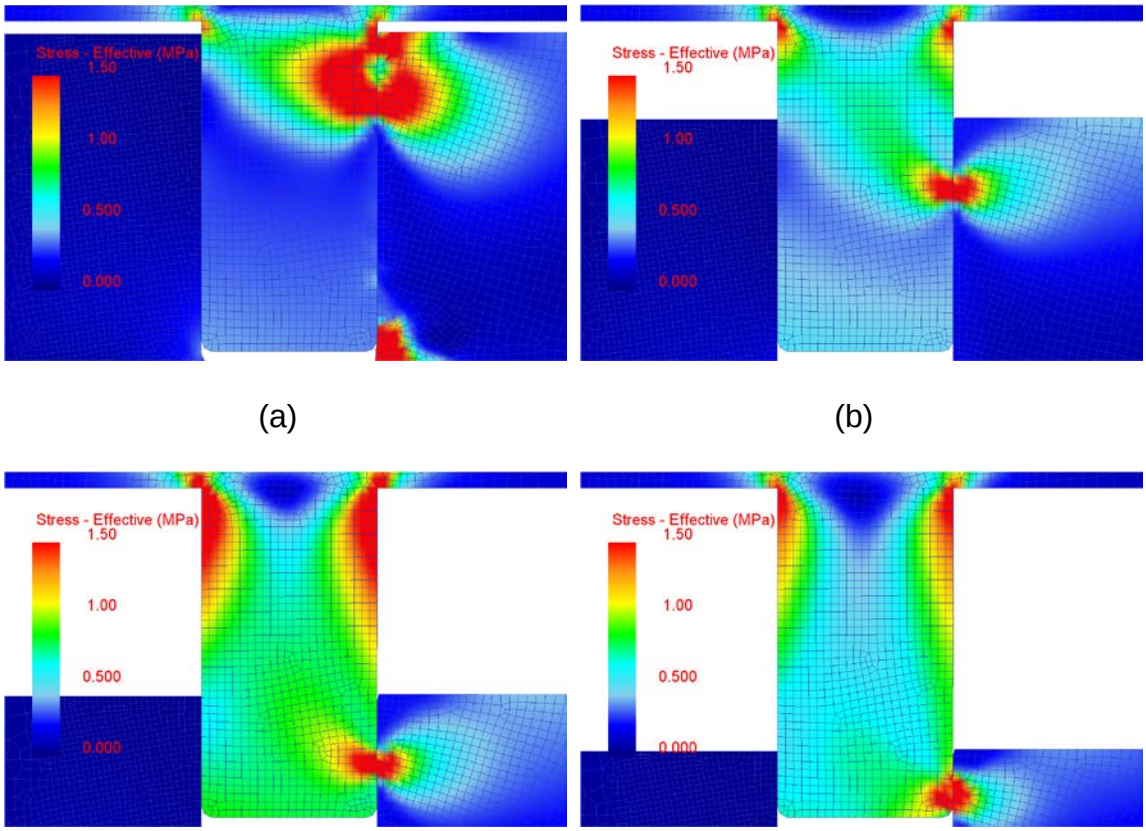

Figure 3.29. Effective stress distribution in the through-hole located at 40 mm from the thermal center, at a molding temperature of 150°C, when the displacement was (a) 25, (b) 250, (c) 500, and (d) 750 μm.

Figure 3.30 shows the flow stress at the bottom edge of the pin during demolding when the pin locations were 0, 10, 20, 30, and 40 mm relative to the thermal center. Stress at the bottom edge of the pin was observed as the radial location of the through-hole was increased. The results of simulation indicated a direct relationship between the effective stress at the edge of the pin and the radial location of the through-hole. As the molding temperature increased, the effective stress during demolding increased due to the higher shrinkage rate of the polymer.

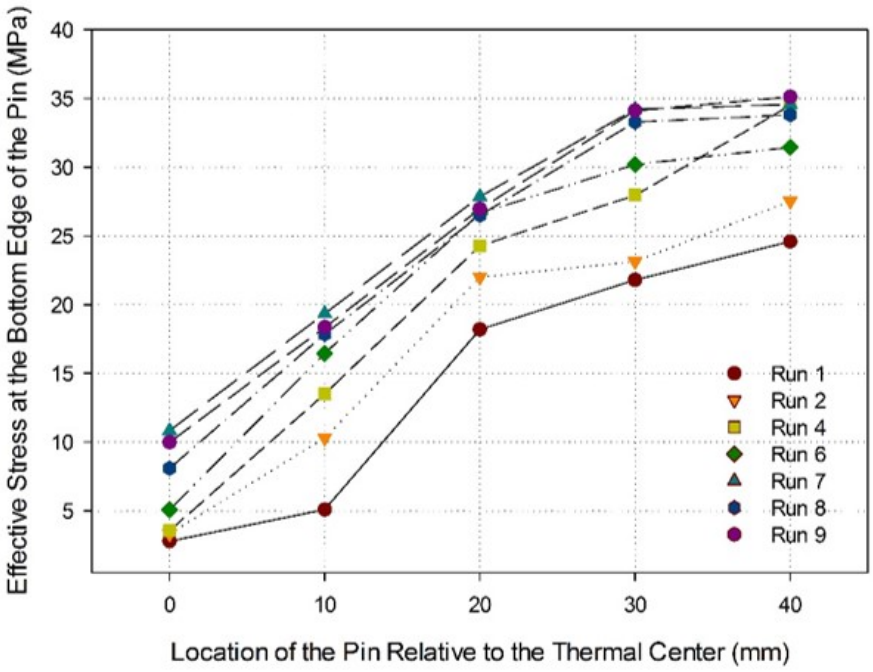

Figure 3.30. Flow stress at the bottom edge of the pin at the end of the demolding step, at radial locations of 0, 10, 20, 30, and 40 mm from the thermal center. When the molding temperatures were 100, 125, and 150°C, the embossing forces were 10, 30, and 50 kN, and the polymer thicknesses were 0.8, 1.5, and 3.0 mm.

3.8. Summary

Finite element simulations were developed to investigate the behavior of the flow front of the polymer during molding, cooling, and demolding. Numerical analyses using DEFORM 2D, predicted the effect of the molding temperatures and embossing forces during molding. Simulation results showed incomplete through-holes at molding temperatures below T_g. Complete Through-holes were achieved at molding temperatures of 125 and 150°C and embossing forces of 10, 30, and 50 kN. Molding temperature significantly affected advance of the flow front, allowing the pin to move into the polymer causing fracture of the residual layer.

The stress evolution and displacement of the polymer substrate and the pin was investigated during cooling and demolding to analyze the effect of thermal stress and adhesion forces on the fabricated through-hole and the mold pin. Simulation results predicted stress concentration at the bottom of the mold pin and at the contact area between the pin and the polymer substrate. The increase in the radial distance of the pin relative to the thermal center directly increased thermal stress on the contact area.

4. HOT EMBOSSING EXPERIMENTS

4.1. Introduction

Hot embossing experiments were performed to study the fabrication of through-holes for microfluidic devices. The experiments could be used to understand the effect of the process parameters in the filling of a mold cavity. Process parameters have been widely studied to understand the flow behavior of a polymer in hot embossing (Gomez et al. 2014; Heckele et al. 2004). Process parameters including molding temperature, embossing force, and the thickness of the polymer have a critical effect on the advance of the flow front in micro hot embossing (Joudkazis et al. 2004).

Experiments were performed to determine the process parameters for the reliable replication of through-holes in microfluidic devices. Molding temperature, embossing force, and the thickness of the polymer were selected as the process parameters included in the experiments. A brass mold insert was designed by CAD software. The mold insert containing nine pins at different radial locations was machined by a CNC milling machine. An oil circulation system was added to the press to reduce the cooling time. The decrease in the cooling time could reduce defects on the molded pattern. Through holes were measured and characterized by the use of the measurement parameters.

4.2. Design and assembly of the cooling system

Cooling of the embossed pattern is a critical step in hot embossing (Song et al. 2008). The cooling rate affects the thermal stress and flow behavior of the polymer. This effect is caused by the difference in the coefficient of thermal expansion

between the polymer and the mold insert (Jin et al. 2009). The proper selection of the cooling rate could significantly reduce cooling defects including deformed, distorted, and broken features (Matthew et al. 2011).

The hot embossing system was modified to reduce the cooling time. The decrease in cooling time could reduce both pattern defects and cycle time. An oil-based cooling system was designed to be added to the press. The system consisted of an oil transfer pump, heat transfer fluid, a heat exchanger, and a cooling fan. Figure 4.1 shows a schematic representation of the cooling system.

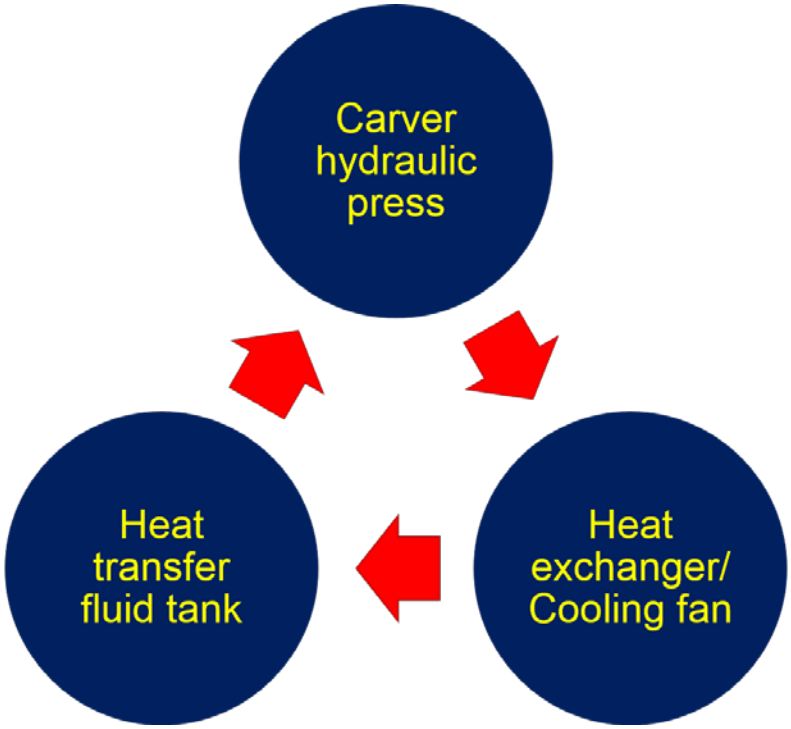

Figure 4.1. Schematic representation of the cooling system indicating the flow direction of the heat transfer fluid.

The oil transfer pump (6X674H, Dayton Electric Mfg. Co., Niles, IL) was used to pump a heat transfer fluid (Paratherm MR, Paratherm Corp., Conshohocken, PA) across the fluid lines inside the top and bottom platens. The heat transfer fluid was pumped to the heat exchanger, where forced convection was applied as shown in Figure 4.2.

The addition of the cooling system offered advantages including a significant decrease in the total time of the embossing cycle, no waste production due to the recirculation of the cooling fluid, and no steam traps were needed when compared to a cooling system based on the circulation of water.

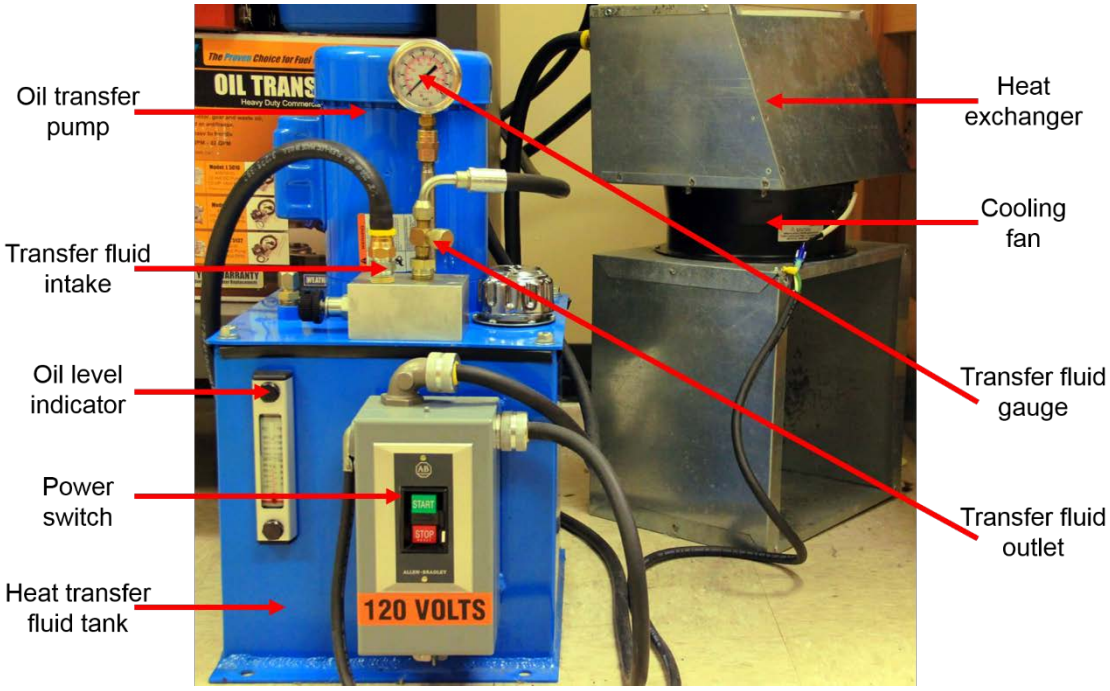

Figure 4.2. Configuration of the cooling system used for the fabrication of through-holes in hot embossing.

4.3. Micro hot embossing experiments

4.3.1. Design and fabrication of the mold insert

The mold inserts were fabricated by machining an ultra-machinable brass alloy 353 (McMaster-Carr, Atlanta, GA). Brass alloy 353 is an economical high strength and high conductivity copper base alloy with a density of 8.75 g/cc which offer several advantages including a tensile strength of 344 MPa, a Brinell hardness of 90, a thermal conductivity of 183 W/m-K, a coefficient of thermal expansion (CTE) of 16.2 µm/m-°C, and an excellent machinability as presented in Table 4.1.

To fabricate the pins, a file with the required patterns was designed by computer-aided design (CAD) software AutoCAD (Autodesk, San Rafael, CA). The CAD file was imported into a computer-aided manufacturing (CAM) software MasterCAM (CNC software Inc., Tolland, CT) to generate the tool path. The mold insert was machined by a computer numerically controlled (CNC) milling machine HAAS MiniMill (Haas Automation Inc., Oxnard, CA).The mold insert contained nine pins at radial locations relative to the center of the mold as shown in Figure 4.3. Pins were located at 0, 10, 20, 30, and 40 mm from the center of the mold insert.

Table 4.1. Material properties of Brass Alloy 353.

Properties	Metric
Density	8.75 g/cc
Tensile Strength	586 MPa
Brinell Hardness	90
Thermal Conductivity	183 W/m-K
CTE	16.2 µm/m-°C

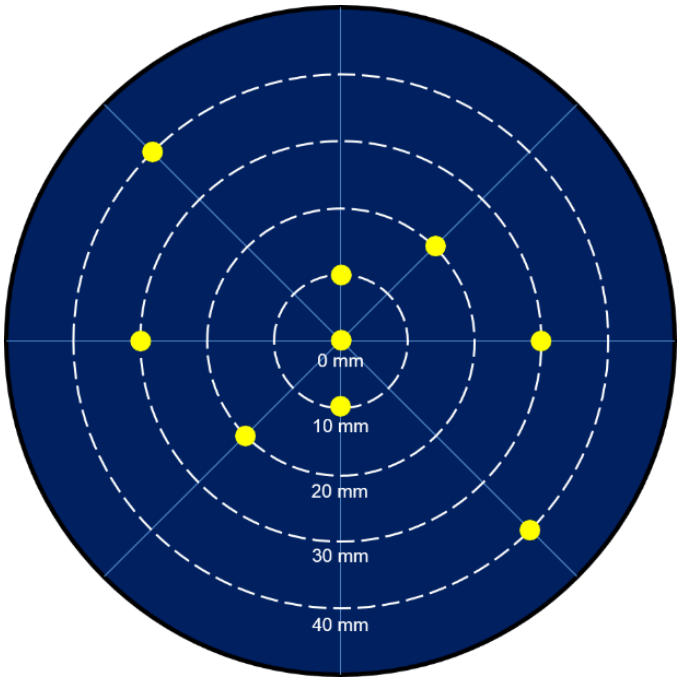

(a)

(b)

Figure 4.3 (a) Schematic representation of the mold insert illustrating the location of the pins at 0 mm, 10 mm, 20 mm, 30 mm, and 40 mm relative to the center of the polymer substrate and (b) Rendered representation of the mold insert pins.

Table 4.2. Dimensions of the fabricated pins including a 95% confidence interval.

Substrate Thickness (μm)	Pin location (mm)	Pin Dimensions	
		Height (μm)	Diameter (μm)
800	0	802.4 ± 2	755.8 ± 2
	10	809.6 ± 2	769.2 ± 2
	20	766.1 ± 3	769.7 ± 3
	30	813.9 ± 2	768.1 ± 2
	40	808.8 ± 3	768.3 ± 3
1500	0	1439.6 ± 5	766.9 ± 5
	10	1434.4 ± 5	768.4 ± 5
	20	1408.3 ± 3	763.7 ± 4
	30	1462.8 ± 5	762.4 ± 3
	40	1462.5 ± 4	763.7 ± 3
2800	0	2469.5 ± 7	760.9 ± 2
	10	2471.6 ± 4	762.5 ± 8
	20	2499.3 ± 9	766.8 ± 5
	30	2489.2 ± 3	764.1 ± 5
	40	2493.1 ± 5	769.4 ± 1

The length of the pin was dependent on the thickness of the polymer. A pin diameter of 800 μm was maintained constant throughout the experimental testing. Table 4.2 shows the dimensions of the pin depending on the polymer selected. To determine the height of the pin, hot embossing experiments were performed using a blank mold. The blank mold was used to determine the compression of the polymer after the embossing cycle. The final thickness of the polymer was measured in relation with the process parameters.

Figure 4.4 shows the machined pins used for the fabrication of through-holes in a polymer with a thickness of 0.8 mm. Figures 4.4 (a), (b), (c), (d), and (e) illustrate the pins at radial locations of 0, 10, 20, 30, and 40 mm, respectively. Machining traces were observed in the mold surface near the pin due to the tool change needed to produce smaller cuts.

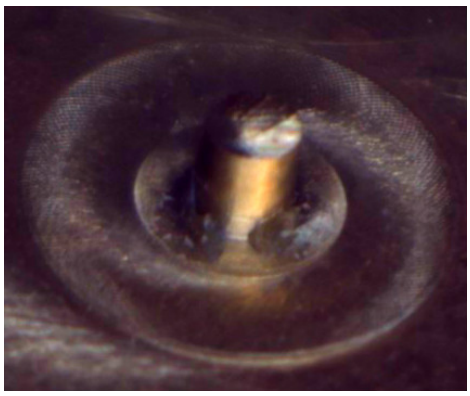

(a)

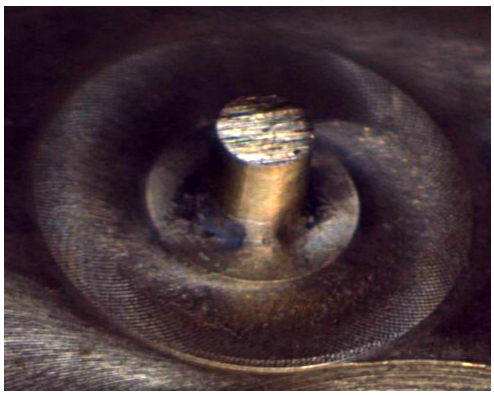

(b)

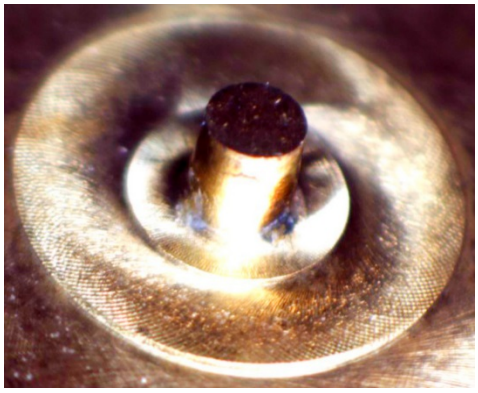

(c)

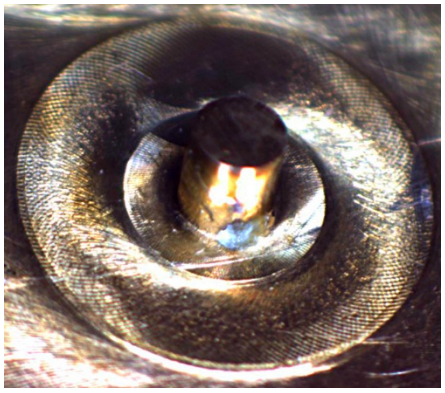

(d)

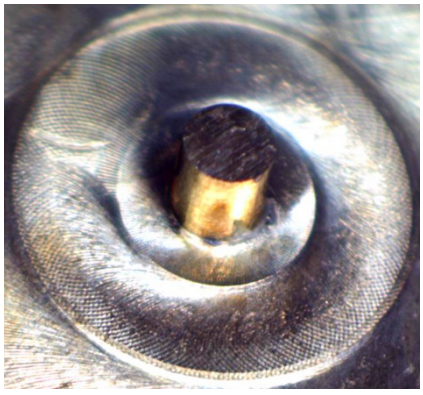

(e)

Figure 4.4. CNC machined mold insert illustrating the 0.8 mm pins at the radial locations of: (a) 0 mm, (b) 10 mm, (c) 20 mm, (d) 30 mm, and (e) 40 mm.

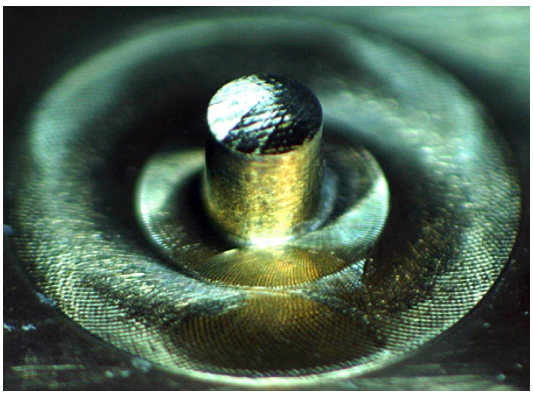

(a)

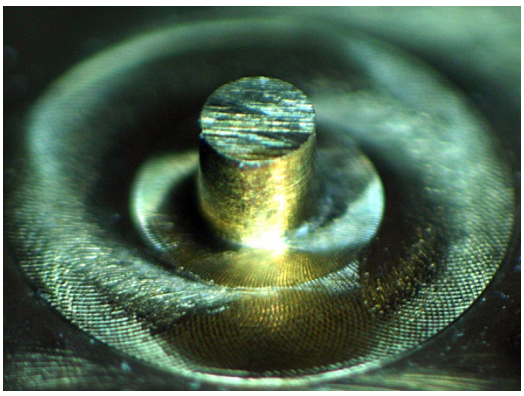

(b)

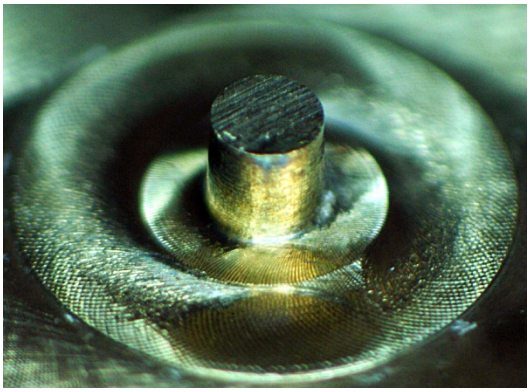

(c)

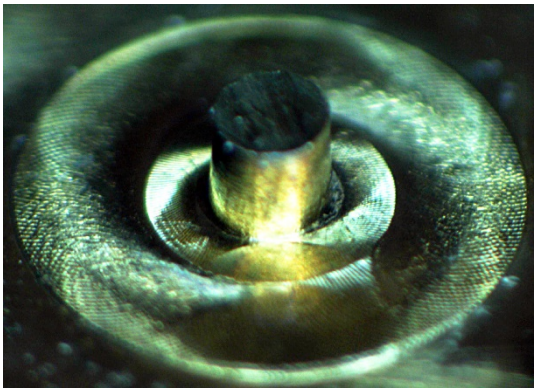

(d)

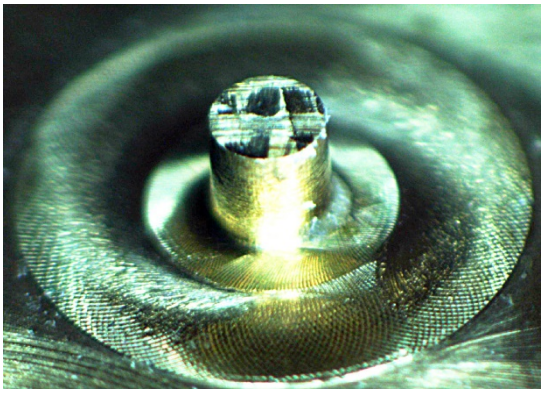

(e)

Figure 4.5. CNC machined mold insert illustrating the 1.5 mm pins at the radial locations of: (a) 0 mm, (b) 10 mm, (c) 20 mm, (d) 30 mm, and (e) 40 mm.

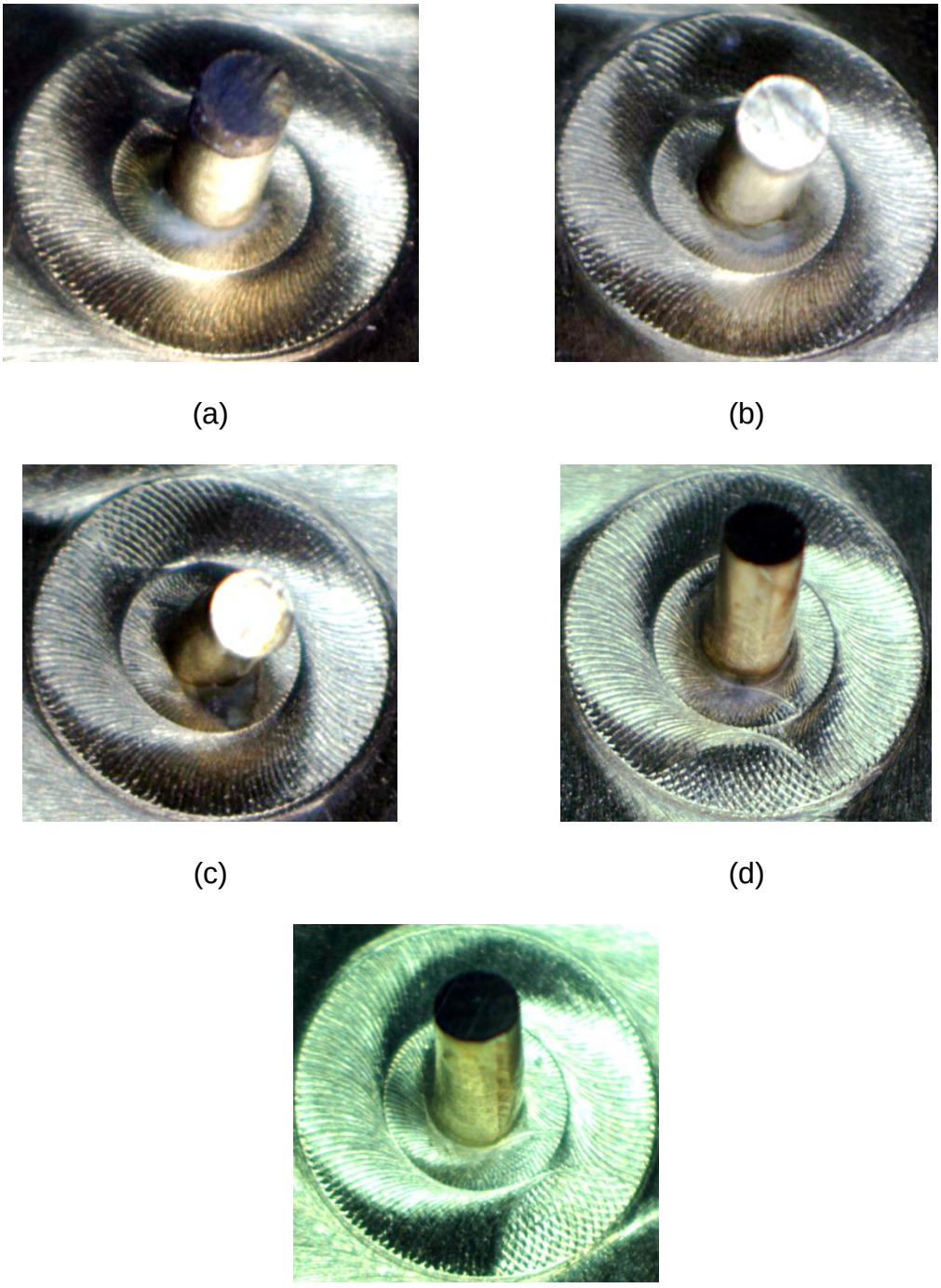

Figure 4.6. CNC machined mold insert illustrating the 3.0 mm pins at the radial locations of: (a) 0 mm, (b) 10 mm, (c) 20 mm, (d) 30 mm, and (e) 40 mm.

The pins used for the fabrication of through-holes in polymers with a thickness of 1.5 and 3.0 mm are shown in Figures 4.5 and 4.6, respectively. Machining traces were observed in all the pins due to the removal of material in the fabrication process. A top view of the machined pin is shown in Figure 4.7.

Different patterns were observed at the top of the pin and the surface of the mold insert. The patterns were caused by the end mills using on the process. The machining traces located in the surface of the mold insert could be used as a visual test for complete cavity filling. The traces on the mold insert could be transferred to the polymer when complete cavity filled is achieved.

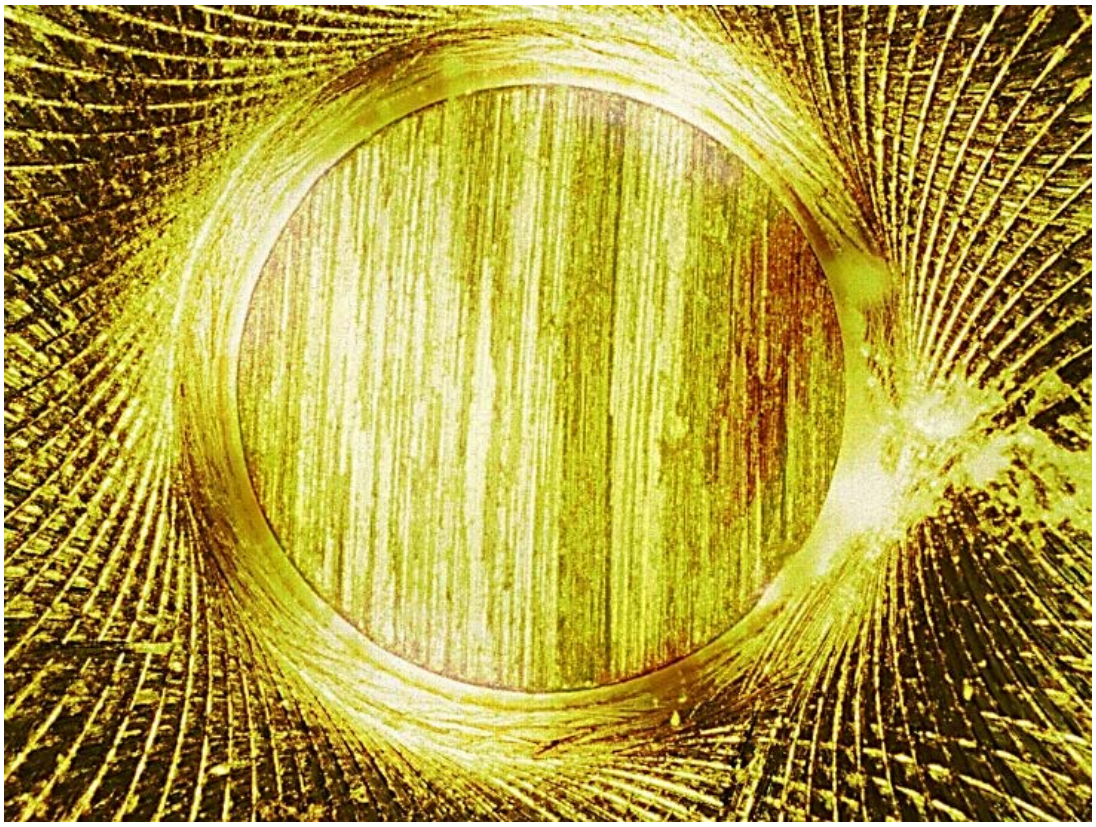

Figure 4.7. Top view of the CNC machined pin.

Figure 4.8. Image of the mold insert illustrating the radial location of the pins used to fabricate interconnects in an 800 µm polymer.

Figure 4.8 shows a complete view of the mold insert containing the pins located at radial directions relative to the center. The mold insert is located on the aluminum plate, showing the screws used to tighten it the press. A contour shape was machined to eliminate contact between the mounting screws and the polymer. The contact between the mounting screws and the polymer could increase the adhesion force preventing the separation from the mold and the polymer.

4.3.2. Materials

4.3.2.1. Polymer layer

PMMA (Plexiglass®, Sabic plastics, Shanghai, China) is a common polymer used in bioMEMS applications due to its compatibility with human tissue. It is an acceptable substrate for medical research for the fabrication of Lab-on-a-Chip (LOC) devices.

Table 4.3. Material properties of PMMA.

Properties	Metric
Density	1.15 g/cc
Glass Transition Temperature	105°C
Young's Modulus	3100 MPa
Poisson's Ratio	0.4
CTE	8e-6 K^{-1}
Thermal Conductivity	0.24 W/m-K

PMMA is a transparent thermoplastic used in a wide range of fields and applications including automotive, personal care, and construction industries. Among its most important properties are a density of 1.15 g/cc, it has an impact strength higher than glass but lower than polycarbonate (PC), a glass transition temperature of approximately 105°C, a Young's modulus of 3100 MPa, a Poisson's ratio of 0.4, a CTE of 8e-6 K^{-1}, and a thermal conductivity of 0.24 W/m-K as represented in Table 4.3. PMMA was obtained in films of 6 x 6 inches with thicknesses of 0.8, 1.5, and 2.8 mm.

4.3.2.2. Buffer layer

PSU (Colorcomp™, Sabic plastics, Shanghai, China) is a thermoplastic polymer widely used thanks to its toughness and stability at high temperatures and commonly used as a replacement for polycarbonates.

Table 4.4. Material properties of PSU.

Properties	Metric
Density	1.24 g/cc
Glass Transition Temperature	175°C
Young's Modulus	2480 MPa
Poisson's Ratio	0.37
CTE	5e-6 K^{-1}
Thermal Conductivity	0.26 W/m-K

Table 4.4 presents the material properties of PSU. A density of 1.24 g/cc, a T_g of 175°C, a Young's modulus of 2480 MPa, a Poisson's ratio of 0.37, a CTE of 5e-6 K^{-1}, and a Thermal conductivity of 0.26 W/m-K are considered among the principal material properties of Polysulfone.

4.3.3. Process conditions

The carver thermal press (3893 4NE18, Wabash, IN) used for the experiments is shown in Figure 4.9. A hydraulic cylinder was used to guide the bottom heating and cooling platen vertically to the top heating and cooling platen. The mold insert, containing the pins at radial locations, was mounted at the center of the top aluminum platen. The polymer and the buffer were placed on the bottom aluminum platen.

Prior to embossing, the polymers were dehydrated at 80°C for a period of at least four hours in a convection oven (Quincy Lab Inc., 31-350ER-1). Dehydration should not exceed sixteen hours to prevent the denaturalization of the polymer. After the pretreatment, the polymer was sprayed using a nitrogen gun to remove particulate material from the surface.

The polymer was placed inside the hydraulic press on top of the buffer layer for a period of 15 minutes to allow the polymer to reach the thermal equilibrium state. Mold release agent (Mold Wiz F-57 NC) was sprayed to the mold to reduce friction as well as the risk of damaging the molded patterns during demolding.

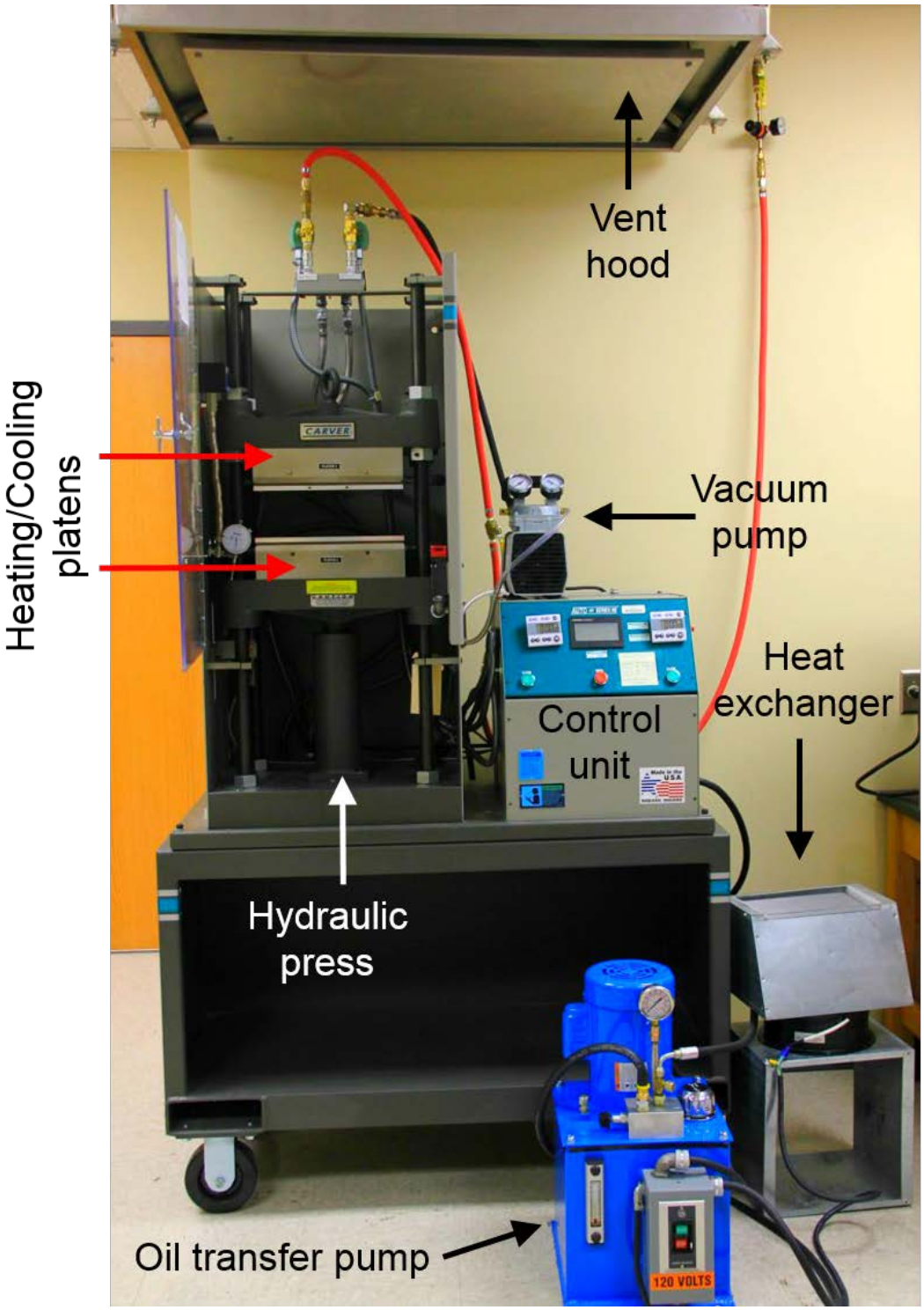

Figure 4.9. Overview of the Carver Thermal Press 3893 4NE18 used in fabrication of polymer interconnects in hot embossing.

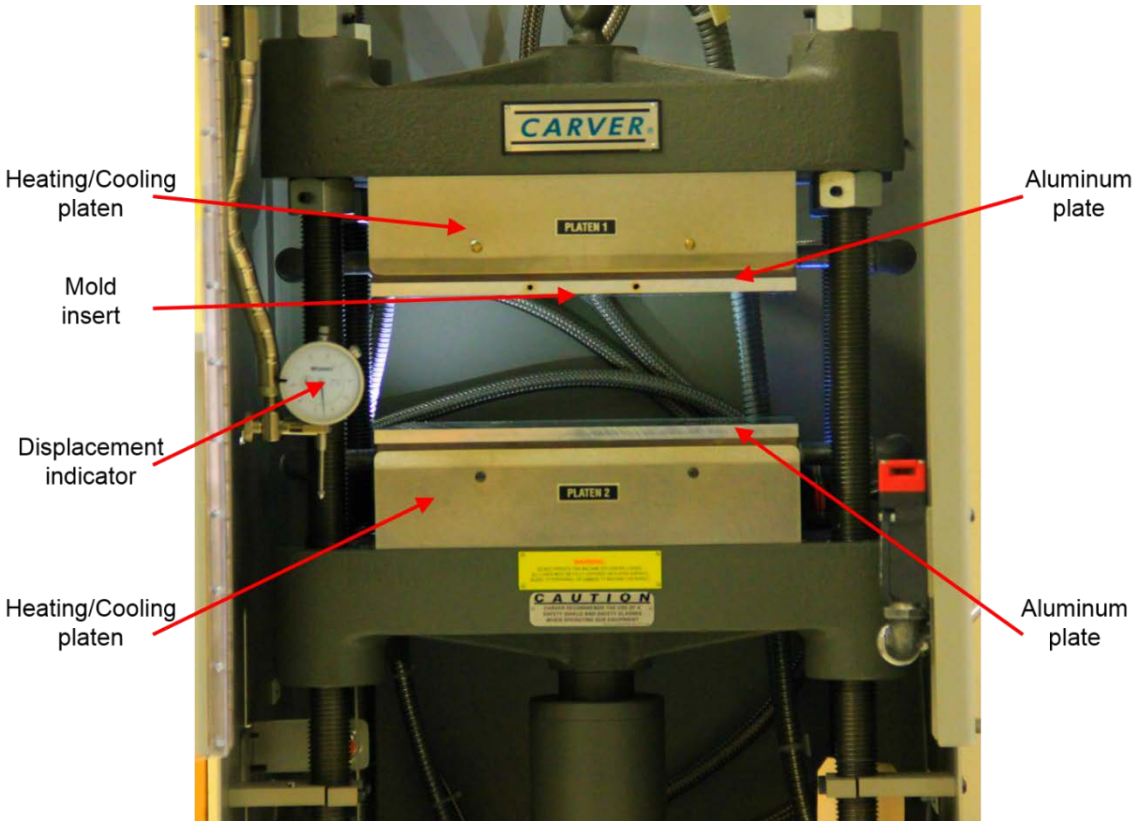

Figure 4.10. Image of the Carver Thermal Press 3893 4NE18 illustrating the heating and cooling platens, location of mold insert, and displacement indicator.

Process parameters applied in micro hot embossing experiments are shown in Table 4.5. Embossing forces of 10, 30, and 50 kN, molding temperatures of 100, 125 and 150°C, thickness of the polymer of 0.8, 1.5, and 2.8 mm, a holding time of 5 minutes, and an embossing speed of 5 mm/min were used in the experiments. Molding temperatures and forces were set by the control unit and maintained constant throughout the embossing process. A dial indicator (Westward model 2YNK2) was fixed to the press to measure the displacement of the bottom platen a shown in Figure 4.10. The dial indicator measured the distance the bottom platen traveled to make contact with the top platen.

Table 4.5. Design of experiment for the fabrication of through-holes in polymer microfluidic devices.

Run	Molding Temperature (°C)	Embossing Force (kN)	Substrate Thickness (mm)
1	100	10	0.8
2	100	30	1.5
3	100	50	3.0
4	125	10	1.5
5	125	30	3.0
6	125	50	0.8
7	150	10	3.0
8	150	30	0.8
9	150	50	1.5

Once the holding time was completed, the cooling system was started to bring the embossed patterns and the mold to a demolding temperature. The press was cooled until it reached a temperature of 80 ± 5°C.

4.4. Characterization of the fabricated through-holes

Characterization of through-holes was performed by the estimation of the measurement parameters of the fabricated through-holes using a measurescope (MM-800, Nikon, Japan) and a Scanning Electron Microscope (SEM) (Helios NanoLab 400, FEI, Hillsboro, OR).

Dimensional and shape variations, as well as roundness, and tapering of the fabricated through-hole were measured. Figure 4.11 (a) and (b) illustrate the schematic and SEM image of the measurement parameters used to determine the reliability of the fabricated through-holes, respectively.

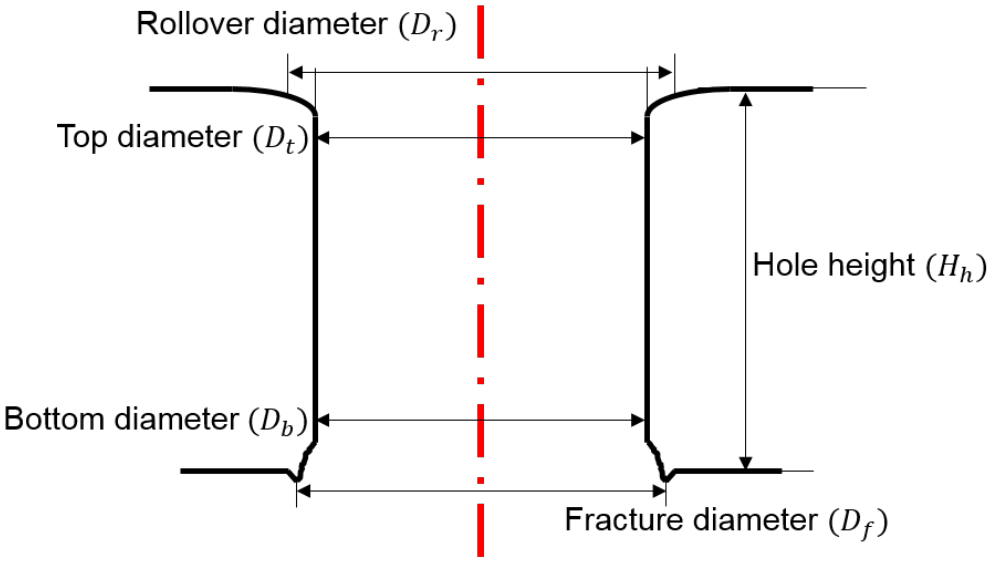

(a)

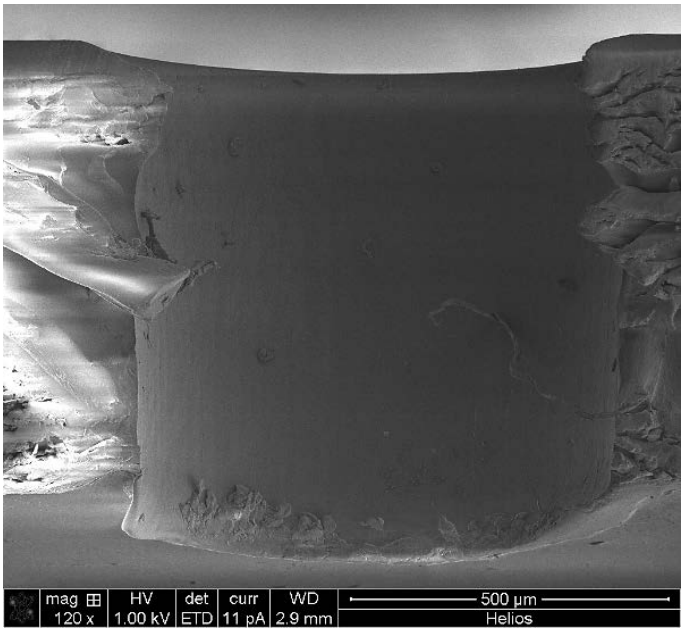

(b)

Figure 4.11. (a) Schematic representation of the measurement parameters for the characterization; (b) SEM image showing the cross-sectional area of the fabricated through-hole.

The measurement parameters include top diameter (D_t), which is located in the top surface of the hole and caused by the initial penetration of the pin into the polymer. The bottom diameter (D_b), located at the bottom surface where fracture was expected. The fracture diameter (D_f) caused by the separation of the residual layer from the polymer, and the through-hole height (H_h). The measurement parameters could assist to determine the quality of the fabricated through-holes by quantifying the variation of the structure.

4.5. Results of the hot embossing experiments

Hot embossing experiments were performed to analyze the fabrication of through-holes. Experimental hot embossing included the preparation of samples, the hot embossing cycle, and the characterization of the fabricated through-holes. Samples were prepared by dehydration during the preheating cycle. Molding temperatures, embossing forces, and thickness of the polymer were the process parameters selected for the experiments. Each combination of process parameters was performed in triplicates.

The measurement parameters were characterized with the use of a measurescope, where three measurements were estimated from three different reference points for statistical validity.

Measurescope images of the fabricated through-hole at a molding temperature of 100°C, an embossing force of 10 kN, and a thickness of polymer of 0.8 mm is shown in Figure 4.12.

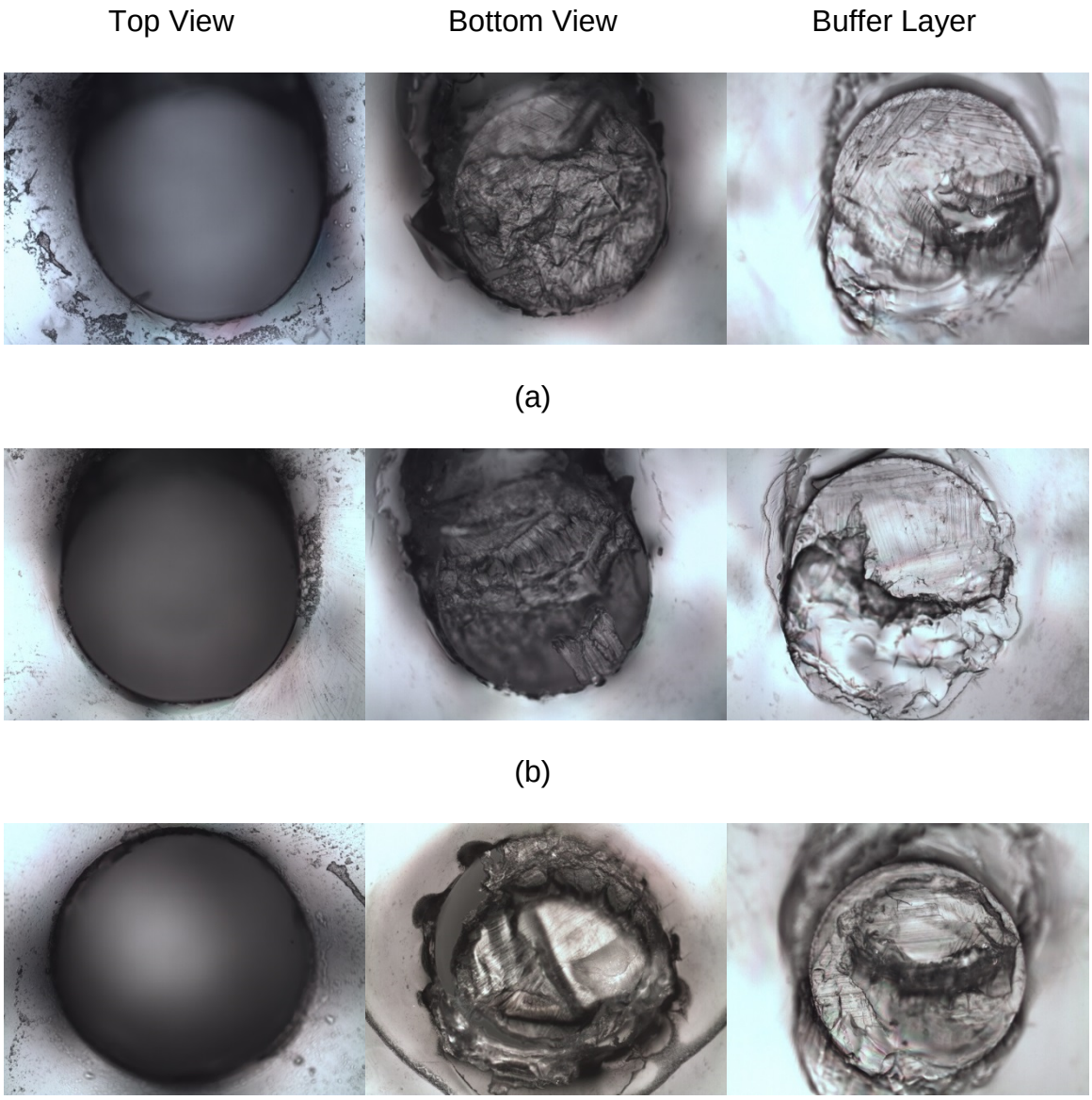

Figure 4.12. Measurescope images of the fabricated through-hole including top view, bottom view, and buffer layer; at a molding temperature of 100°C, an embossing force of 10 kN, and a thickness of the polymer of 0.8 mm; at radial locations of (a) 0, (b) 20, and (c) 40 mm.

The results of experiments showed the incomplete fabrication of through-holes as shown by the bottom view in Figures 4.12 (a), (b), and (c). Clean and round holes were observed at the top surface of the polymer. However, there was no fracture on the residual layer as illustrated by the bottom views. Incomplete cavity filling was determined by the lack of machining traces from the mold insert on the polymer. Partial fracture of the residual layer was observed in the bottom view of Figure 4.12 (c). A separation between the polymer and the residual layer was observed on the top-right quadrant of the incomplete through-hole. The buffer layer in Figures 4.12 (a), (b), and (c) illustrate the location were the embossing force from the pin was applied. Polymer concentration is observed due to the reduction of the residual layer and the increase in pressure at the buffer layer.

SEM images of the fabricated through-holes are shown in Figure 4.13. Top views including a 30° tilt view are included in Figure 4.13 (a). The residual layer was observed inside the through-hole indicating incomplete separation from the polymer. Sidewall damage was caused by the displacement of the pin. Signs of cracking were observed in the sidewall of the polymer due to the reduced molding temperature. At a molding temperature of 100°C the fluidic resistance of the polymer is high causing it to crack and fail. Figure 4.13 (b) illustrates a magnification of the defects observed at the top of the through-hole. The increased rollover diameter was caused by the incomplete mold filling. The bottom view of the polymer layer is shown in Figure 4.13 (c). As observed in Figure 4.13 (a), the residual layer remained attached to the polymer layer.

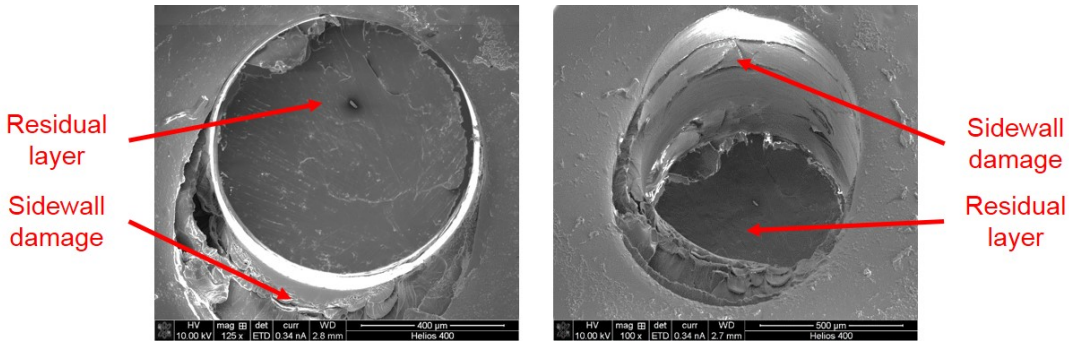

(a)

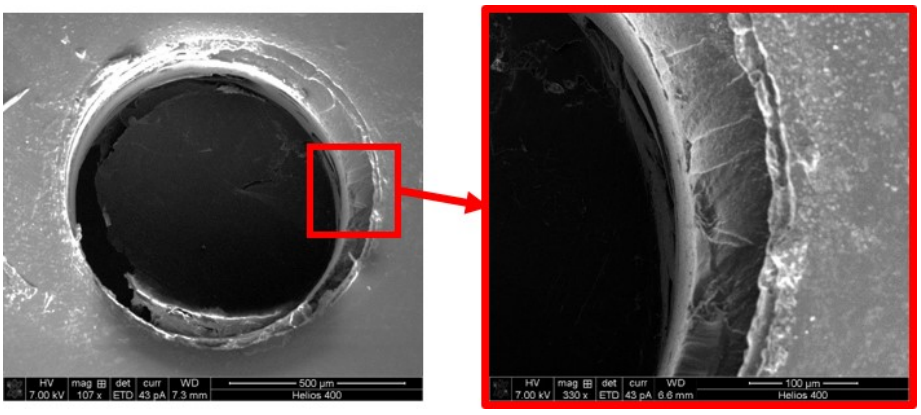

(b)

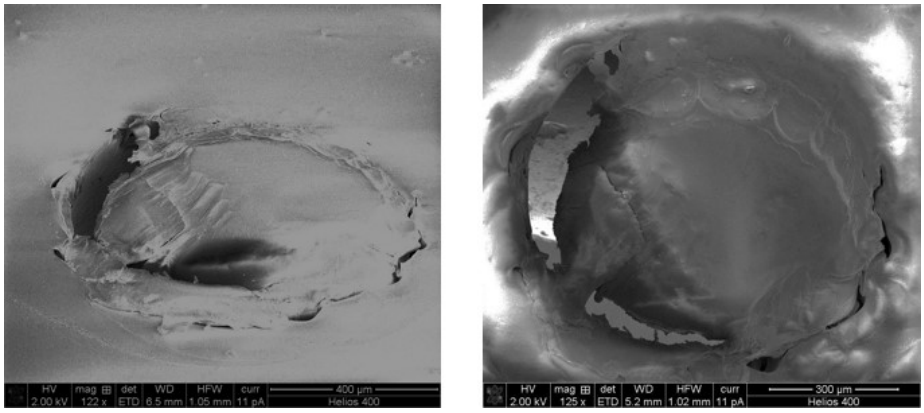

(c)

Figure 4.13 SEM images of the fabricated through-holes at a molding temperature of 100°C, an embossing force of 10 kN, and a thickness of the polymer of 0.8 mm. (a) Top view; (b) sidewall damage; and (c) bottom view.

The results of the measurement parameters for the fabricated through-holes at the process parameter defined in Figure 4.12 are shown in Figure 4.13. The diameter of fracture could not be estimated since there was no separation between the residual layer and the polymer. Figure 4.14 (a) shows the rollover diameter (D_r) of the fabricated through-hole depending on the location of the pin. The rollover diameter was estimated at the top surface of the polymer which was caused by the squeeze flow of the polymer during molding. No significant relation between the location of the pin and the rollover diameter was observed. The highest D_r of 837.20 ± 0.35 µm was observed on the pin located at 20 mm from the thermal center.

Figure 4.14 (b) presents the results of measurement of the diameter at the top of the through-hole. The diameter of the through-hole is directly related with the diameter of the pin. A through-hole with a reduced diameter was observed at the center of the mold due to the tolerances of the CNC used to machine the mold insert. The diameter of the pin located at the center was 755.40 ± 2 µm. The variation in the diameter of the pins located at the other radial locations was not significant. The height of the fabricated through-holes is shown in Figure 4.14 (c). The difference in the height of the through-holes could be caused by the leveling of the platens which led to higher embossing forces at the edges. Incomplete heights of through-holes of 647.70 ± 0.17, 651.40 ± 0.26, 667.63 ± 0.25, 669.37 ± 0.38, and 669.27 ± 0.57 µm were observed at the radial locations of 0, 10, 20, 30, and 40 mm, respectively.

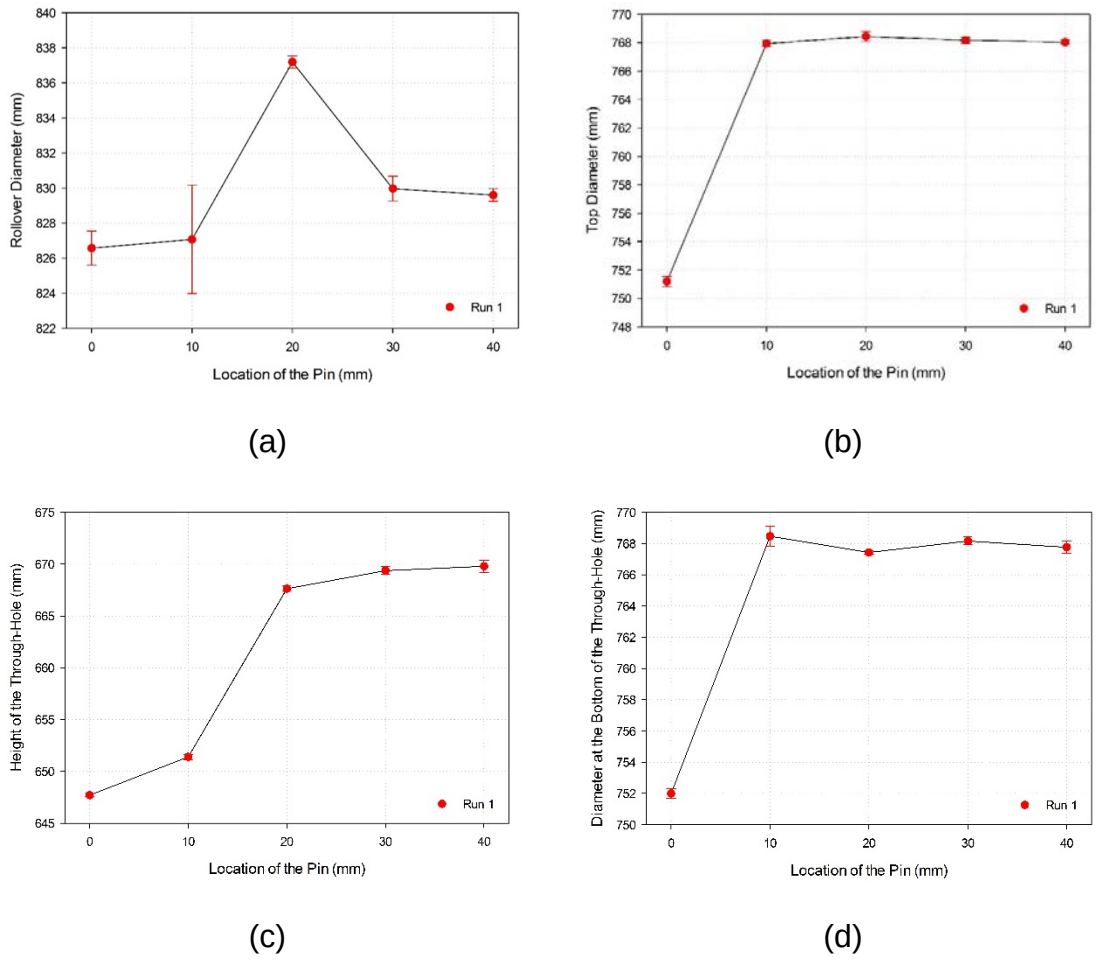

Figure 4.14. Means and confidence intervals of the measurement parameters relative to the location of the pin at a molding temperature of 100°C, an embossing force of 10 kN, and a polymer thickness of 0.8 mm; (a) Rollover diameter, (b) Top diameter, (c) Through-hole height, and (d) Bottom diameter.

The distribution of the diameter measured at the bottom of the through-hole is shown in Figure 4.14 (d). The dimensions of the top and bottoms of the through-hole were comparable with the diameter of the pin.

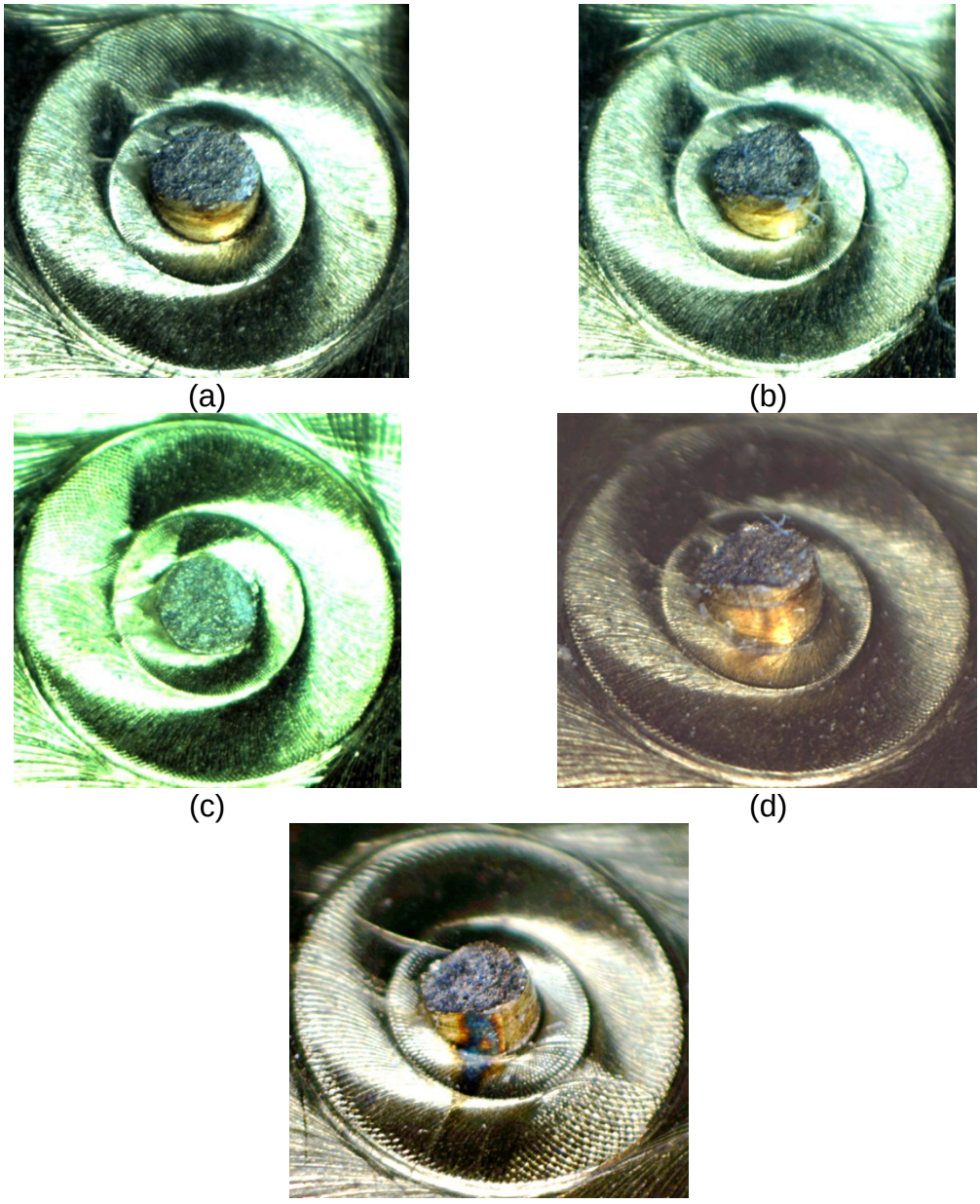

Figure 4.15. Stereoscopic images indicating fracture of the pin at a molding temperature of 100°C, an embossing force of 50 kN, and a polymer thickness of 3.0 mm, at radial locations of (a) 0, (b) 10, (c) 20, (d) 30, and (e) 40 mm.

Fracture of the pin at a molding temperature of 100°C, an embossing force of 50 kN, and a thickness of the polymer of 3.0 mm is shown in Figure 4.15. The low molding temperature, as well as the increased embossing force caused the failure of the pins. Figures 4.15 (a), (b), (c), (d), and (e) show the fracture of the pin at radial locations of 0, 10, 20, 30, and 40 mm, respectively.

Results of hot embossing experiments at a molding temperature of 100°C correlated with the results of simulation. The increase in the length of the pin recued the aspect ratio of the structure. Fracture of the pin was observed at the top edge of the pin at the interface with the base of the mold insert.

The complete fabrication of through-holes when the molding temperature was 125°C, the embossing force was 10 kN, and the thickness of the polymer was 1.5 mm is shown in Figure 4.16. Complete cavity filling was achieved as observed by the machining traces in Figures 4.16 (a), (b), and (c). The marks on the polymer were generated when the flow front reached the boundary of the mold. The bottom view on Figures 4.16 (a) and (c) illustrate complete through-holes. The residual layer was not present of the bottom of the polymer but it could be seen in the indentation generated on the buffer layer. Burrs were observed at the bottom view of the through-hole.

The shape of the burr was irregular and located on the right side along the circumference of the through-hole. The burr was caused by the fracture of the polymer which was pressed by the pin until it reached its yield point. The residual layer on Figure 4.16 (a) was observed by the difference in depth at the indentation. The residual layer in Figures 4.16 (c) was not observed.

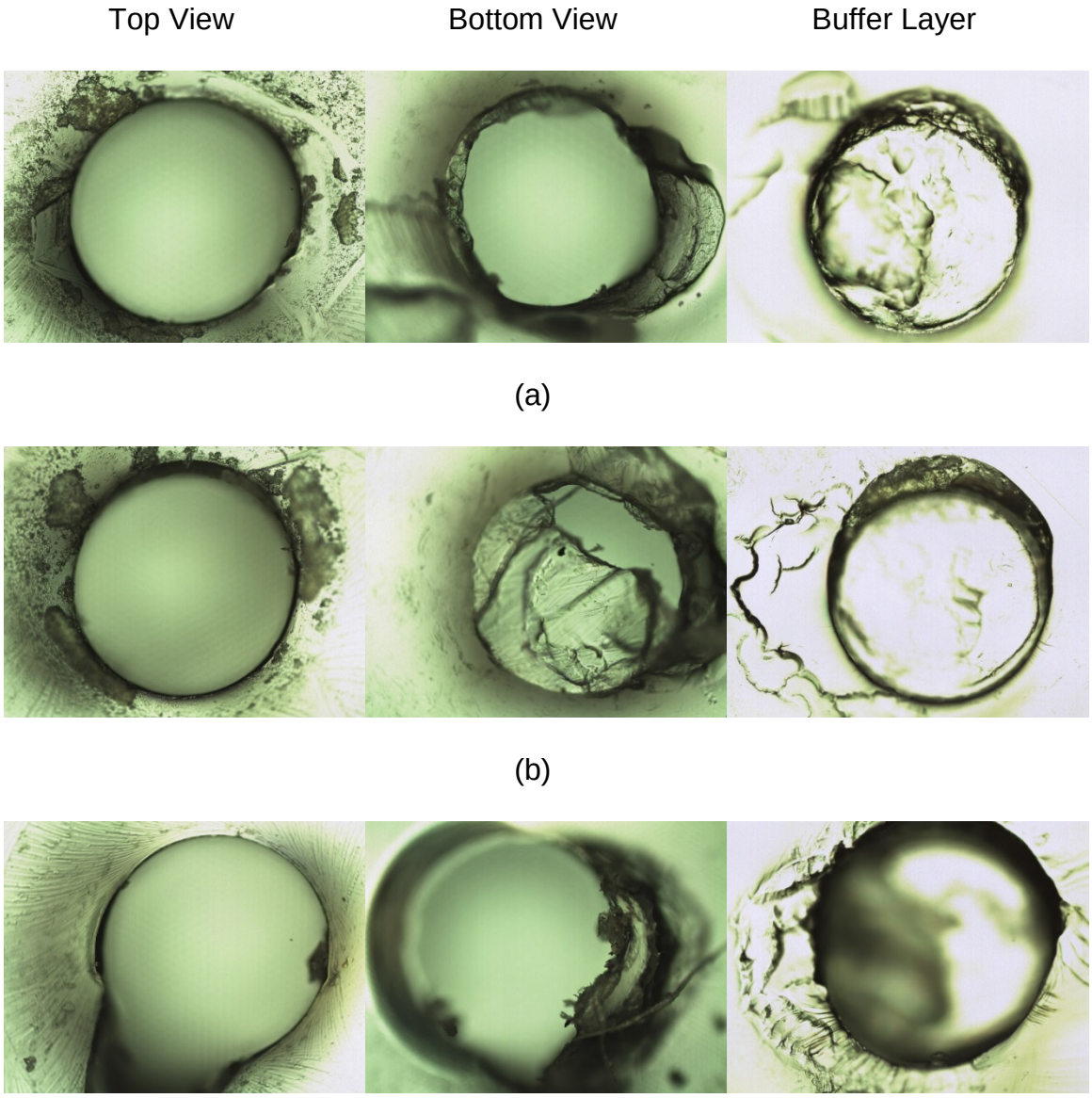

Figure 4.16. Measurescope images of the fabricated through-hole including top view, bottom view, and buffer layer; at a molding temperature of 125°C, an embossing force of 10 kN, and a thickness of the polymer of 1.5 mm; at radial locations of (a) 0, (b) 20, and (c) 40 mm.

Stereoscopic images of an incomplete through-hole and the defects observed in Figure 4.16 are shown in Figure 4.17. The incomplete through-hole fabricated by the pin located at 20 mm relative to the thermal center is shown in Figure 4.16 (a). Fracture of the residual layer was observed. However, a significant portion of the residual layer remained, generating a partial blind hole. A portion of the residual layer can be observed on the buffer layer of Figure 4.17 (b).

The residual layer was identified by matching the shape of the partial through-hole with the shape of the partial residual layer observed in the indentation. Figure 4.17 (b) illustrates the elongation of the sidewall. This could be caused by the bending of the pin. The bent pin pushed the sidewall of the through-hole in demolding. Spring back could have caused the pin to apply pressure at the top edge of the sidewall causing pattern deformation. The spring back effect is caused by the release of pressure from the pin.

Figure 4.18 illustrate the SEM images of the fabricated through-holes at a molding temperature of 125°C, an embossing force of 10 kN, and a polymer thickness of 1.5 mm. Clean and round through-holes were observed when the molding temperature was increased as shown in Figure 4.18 (a). The residual layer was completely separated from the polymer as illustrated in the bottom view of Figure 4.18 (b). The residual layer was observed on the surface of the buffer layer as presented in Figure 4.18 (c). The magnified area illustrates both the residual layer and the buffer layer. The residual layer was identified by the pattern transferred from the bottom of the pin. The machining traces observed indicated that the buffer layer acted as a residual layer receptor.

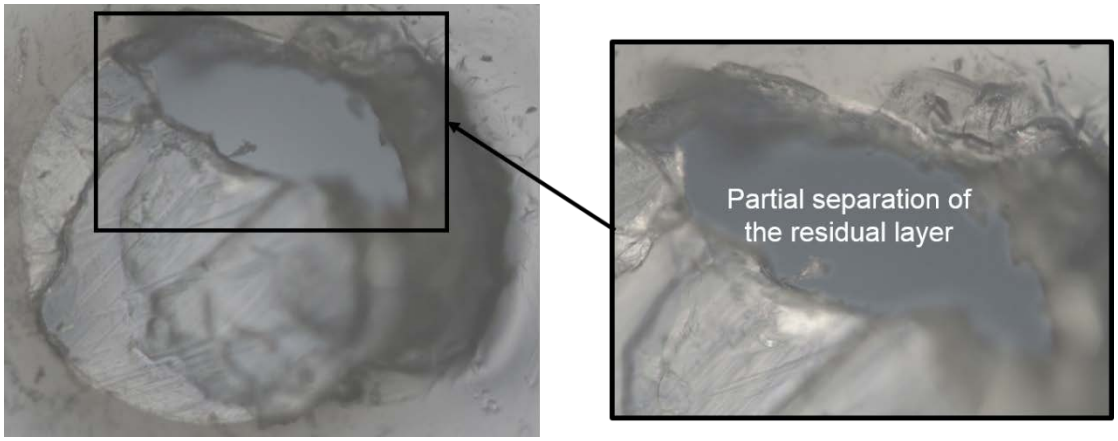

(a)

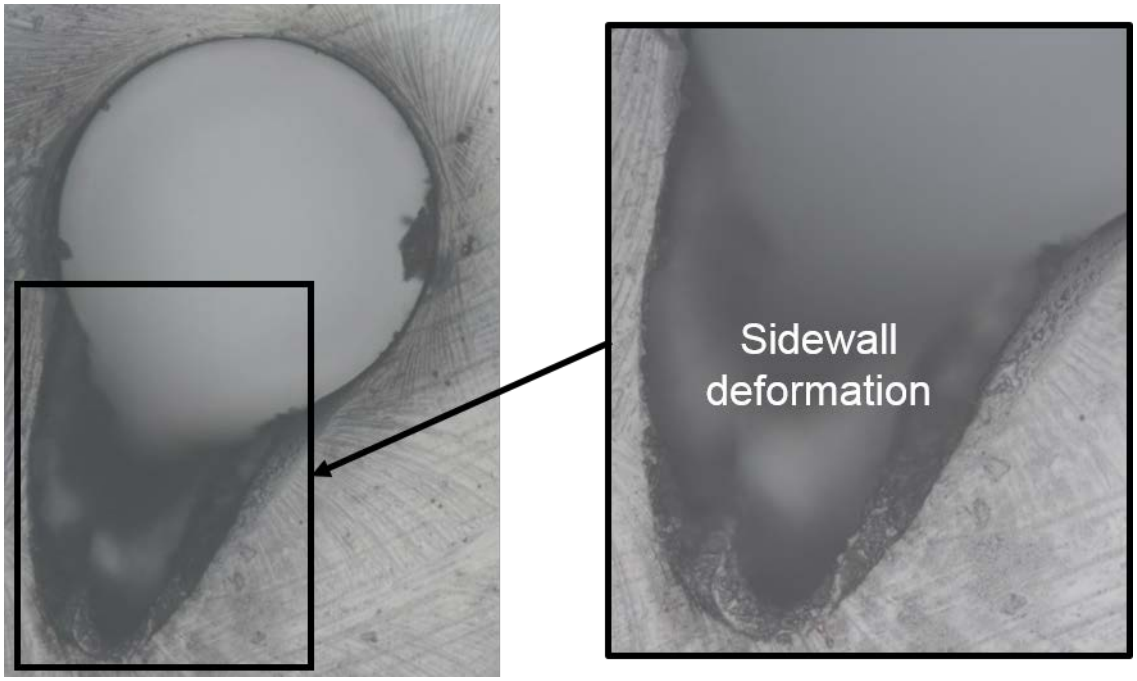

(b)

Figure 4.17. Fabrication defects observed at a molding temperature of 125°C, an embossing force of 10 kN, and a polymer thickness of 1.5 mm. (a) Incomplete through-hole; (b) sidewall deformation.

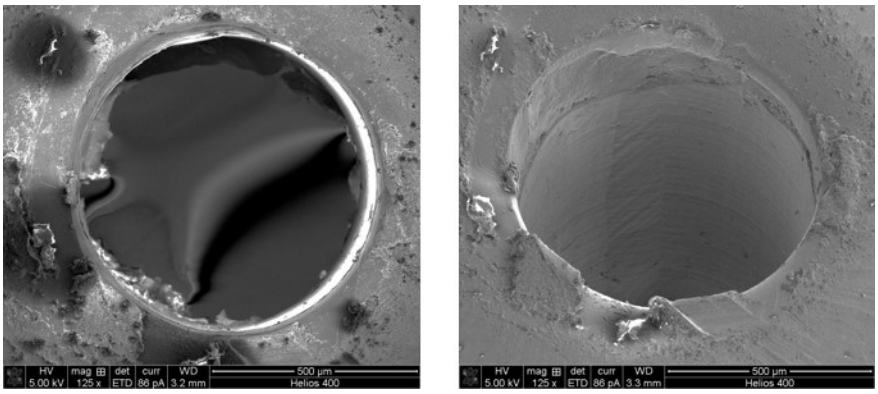

(a)

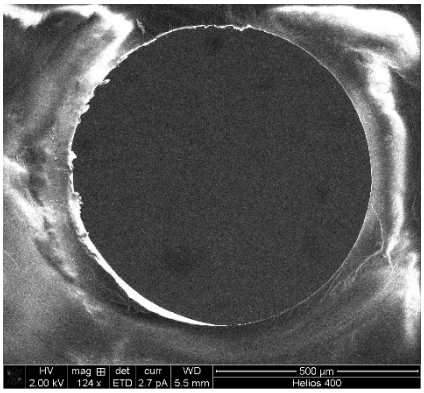

(b)

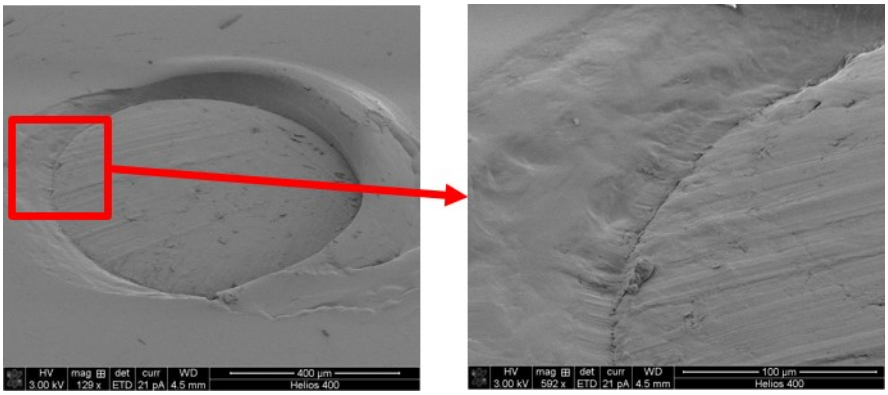

(c)

Figure 4.18 SEM images of the fabricated through-holes at a molding temperature of 125°C, an embossing force of 10 kN, and a thickness of the polymer of 1.5 mm. (a) Top view; (b) bottom view; and (c) buffer layer.

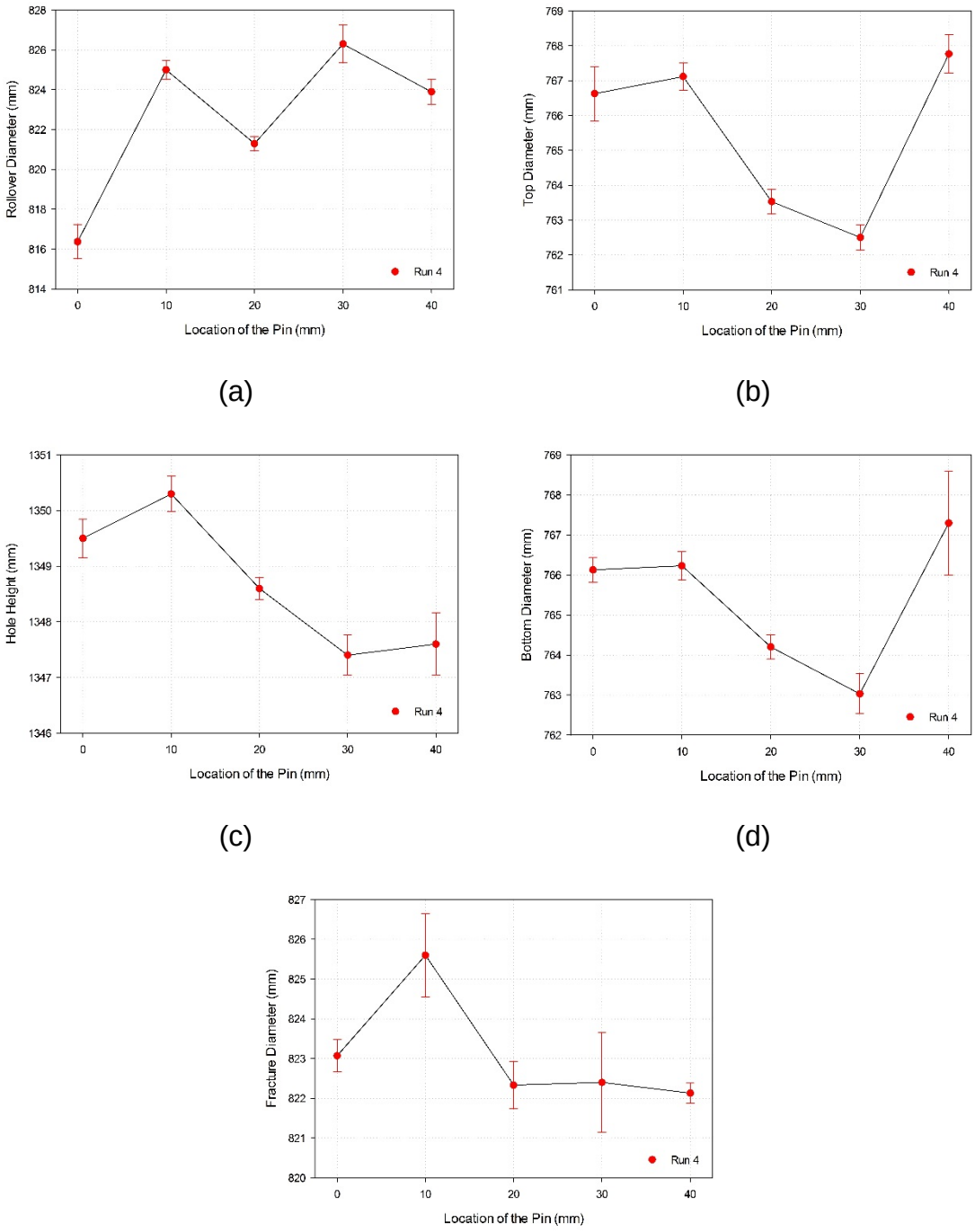

Figure 4.19. Means and confidence intervals of the measurement parameters relative to the location of the pin at a molding temperature of 125°C, an embossing force of 10 kN, and a polymer thickness of 1.5 mm. (a) Rollover diameter, (b) Top diameter, (c) Through-hole height, and (d) Bottom diameter.

Sidewall elongation and the spring back effect were not observed on the results of the simulations. The occurrence of the observed defects was not taken into consideration in the numerical model to simplify the calculation.

The statistical data for the measurement parameters at a molding temperature of 125°C, an embossing force of 10 kN, and a thickness of polymer of 1.5 mm is shown in Figure 4.19. The figure illustrates the mean and confidence interval when the pin location was 0, 10, 20, 30, and 40 mm relative to the thermal center. Figure 4.19 (a) shows the rollover diameter of the fabricated through-holes. The rollover diameter at the center of the mold was lower than the observed at the other locations. The mean diameter at the center was 816.37 ± 0.84 μm. This could be caused by the thermal shrinkage of the polymer during cooling.

Figures 4.19 (b) and (d) represent the top and bottom diameters, respectively. The results observed in Figure 4.14 is supported by the trend observed in the figures. The trend sows that the diameters at both the top and bottom of the through-hole are directly related with the diameter of the pin. The mean diameters at the top and bottom of the through-holes were closely correlated. The height of the fabricated through-holes is shown in Figure 4.19 (c). The difference in the height of the through-hole could be caused by the variations in the flatness of the aluminum platen and the buffer layer. A maximum height of 1,350.3 ± 0.35 μm was observed at the through-hole located at 10 mm relative to the thermal center.

The diameter of fracture at the bottom of the through-hole is shown in Figure 4.19 (e). The higher fracture diameter was observed at 10 mm from the center. This could be related with the increased height of the through-hole illustrated in

Figure 4.19 (c). The elevated height could cause an increase in the shear deformation of the residual layer, generating a higher diameter. This could explain the relation between the height of the through-hole and the diameter of fracture.

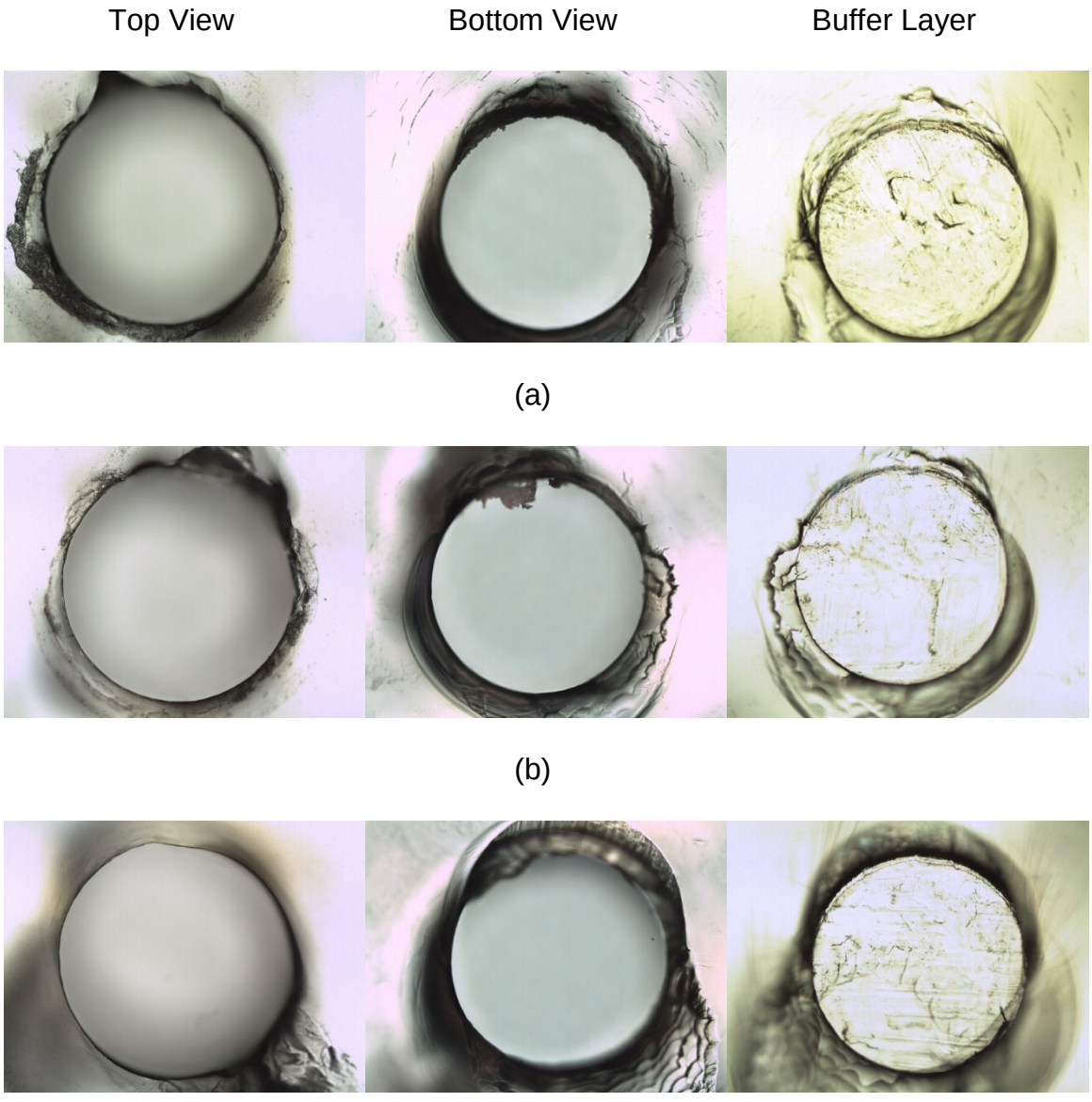

Figure 4.20. Measurescope images of the fabricated through-hole including top view, bottom view, and buffer layer; when the molding temperature was 125°C, the embossing force was 50 kN, and the thickness of the polymer was 0.8 mm; at radial locations of (a) 0, (b) 20, and (c) 40 mm.

Figure 4.20 illustrate the fabrication of complete through-holes at a molding temperature of 125°C, an embossing force of 50 kN, and a thickness of polymer of 1.5 mm. The pin compressed the polymer until it the residual layer was formed. The indentation generated on the buffer layer trapped the remaining polymer until the bottom edge of the pin contacted the residual layer. A reduction on the thickness of the residual layer was caused by the stretching of the polymer. The decreased thickness of the residual layer led to the contact between the pin and the buffer layer, generating fracture.

The increase in the embossing force allowed for the fabrication of cleaner edges at both the top and bottom of the through-hole as shown in Figures 4.20 (a), (b), and (c). No elongation of the sidewall of the through-hole and incomplete through-holes were observed when compared with the results of experiments in Figure 4.16. Machining traces from the pin were observed in the indentation of the buffer layer, indicating the presence of the residual layer.

Figure 4.21 illustrates the SEM images of the fabricated through-holes. Machining traces were observed on the top view of the through-holes as shown in Figure 4.21 (a). The ring observed around the edge of the hole was transferred from the mold insert and was caused by the change of tool during the fabrication of the mold. Round and clear edges are observed in the bottom view of the polymer layer as presented in Figure 4.21 (b). The residual layer was observed in the buffer layer as shown in Figure 4.21 (c). The magnified area illustrates the indentation fabricated on the buffer layer and the residual layer can be observed by the machining traces from the bottom of the pin.

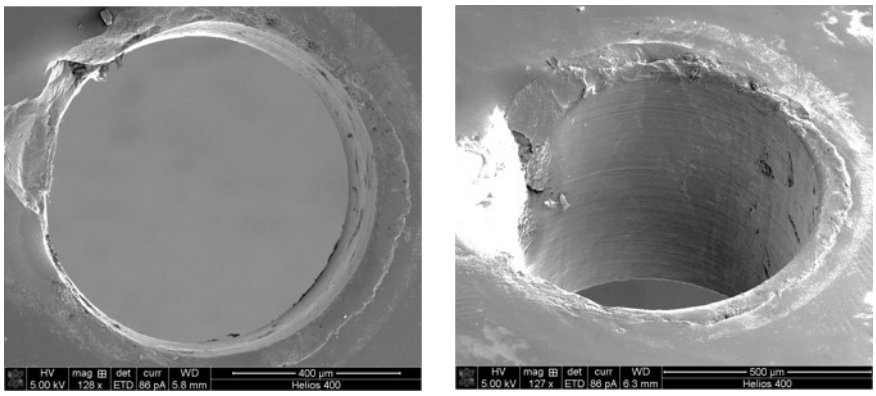

(a)

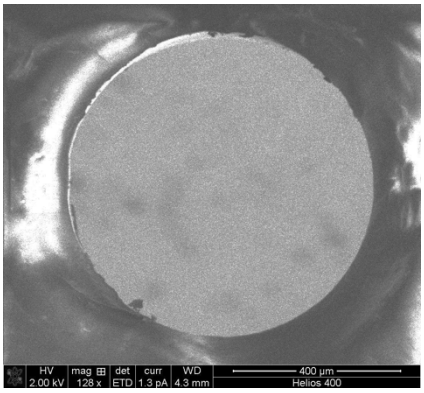

(b)

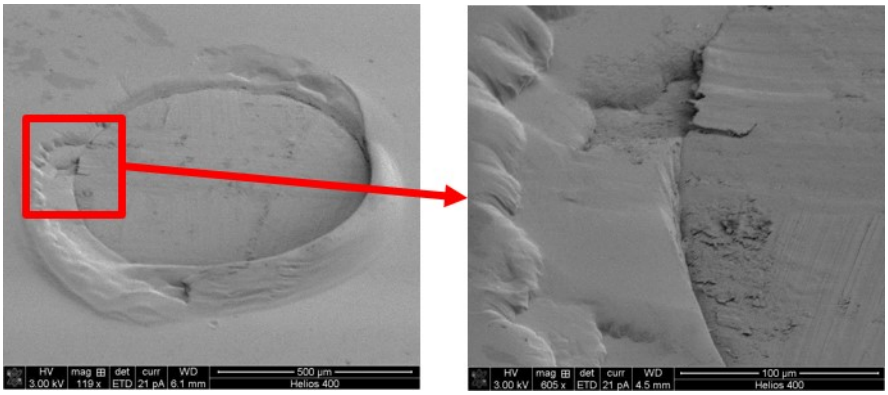

(c)

Figure 4.21. SEM images of the fabricated through-holes at a molding temperature of 125°C, an embossing force of 50 kN, and a thickness of the polymer of 0.8 mm. (a) Top view; (b) bottom view; and (c) buffer layer.

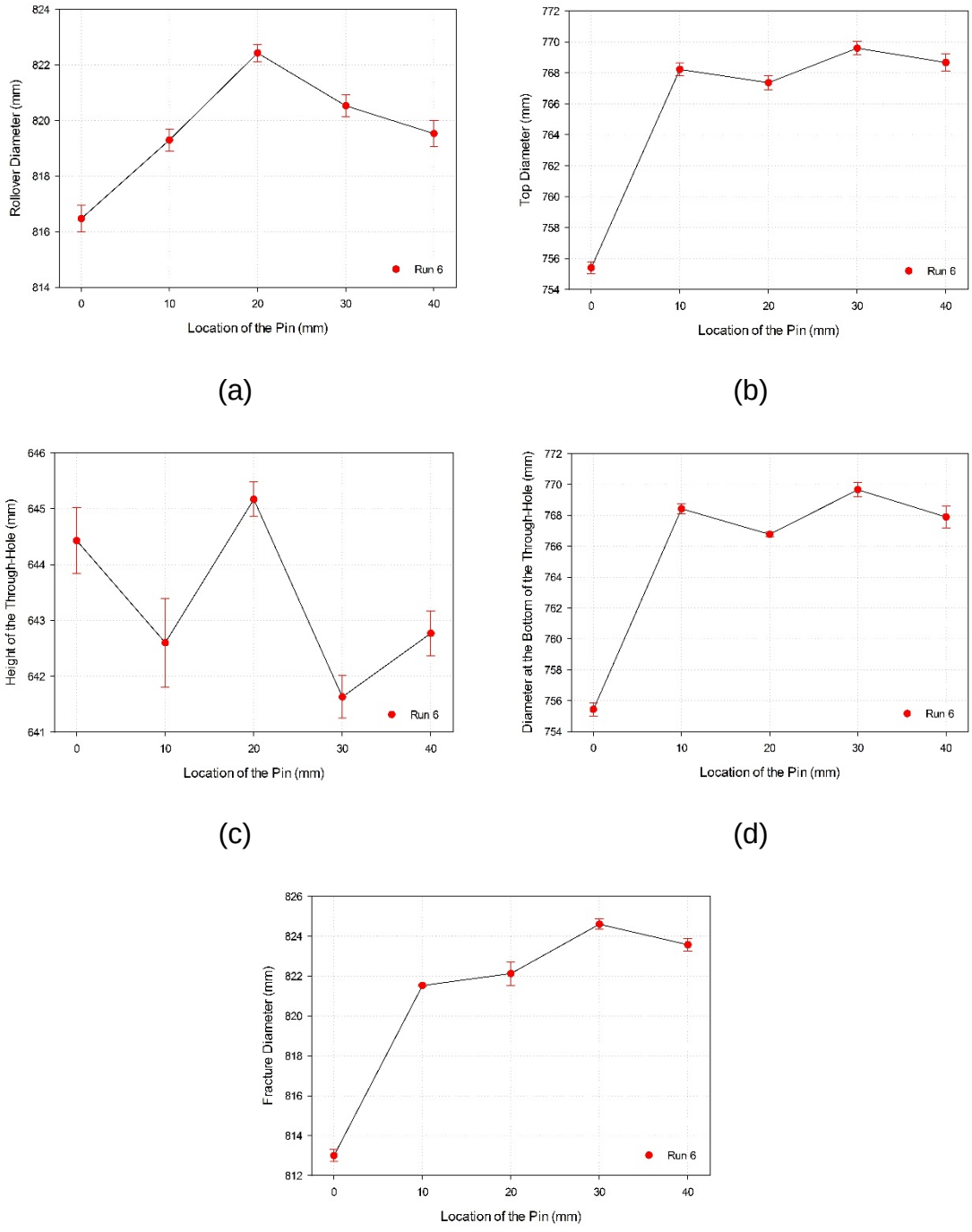

Figure 4.22. Means and confidence intervals of the measurement parameters relative to the location of the pin at a molding temperature of 125°C, an embossing force of 50 kN, and a polymer thickness of 0.8 mm. (a) Rollover diameter, (b) Top diameter, (c) Through-hole height, and (d) Bottom diameter.

The measurement parameters for the fabricated through-holes shown in Figure 4.20 are presented in Figure 4.21. The rollover diameter at the center of the mold was the lowest with a mean diameter of 816.47 ± 0.49 μm as shown in Figure 4.19 (a). The reduced rollover diameter could be related to the thermal contraction towards the center of the mold as shown in Figure 4.19. There was no significant relation observed between the rollover diameter and the radial location of the pin.

The location of the pin had no observable effect on the rollover diameter, the height of the through-hole, and the dimeter of fracture as shown in Figures 4.21 (a), (c), and (e).

The failure of the pin at a molding temperature of 125°C, an embossing force of 30 kN, and a thickness of polymer of 3.0 mm is shown in Figure 4.23. There were two types of failure including fracture and deformation. Figure 4.23 (a) shows that the pin separated at the base of the mold after fracture. Fracture was caused by the length of the pin and the elevated embossing force. Figure 4.23 (b) shows the deformation of the pin due to inability to completely penetrate into the polymer.

When the pin contacted the polymer the increased embossing force caused the pin to bend. The bent pin generated contact between the sidewalls of the pin and the top surface of the polymer. The contact generated by the pin produced elongated indentations with a depth relative to the diameter of the pin. The vertical displacement of the platen during demolding caused the pin to slightly bend back. The fatigue on the pin increased after the initial deformation, causing fracture after demolding.

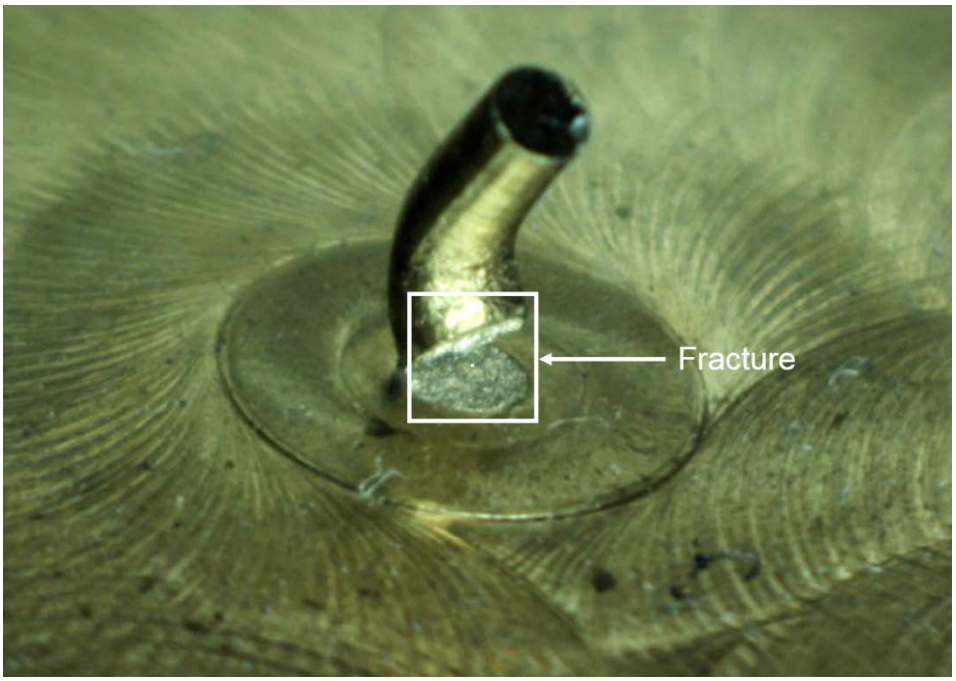

(a)

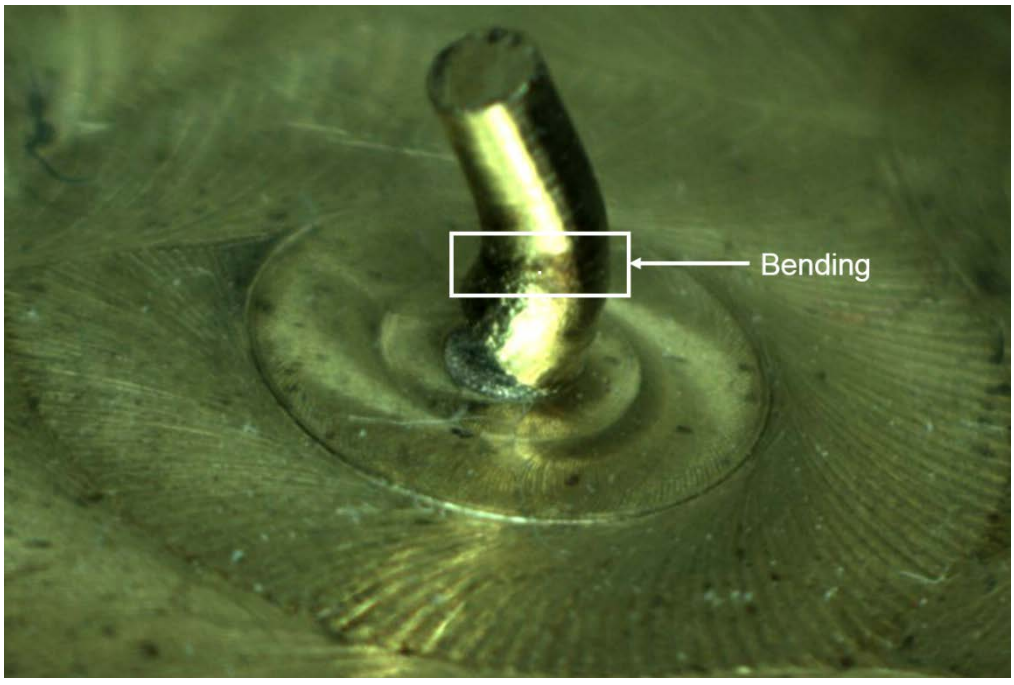

(b)

Figure 4.23. Stereoscopic images indicating failure of the pin at a molding temperature of 125°C, an embossing force of 30 kN, and a polymer thickness of 3.0 mm. (a) Fracture and (b) bending.

Top View Bottom View Buffer Layer

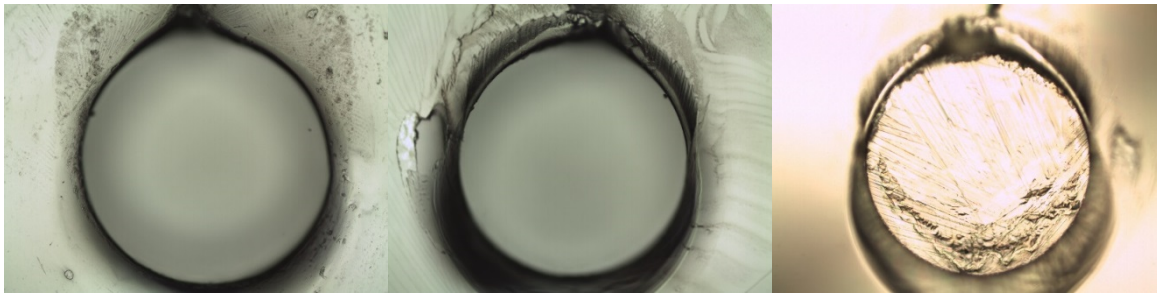

(a)

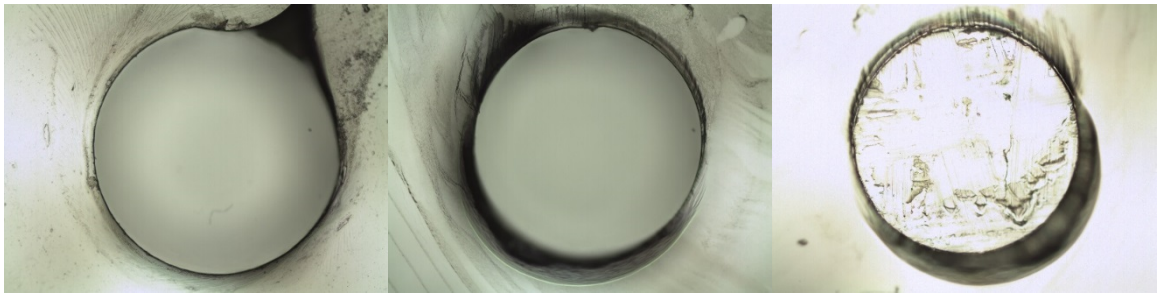

(b)

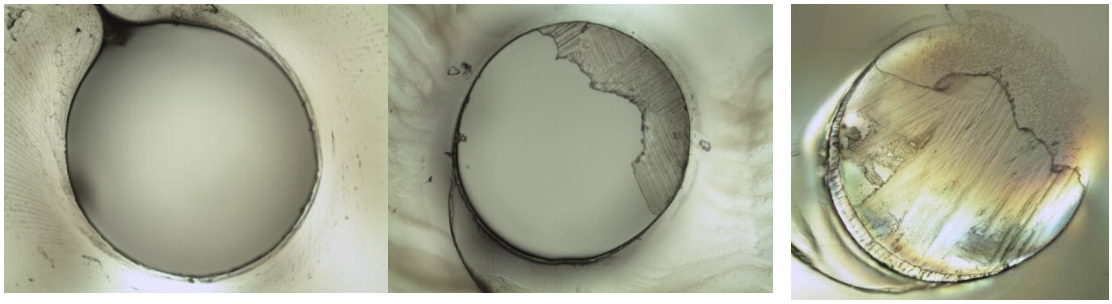

(c)

Figure 4.24. Measurescope images of the fabricated through-hole including top view, bottom view, and buffer layer; when the molding temperature was 150°C, the embossing force was 30 kN, and the thickness of the polymer was 0.8 mm; at radial locations of (a) 0, (b) 20, and (c) 40 mm.

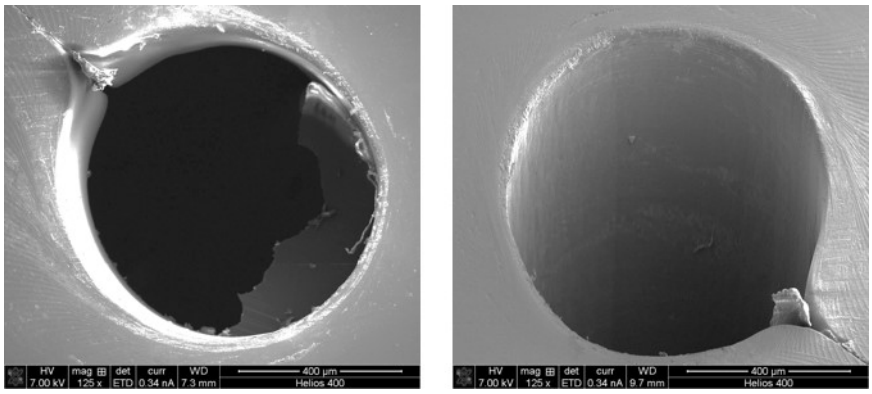

(a)

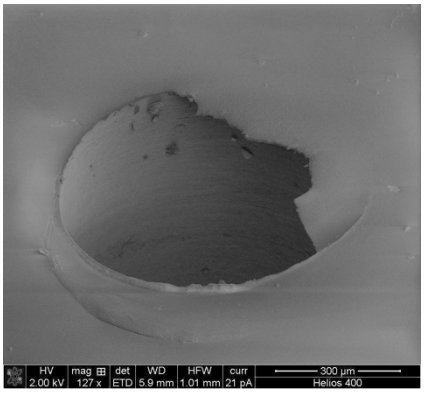

(b)

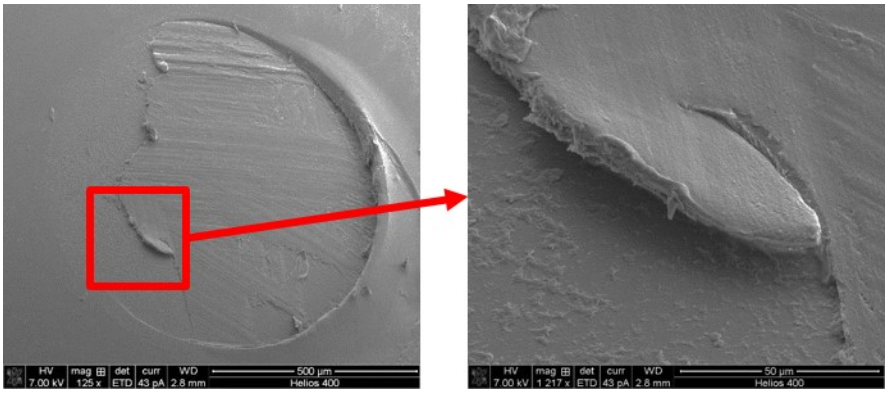

(c)

Figure 4.25. SEM images of the fabricated through-holes at a molding temperature of 150°C, an embossing force of 30 kN, and a thickness of the polymer of 0.8 mm. (a) Top view; (b) bottom view; and (c) buffer layer.

Figure 4.24 shows the results of experiments at a molding temperature of 150°C, an embossing force of 30 kN, and a thickness of polymer of 0.8 mm. The increase in the molding temperature generated round and clear through-holes. However, a slight elongation on the top sidewall of the through-hole was observed at all radial locations as shown by the top view in Figures 4.24 (a), (b), and (c). The elongation of the sidewall could be caused by the vertical displacement of the pin during demolding. Partial through-hole was observed at a radial location of 40 mm as shown in Figure 4.24 (c). A portion residual layer was observed in both the buffer and the bottom of the through-hole. The residual layer was identified in Figures 4.24 (a) and (b) by the machining traces on the indentation in the buffer.

SEM images of the fabricated through-holes at a molding temperature of 150°C, an embossing force of 30 kN, and a polymer thickness of 0.8 mm are shown in Figure 4.25. Sidewall damage was observed on the top view of the fabricated through-hole as shown in Figure 4.25 (a). A portion of the residual layer was observed at the bottom of the through hole as shown in Figures 4.25 (a) and (b).

The bottom view of the polymer layer illustrates the portion of the residual layer that remained attached to the polymer layer. The incomplete separation of the residual layer was caused by the early fracture at the point of high stress. Flatness of the substrate plate could also cause the incomplete separation of the residual layer by the non-uniform distribution of the embossing force.

The complementary portion of the residual layer is shown in Figure 4.25 (c). The magnified area illustrates a gap between the residual and the buffer layer. The area that remained in the polymer does not show machining traces.

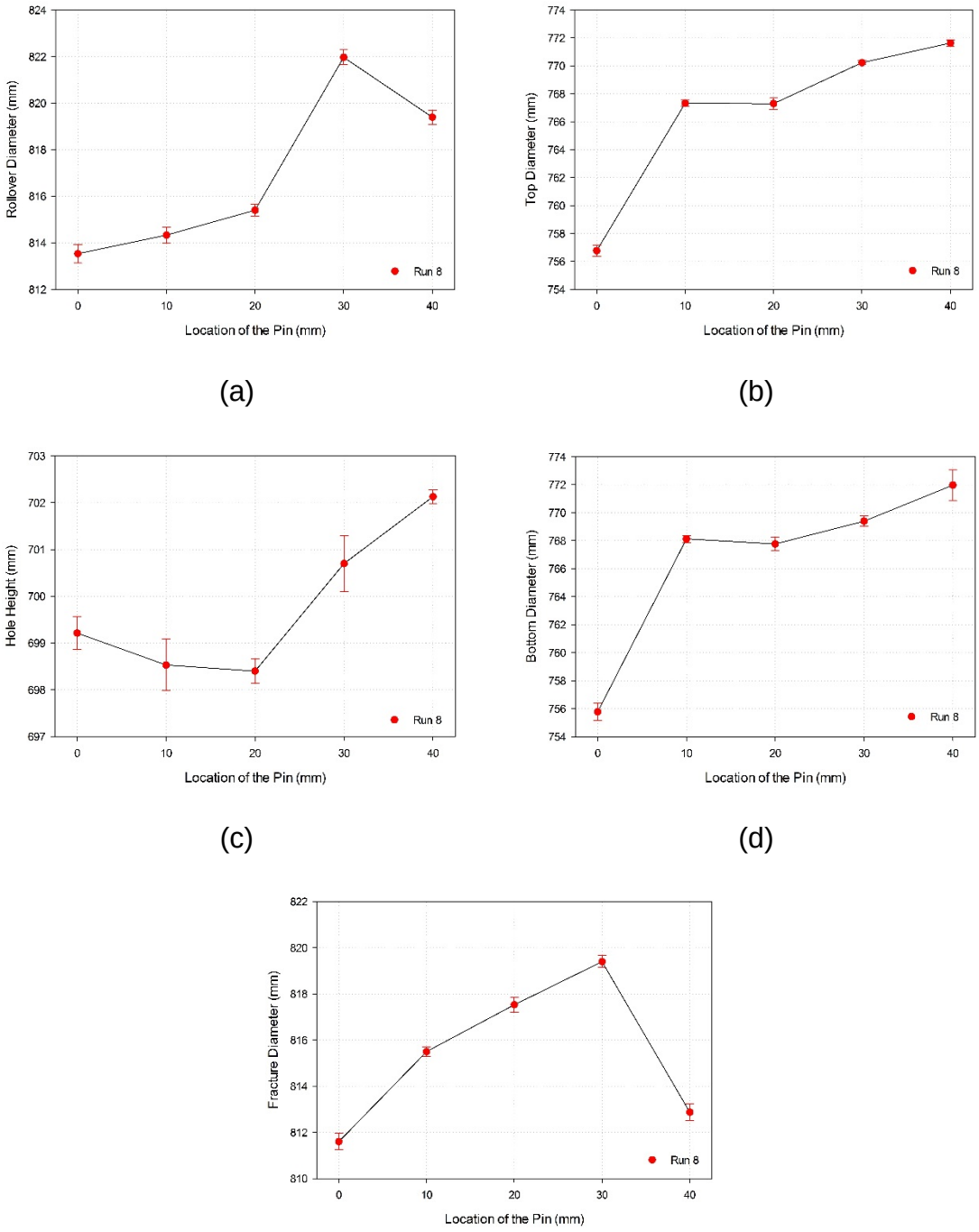

Figure 4.26. Means and confidence intervals of the measurement parameters relative to the location of the pin at a molding temperature of 150°C, an embossing force of 30 kN, and a polymer thickness of 0.8 mm. (a) Rollover diameter, (b) Top diameter, (c) Through-hole height, and (d) Bottom diameter.

Figure 4.26 illustrate the results of the measurement parameters when the molding temperature was 150°C, the embossing force was 30 kN, and the thickness of the polymer was 0.8 mm. There was no significant relation observed when compared with the results of the measurement parameters at molding temperatures of 100 and 125°C.

The radial location of the pin did not significantly affect the separation of the residual layer to fabricate through-holes. Variations in the height of the through-hole were present in all the combinations of process parameters used in the experiments of hot embossing. The non-uniformity of height was not observed in the results of the simulations. This could have been caused by the variation in flatness from the mold and the aluminum platens that were not considered in the numerical analysis.

4.6. Summary

In this chapter, through-holes were fabricated by micro hot embossing on a PMMA substrate. A brass mold was designed with nine pins at five different radial locations. A PSU buffer layer was used to reduce damage on the pin during embossing.

Complete through-holes were observed at molding temperatures of 125 and 150°C, embossing forces of 10, 30, and 50 kN, and in polymers with a thickness of 0.8, 1.5, and 3.0 mm. Temperatures below T_g were not suitable to fabricate complete through-holes as observed in the results of the simulations and the results of experiments.

The low molding temperature increased the flow resistance of the polymer, generating higher stress concentration on the pin that could lead to failure. Results of hot embossing showed that the pins were able to produce clean and round through-holes. The fabricated through-holes could be used in microfluidic applications due to the reduced burr and fracture diameters when compared to mechanical punching systems.

5. EVALUATION OF PROCESS PARAMETERS

5.1. Introduction

Statistical methods were used to analyze the fabrication of through-holes for microfluidic devices in hot embossing. The Taguchi methodology was used to study the variation in the measurement parameters. Signal-to-noise ratios (S/N ratios) are used in the Taguchi method to determine the relationship between the process parameters organized in an orthogonal array. The orthogonal array configuration identifies the critical parameters while reducing the number of experimental runs required.

In this chapter, the measurement parameters including rollover diameter, top diameter, through-hole height, bottom diameter, and fracture diameter were selected for the analysis. The results of the statistical analysis were used to determine the effect of the factors and levels in the measurement parameters. The calculated main effect indicated the process parameter combination required for the reliable fabrication of through-holes.

5.2. The Taguchi method

The Taguchi method was based on an orthogonal array designed to reduce the variation in a process. As process stability is a critical aspect, the objective of the Taguchi method is to identify the functional relationship between the factors, their levels, and the dependent variables. The Taguchi methodology offers the advantage of reducing the number of experiments compared to a full factorial design by testing combinations (Roy, 2010). The Taguchi method evaluates the process parameters in combination with each other. This facilitates the collection

of data to identify the required process parameters for the reliable replication of through-holes while efficiently managing time and resources.

The Taguchi method evaluates the response of the variables relative to the target value at different noise conditions. S/N ratios are used to measure the response dependent on the desired outcome. The most used S/N ratios include “smaller is better”, “larger is better”, and “nominal is best”. The “smaller is better” S/N ratio minimize the response of the dependent variable while “larger is better” maximizes the response. “Nominal is best” is used to correlate the response to the mean and standard deviation (Taguchi et al., 1993).

The L_9 array, with the fourth parameter omitted, was used to study nine sets of experimental runs with three factors at three levels. The orthogonality of the Taguchi design defines that any in level of a factor, the number of occurrences of any level of any other factor are equal. Table 5.1 presents the process parameters and levels used for the experiments. Three factors including molding temperature, embossing force, and the thickness of the polymer with levels of 100, 125, and 150°C; 10, 30, and 50 kN; and 0.8, 1.5, and 3.0 mm, respectively.

Table 5.1. Process parameters for the fabrication of through-holes in micro hot embossing.

	Process Parameter	Level 1	Level 2	Level 3
A	Molding Temperature (°C)	100	125	150
B	Embossing Force (kN)	10	30	50
C	Thickness of Polymer (mm)	0.8	1.5	3.0

The “nominal is best” configuration was selected for the evaluation of the process parameters in the fabrication of through-holes. The selected S/N ratio identifies the appropriate parameter combination to reduce variability around the target. The orthogonal array was used to analytically evaluate the combinations of process parameters over all the noise factors combinations using the mean response and standard deviation calculated by Equation 5.1 and Equation 5.2, respectively.

$$\bar{y} = \frac{1}{n}\sum_{i=1}^{n} y_i \tag{5.1}$$

where n is the number of experiments and y is the measurement parameter.

$$s = \sqrt{\frac{1}{n-1}\sum_{i=1}^{n}(y_i - \bar{y})^2} \tag{5.2}$$

where $\bar{y}$ is the mean response, n is the number of experiments, and y is the measurement parameter.

Table 5.2. Estimated mean and standard deviation of the rollover diameter on the fabricated through-holes.

				Rollover Diameter (μm)									
Run	**A**	**B**	**C**	**0 mm**		**10 mm**		**20 mm**		**30 mm**		**40 mm**	
				$\bar{x}$	**s**	$\bar{x}$	**s**	$\bar{x}$	**s**	$\bar{x}$	**s**	$\bar{x}$	**s**
1	L1	L1	L1	826.57	0.97	827.07	3.09	837.20	0.35	829.97	0.71	829.60	0.36
2	L1	L2	L2	852.10	0.26	845.03	1.93	851.93	0.25	860.90	0.75	852.13	0.55
4	L2	L1	L2	816.37	0.84	825.00	0.46	821.30	0.36	826.30	0.95	832.90	0.62
6	L2	L3	L1	816.47	0.49	819.30	0.40	822.43	0.31	820.53	0.40	819.53	0.47
7	L3	L1	L3	868.50	0.36	869.53	0.29	861.53	0.38	870.47	0.40	872.23	0.42
8	L3	L2	L1	813.53	0.40	814.33	0.32	815.40	0.26	821.97	0.31	823.40	0.30
9	L3	L3	L2	815.53	0.49	819.37	0.31	820.53	0.32	821.63	0.31	829.40	0.26

The calculated mean response and standard deviation of the rollover diameter on the fabricated Through-holes is shown in Table 5.2. The rollover diameter is presented depending on the radial location of the pin. The factors and levels are shown to indicate the process parameter combination used in each run. There was no direct correlation between the rollover diameter and the radial location of the pin. Table 5.3 shows the estimated mean and standard deviation of the diameter at the top of the fabricated through-holes. Variations in standard deviation could be contributed to the accuracy of the measuring technique.

The calculated mean and standard deviation for the height of the fabricated through-hole are shown in Table 5.4. The height of the through-hole was directly correlated with the thickness of the polymer. Runs 3 and 5 were not included since there was not data obtained by the failure of the pin. Tables 5.5 and 5.6 show the estimated means and standard deviations for the diameter at the bottom of the through-hole and the fracture diameter, respectively.

Table 5.3. Estimated mean and standard deviation of the diameter at the top of the fabricated through-holes.

				Top Diameter (μm)									
Run	**A**	**B**	**C**	**0 mm**		**10 mm**		**20 mm**		**30 mm**		**40 mm**	
				$\bar{x}$	**s**	$\bar{x}$	**s**	$\bar{x}$	**s**	$\bar{x}$	**s**	$\bar{x}$	**s**
1	L1	L1	L1	751.20	0.36	767.93	0.21	768.43	0.35	768.17	0.21	768.03	0.15
2	L1	L2	L2	797.30	0.36	797.10	0.66	789.87	0.75	798.03	1.33	793.63	1.17
4	L2	L1	L2	766.63	0.78	767.12	0.40	763.53	0.35	762.50	0.36	767.77	0.55
6	L2	L3	L1	755.40	0.36	768.23	0.42	767.37	0.45	769.90	0.44	768.67	0.55
7	L3	L1	L3	742.00	0.46	752.40	0.38	756.60	0.85	754.70	0.21	754.53	0.40
8	L3	L2	L1	756.77	0.40	767.33	0.25	767.30	0.40	770.23	0.15	771.63	0.25
9	L3	L3	L2	783.40	0.26	784.30	0.20	788.53	0.35	789.43	0.42	787.37	0.31

Table 5.4. Estimated mean and standard deviation of the height on the fabricated through-holes.

Hole Height (μm)													
Run	**A**	**B**	**C**	**0 mm**		**10 mm**		**20 mm**		**30 mm**		**40 mm**	
				$\bar{x}$	**s**	$\bar{x}$	**s**	$\bar{x}$	**s**	$\bar{x}$	**s**	$\bar{x}$	**s**
1	L1	L1	L1	647.70	0.17	651.40	0.26	667.63	0.25	669.37	0.38	659.27	0.57
2	L1	L2	L2	1008.20	0.26	1008.10	0.36	1004.00	0.60	1005.70	1.12	1003.00	1.42
4	L2	L1	L2	1349.50	0.35	1350.30	0.32	1348.60	0.20	1347.40	0.36	1347.60	0.56
6	L2	L3	L1	644.43	0.59	642.60	0.79	645.17	0.31	641.63	0.38	642.77	0.40
7	L3	L1	L3	2516.07	0.21	2512.53	0.40	2510.67	0.49	2512.63	0.31	2513.37	0.31
8	L3	L2	L1	699.23	0.35	698.53	0.55	698.40	0.26	700.70	0.60	702.13	0.15
9	L3	L3	L2	987.40	0.30	980.07	0.47	981.40	0.26	985.43	0.23	989.37	0.31

Table 5.5. Estimated mean and standard deviation of the diameter at the bottom of the fabricated through-holes.

Bottom Diameter (μm)													
Run	**A**	**B**	**C**	**0 mm**		**10 mm**		**20 mm**		**30 mm**		**40 mm**	
				$\bar{x}$	**s**	$\bar{x}$	**s**	$\bar{x}$	**s**	$\bar{x}$	**s**	$\bar{x}$	**s**
1	L1	L1	L1	746.37	0.32	755.47	0.65	760.10	0.10	771.17	0.25	770.77	0.40
2	L1	L2	L2	797.67	0.25	797.47	0.32	794.47	2.35	798.63	0.25	791.70	0.56
4	L2	L1	L2	766.13	0.31	766.23	0.36	764.20	0.30	763.03	0.50	767.20	1.12
6	L2	L3	L1	755.43	0.45	768.43	0.32	767.77	0.15	767.67	0.45	767.90	0.70
7	L3	L1	L3	755.30	0.46	761.47	0.38	762.00	0.85	763.47	0.21	764.37	0.40
8	L3	L2	L1	755.77	0.61	768.13	0.25	767.77	0.50	769.40	0.36	771.97	2.60
9	L3	L3	L2	783.59	0.25	784.47	0.40	785.57	0.31	786.53	0.40	786.63	0.31

Table 5.6. Estimated mean and standard deviation of the diameter of fracture on the fabricated through-holes.

Fracture Diameter (μm)													
Run	**A**	**B**	**C**	**0 mm**		**10 mm**		**20 mm**		**30 mm**		**40 mm**	
				$\bar{x}$	**s**	$\bar{x}$	**s**	$\bar{x}$	**s**	$\bar{x}$	**s**	$\bar{x}$	**s**
4	L2	L1	L2	823.07	0.40	825.60	1.05	822.33	0.60	822.40	1.25	822.13	0.25
6	L2	L3	L1	813.00	0.30	821.53	0.40	822.13	0.59	824.60	0.26	823.57	0.31
7	L3	L1	L3	831.93	0.15	842.50	0.20	842.53	0.35	842.60	0.10	841.97	0.31
8	L3	L2	L1	811.60	0.36	815.50	0.20	817.53	0.32	819.40	0.26	812.87	0.35
9	L3	L3	L2	823.67	0.25	825.57	0.42	827.53	0.40	829.47	0.32	829.40	0.26

Table 5.7. S/N ratio and main effect for the measured rollover diameter.

	0 mm				40 mm			
Factor	**Level 1**	**Level 2**	**Level 3**	**Main Effect**	**Level 1**	**Level 2**	**Level 3**	**Main Effect**
A	-68.12	-62.00	-64.37	6.12	-65.51	-63.64	-68.37	2.86
B	-64.76	-63.02	-67.64	4.62	-66.28	-65.39	-67.35	1.96
C	-64.38	-62.07	-66.03	3.96	-66.93	-65.41	-66.42	1.52

The main effects were calculated from the S/N ratios obtained from the estimated means and standard deviations. The difference between the maximum and minimum S/N ratio for each factor determined the main effect. The main effect establishes which parameter had the most significant effect on the stability of the process.

Table 5.7 shows the S/N ratio and main effect for the rollover diameter at radial locations of 0 and 40 mm. The results of the main effect indicate that the molding temperature had a significant effect on the reliability of the rollover diameter. This means that the molding temperature of the polymer is a critical factor to reduce variation on the flow of the polymer in hot embossing.

The main effect plots of the S/N ratio for the rollover diameter at radial locations of 0 and 40 mm are shown in Figure 5.1. The graphical representation of the S/N ratio indicates the appropriate process parameters to reduce rollover diameter variation. A molding temperature of 125°C, an embossing force of 30 kN, and a polymer thickness of 1.5 mm could increase the stability in regard to the rollover diameter as shown in Figures 5.1 (a) and (b).

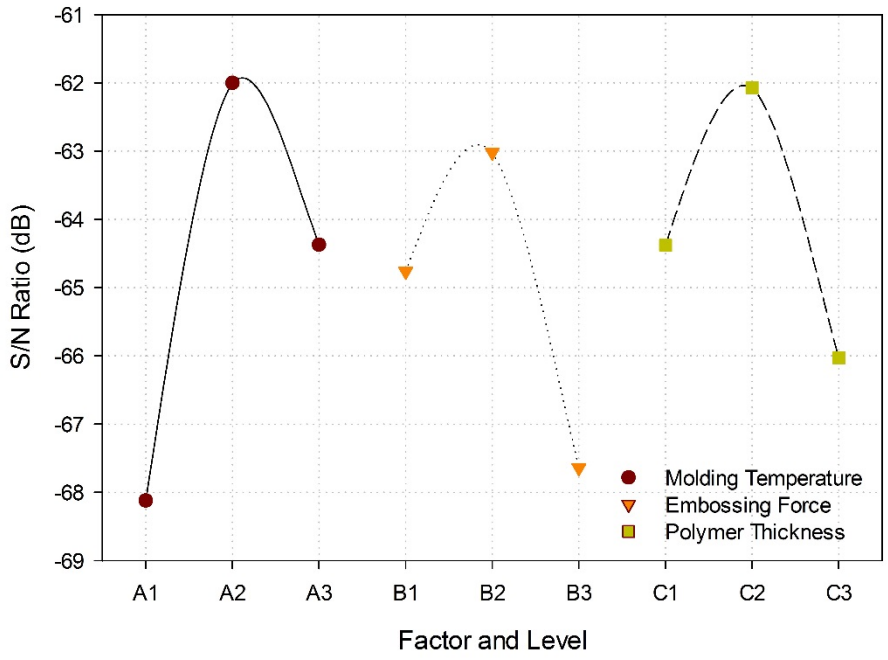

(a)

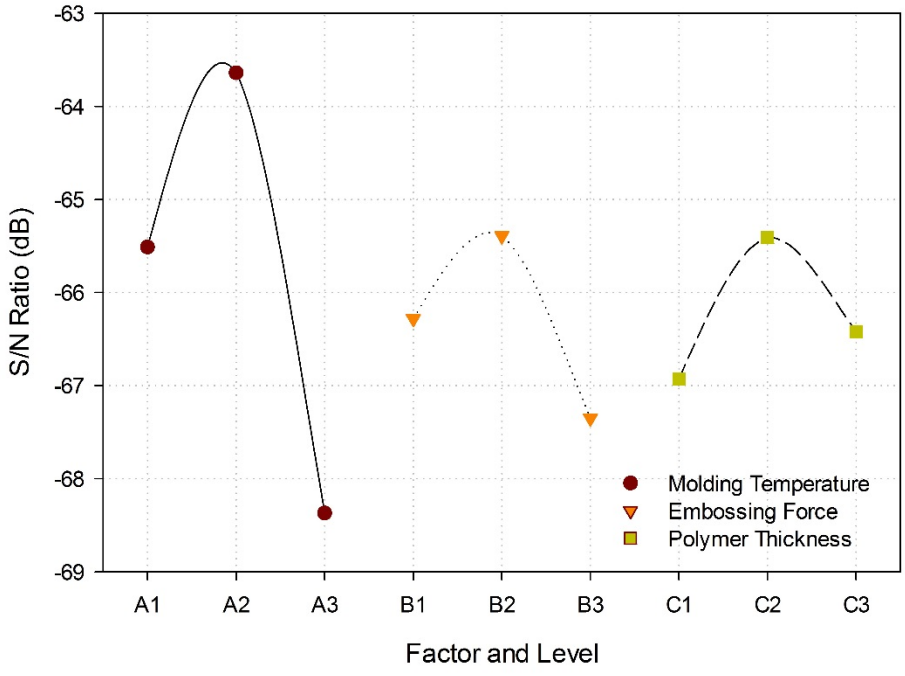

(b)

Figure 5.1. The main effect plot of the S/N ratios for the rollover diameter of the fabricated through-holes; at radial locations of: (a) 0 and (b) 40 mm.

Table 5.8. S/N ratio and main effect for the measured diameter at the top of the through-hole.

	0 mm				40 mm			
Factor	**Level 1**	**Level 2**	**Level 3**	**Main Effect**	**Level 1**	**Level 2**	**Level 3**	**Main Effect**
A	-66.65	-62.04	-66.42	4.61	-65.41	-62.90	-67.80	4.90
B	-63.46	-66.22	-68.01	4.54	-67.53	-63.21	-65.50	4.32
C	-66.12	-65.45	-64.15	1.97	-65.51	-62.54	-65.51	2.97

Table 5.8 shows the calculated S/N ratios and main effects for the measured diameter at the top of the fabricated through-hole. The results of the calculation identified the molding temperature as the main effect for the stability in the measured diameter, at the top of the through-hole. Followed by the embossing force and the thickness of the polymer.

A molding temperature of 125°C, an embossing force of 30 kN, and a polymer thickness of 3.0 mm were identified as the optimal process parameters for the diameter at the top of the fabricated through-hole as shown in Figure 5.2 (a). The reduced variation in the polymer with a thickness of 3.0 mm was caused by the failure of the pins at molding temperatures of 100 and 125°C. As a result, there was only one data point for the thickness of the polymer selected. This limitation constrained the effects of the thickness of the polymer in relation to the diameter at the top of the fabricated through-hole.

Figure 5.2 (b) illustrates an optimal process parameter combination of A2, B2, and C2 for the diameter at the top of the through-hole at a radial location of 40 mm. These results correlated with the combination of parameters for the rollover diameter. However, the reduced data obtained from the polymer with a thickness of 3.0 mm could affect the reliability of the obtained results.

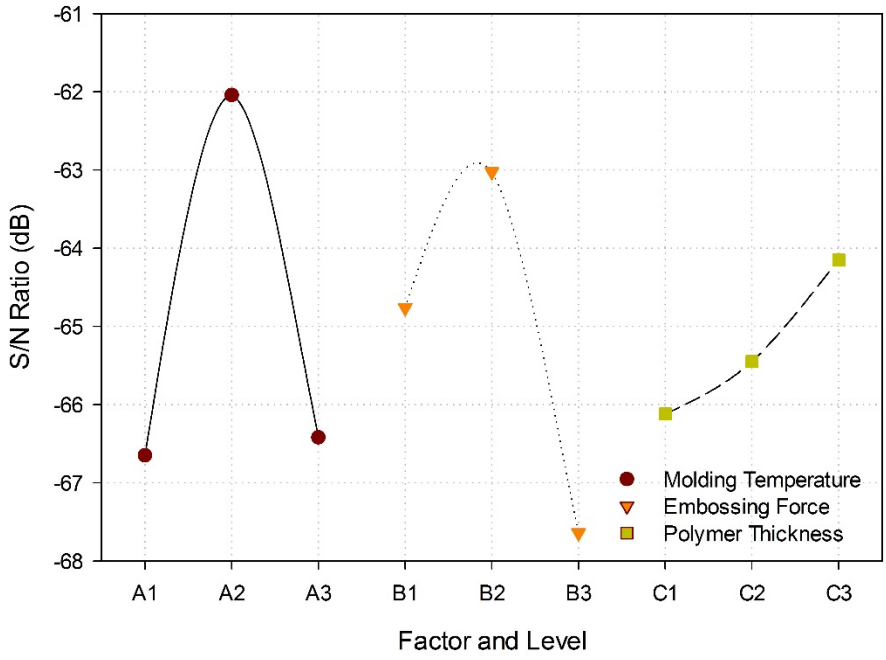

(a)

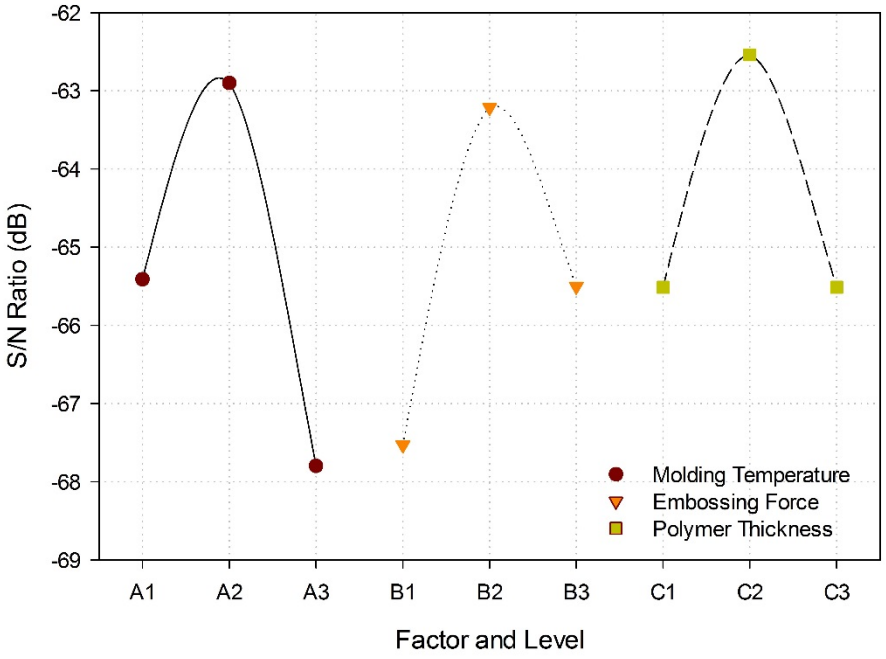

(b)

Figure 5.2. The main effect plot of the S/N ratios for the diameter at the top of the fabricated through-holes; at radial locations of: (a) 0 and (b) 40 mm.

Table 5.9. S/N ratio and main effect for the measured height of the through-hole.

	0 mm				40 mm			
Factor	**Level 1**	**Level 2**	**Level 3**	**Main Effect**	**Level 1**	**Level 2**	**Level 3**	**Main Effect**
A	-71.69	-66.24	-72.64	6.40	-75.79	-65.87	-59.12	16.67
B	-74.97	-68.89	-65.56	6.08	-69.02	-65.19	-67.10	3.83
C	-66.13	-71.28	-70.35	5.15	-66.26	-64.90	-73.41	8.51

The molding temperature was identified as the main effect in relation of the measured height of the through-hole as shown in Table 5.9. Molding temperatures above the glass transition reduced the fluidic resistance of the polymer, allowing the pin to advance further towards the buffer layer. The higher the molding temperature the lower the measured height of the through-hole in response to the reduced polymer resistance.

A reduced variation in the height of the through-hole located at the center was observed at a polymer with a thickness of 0.8 mm as shown in Figure 5.3 (a). This can be explained by the reduced thickness of the polymer. The lower volume of the substrate combined with an elevated embossing force reduced the flow of the molten polymer resulting in a reduced parameter variation.

A molding temperature of 150°C reduced the effect of the embossing force and the thickness of the polymer on the height of the fabricated through-hole at a radial location of 40 mm as illustrated in Figure 5.3 (b). The decrease in the fluidic resistance allowed the pin to penetrate into the polymer while reducing the variation in the height of the through-hole. At this molding temperature, the effect of the embossing force and the thickness of the polymer were not significant. The optimal process parameter combination to reduce variation in a through-hole located at 40 mm were identified as A3, B2, and C2.

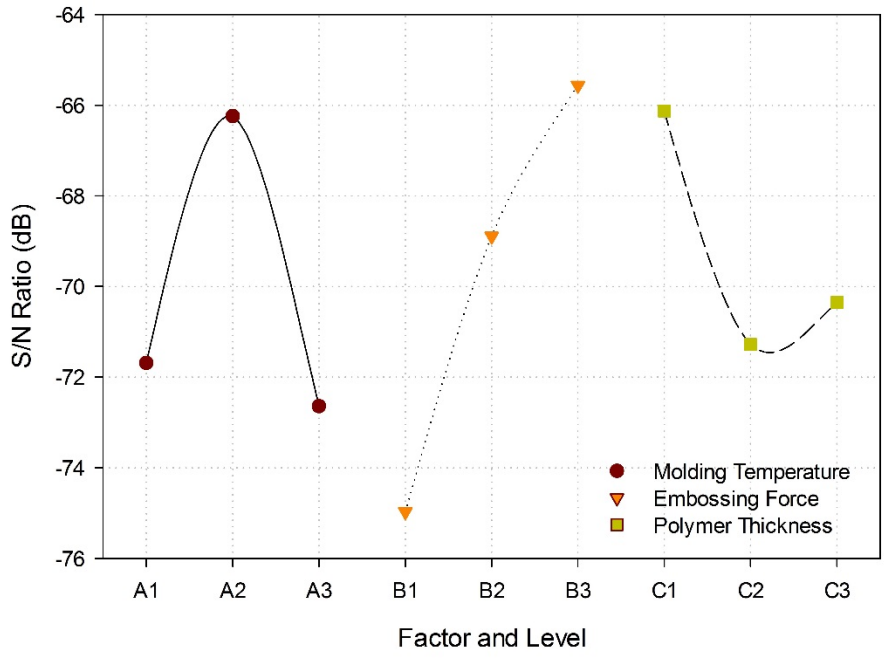

(a)

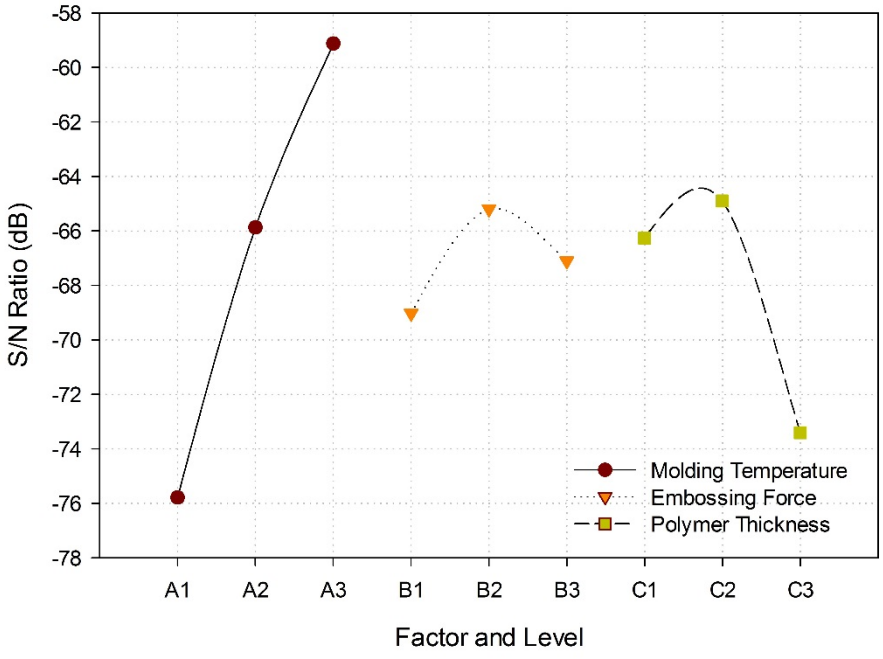

(b)

Figure 5.3. The main effect plot of the S/N ratios for the height of the fabricated through-holes; at radial locations of: (a) 0 and (b) 40 mm.

Table 5.10. S/N ratio and main effect for the measured diameter at the bottom of the through-hole.

	0 mm				40 mm			
Factor	**Level 1**	**Level 2**	**Level 3**	**Main Effect**	**Level 1**	**Level 2**	**Level 3**	**Main Effect**
A	-68.72	-66.18	-65.36	3.35	-64.35	-56.71	-61.06	7.64
B	-66.51	-65.97	-67.21	1.24	-65.55	-64.32	-64.45	1.23
C	-64.57	-65.97	-64.31	1.66	-58.65	-62.60	-65.62	6.97

The calculated main effect for the measured diameter at the bottom of the through-hole identifies the molding temperature as the critical factor for the reliable fabrication as shown in Table 5.10. This can be explained by the softening of the polymer as the molding temperature increased which led to a better replication fidelity.

Figure 5.4 shows the main effect plot of the S/N ratios for the measured diameter at the bottom of the through-hole. The optimal process parameters to achieve reduced variability in relation to the diameter at the bottom of the pin located at the center could be selected from the figures. The results of the statistical analysis agreed with the relationship observed between the top and bottom diameters in the hot embossing experiments. The results observed in Figure 5.2 (a) illustrate an appropriate thickness of the polymer of 3.0 mm. These results can be correlated with the results observed in Figure 5.4 (a). As mentioned before, the indicated thickness of the polymer could be caused by the reduced number of runs. A process parameter combination of A2, B2, and C1 are shown as the proper process parameters in Figure 5.2 (b). Results indicated that the molding temperature significantly affected the dependent variable by promoting the advance of the pin.

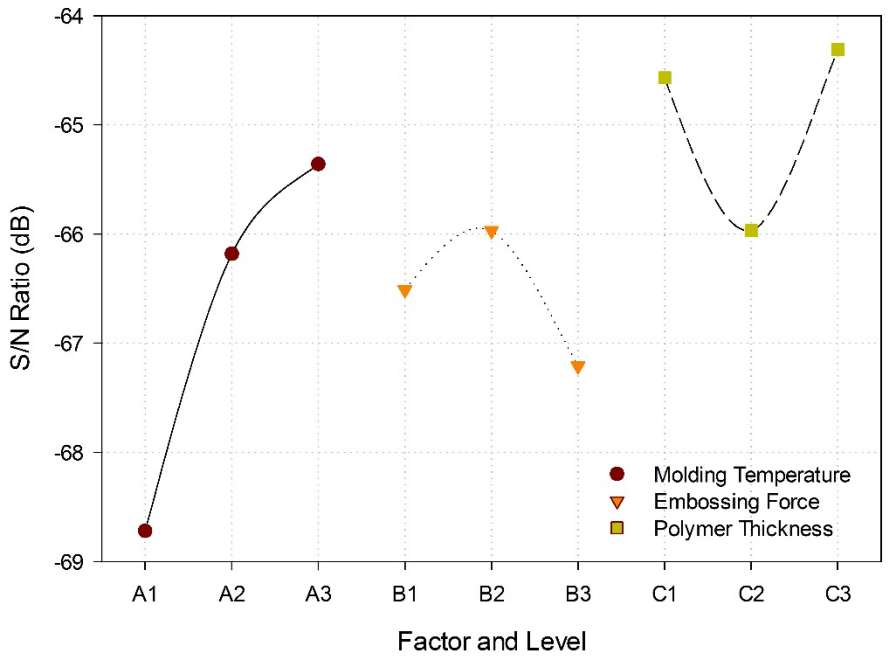

(a)

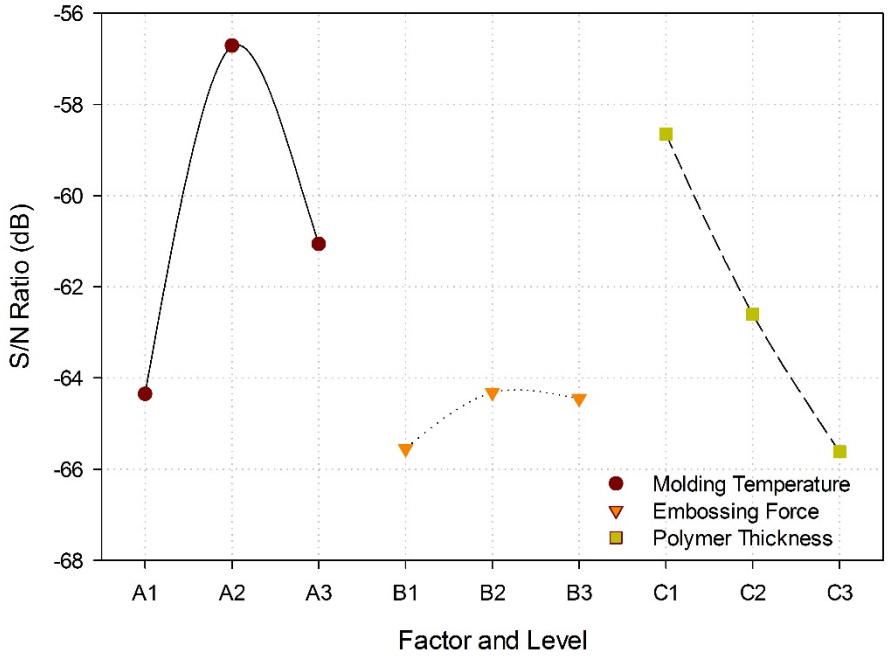

(b)

Figure 5.4. The main effect plot of the S/N ratios for the diameter at the bottom of the fabricated through-holes; at radial locations of: (a) 0 and (b) 40 mm.

Table 5.11. S/N ratio and main effect for the measured diameter of fracture for the fabricated through-hole.

	0 mm				40 mm			
Factor	**Level 1**	**Level 2**	**Level 3**	**Main Effect**	**Level 1**	**Level 2**	**Level 3**	**Main Effect**
A		-67.46	-70.77	3.30		-70.34	-67.69	2.65
B	-70.57	-67.06	-69.51	3.51	-69.51	-67.32	-69.28	2.19
C	-67.86	-68.31	-67.06	1.25	-67.90	-70.21	-70.08	2.17

Incomplete through-holes were observed at a molding temperature of 100°C. Therefore, no S/N ratio data was calculated at A1 of the measured diameter of fracture as shown in Table 5.11. The embossing force was determined as the main effect for the pin located at the center. The variation in the results could be caused by the incomplete through-holes which caused uncertainty compared to the results observed at 40 mm.

Figure 5.5 shows a combination of process parameters. However, the proper parameter combination could not be identified. The fabrication of incomplete through-holes as well as the reduced number of runs with a polymer with a thickness of 3.0 mm increased the uncertainty of the calculated results. Figures 5.5 (a) and (b) could not be used to reduce the variability in the diameter of fracture in the fabricated through-holes.

The molding temperature was identified as the main effect to reduce the variability in the investigated measurement parameters. For the majority of cases, a molding temperature of 125°C was identified as the most significant parameter. Molding temperatures of 100°C reduced the advance of the pin generating incomplete through-holes and failure of the pin, while higher temperature increased the variability of the dependent variables.

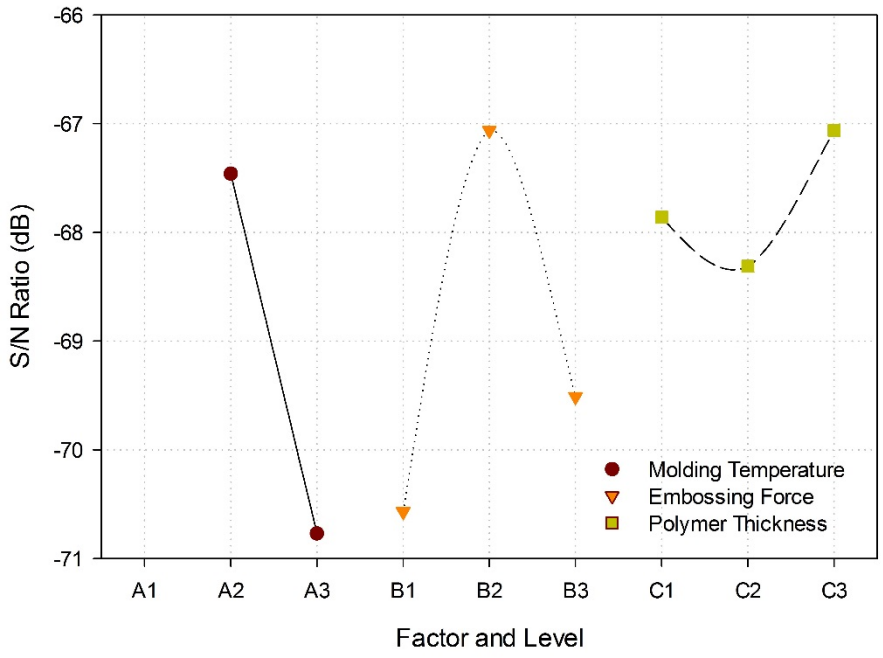

(a)

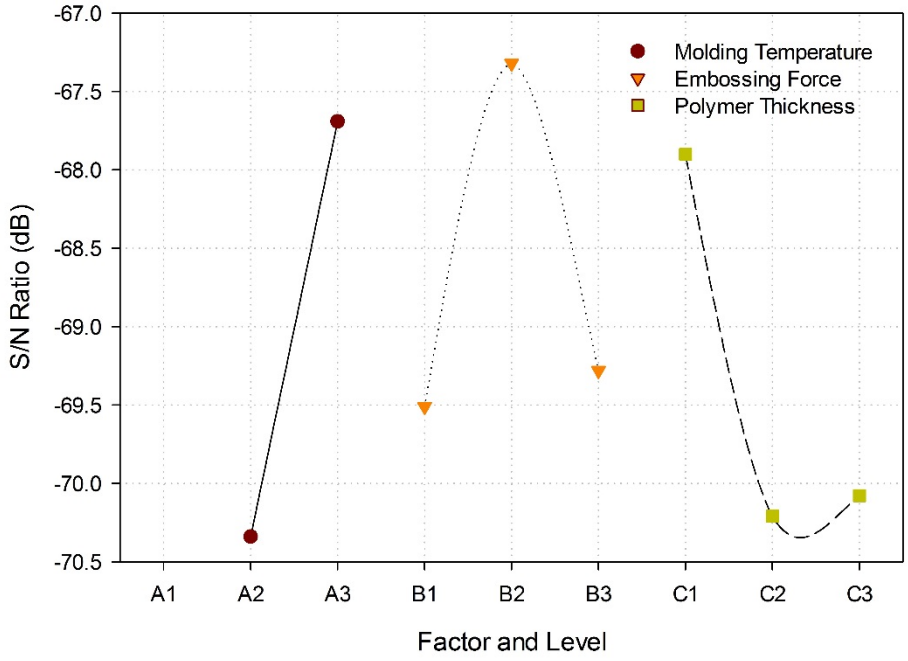

(b)

Figure 5.5. The main effect plot of the S/N ratios for the fracture diameter of the fabricated through-holes; at radial locations of: (a) 0 and (b) 40 mm.

For a through-hole to function correctly, as a microfluidic interconnect, certain dimensional tolerances have to be met. These requirements include alignment and dead volume. Alignment could be improved using auxiliary structures to prevent deformations in the through-hole (Bhagat et al., 2007). The use of auxiliary structures could reduce the effects from stress and shrinkage on the pin during embossing. The dead volume is a section of the internal volume that is out of the flow path causing areas of stagnation within the flow (Johnson et al., 2010). Higher rollover, top, and bottom diameters could significantly affect the flow path inside the through-hole by increasing the dead volume.

A molding temperature of 125°C and an embossing force of 30 kN were the process parameters that showed reduced variation on the rollover, top, and bottom diameters. The identified process parameters could lead to the reliable fabrication of through-holes by reducing the dead volume zones. The results of the S/N ratios in relation to the thickness of the polymer were inconsistent. There was uncertainty on the effect of the polymer thickness on the replication fidelity.

5.3. Interaction between factors and prediction models

Interaction between factors were used to study the effect of the independent variables over the response. Interactions were calculated by analysis of variance using a confidence level of 95%. A fitted regression model using Minitab (Minitab Inc., State College, PA) was developed to predict the measurement parameters depending on the factors selected. Based on the results of the Taguchi design, the effect of the thickness of the polymer was not considered. A two-way full factorial ANOVA design determined the interaction effect of each measurement parameter.

5.3.1. Rollover diameter

Table 5.12. Analysis of variance for the rollover diameter of a through-hole located at the center.

Source	DF	Adj SS	Adj MS	F-Value	P-Value
Molding temperature	2	3734.3	1867.16	6293.81	0.001
Embossing force	2	637.6	318.78	1074.54	0.001
Interaction	4	6532.2	1633.04	5504.63	0.001
Error	18	5.3	0.30		
Total	26	10909.4			

Table 5.13. Analysis of variance for the rollover diameter of a through-hole located at 40 mm from the center.

Source	DF	Adj SS	Adj MS	F-Value	P-Value
Molding temperature	2	2064.25	1032.12	5238.22	0.001
Embossing force	2	845.98	422.99	2146.75	0.001
Interaction	4	4730.18	1182.55	6001.64	0.001
Error	18	3.55	0.20		
Total	26	7643.95			

The results of the analysis of variance for the rollover diameter at radial locations of 0 and 40 mm are shown in Tables 5.12 and 5.13, respectively. Experimental results showed that the molding temperature and the embossing force affected the dependent variable, rollover diameter. Using a 95% confidence interval ($p > 0.05$), the molding temperature caused grater effect on the measurement parameter.

The interaction effect between factors indicated that there was an effect on the advance of the polymer caused by these factors acting together. The regression equation to predict the rollover diameter at radial locations of 0 and 40 mm from the center are presented in Equations 5.3 and 5.4, respectively.

$$D_{r\,@0mm} = 717.7 + 0.956(Molding\ Temperature) + 4.68(Embossing\ Force) - 0.03925(molding\ Temperature * Embossing\ Force) \quad (5.3)$$

$$D_{r\,@40mm} = 730.2 + 0.922(Molding\ Temperature) + 3.805(Embossing\ Force) - 0.03268(molding\ Temperature * Embossing\ Force) \quad (5.4)$$

5.3.2. Top diameter

Table 5.14. Analysis of variance for the top diameter of a through-hole located at the center of the polymer layer.

Source	DF	Adj SS	Adj MS	F-Value	P-Value
Molding Temperature	2	5985.99	2993.00	16941.49	0.001
Embossing Force	2	2108.41	1054.21	5967.21	0.001
Interaction	4	1309.29	327.32	1852.78	0.001
Error	18	3.18	0.18		
Total	26	9406.88			

Table 5.15. Analysis of variance for the top diameter of a through-hole located at 40 mm.

Source	DF	Adj SS	Adj MS	F-Value	P-Value
Molding Temperature	2	2273.04	1136.52	2722.80	0.001
Embossing Force	2	2086.81	1043.40	2499.72	0.001
Interaction	4	977.75	244.44	585.61	0.001
Error	18	7.51	0.42		
Total	26	5345.11			

The results of the statistical analysis for the top diameter are presented in Tables 5.14 and 5.15. Results agreed with the Taguchi design by indicating the molding temperature as the main factor for the fabrication of through-holes. The interaction effect between the molding temperature and the embossing force was verified by the results of the analysis of variance. The regression models are presented in Equations 5.5 and 5.6.

$$D_{t\,@0mm} = 778.7 + 0.274(Molding\ Temperature) + 1.129(Embossing\ Force) - 0.00235(molding\ Temperature * Embossing\ Force) \quad (5.5)$$

$$D_{r\,@40mm} = 730.2 + 0.922(Molding\ Temperature) + 3.805(Embossing\ Force) - 0.03268(molding\ Temperature * Embossing\ Force) \quad (5.6)$$

5.3.3. Through-hole height

The height of the through-hole directly depended on the thickness of the polymer layer. Therefore, a Taguchi design determined the ranking of the factors. Results indicated that both the molding temperature and the embossing force could be rejected as shown in Table 5.16.

Table 5.16. Response table for S/N Ratios of the Through-hole height.

Level	Molding Temperature	Embossing Force	Polymer Thickness
1	20.326	12.217	22.512
2	12.116	16.241	17.043
3	16.393	20.378	9.279
Delta	8.210	8.161	13.233
Rank	**2**	**3**	**1**

The regression model was determined with a single-factor analysis of variance based on the results obtained from the Taguchi design. A regression model was used to determine the prediction equation. The regression equations for the estimation of the height of the through-hole at radial locations of 0 and 40 mm are presented in Equations 5.7 and 5.8, respectively.

$$H_{h\,@0mm} = 176 + 617.5(Polymer\ Thickness) \tag{5.7}$$

$$H_{h\,@40mm} = 183 + 614.3(Polymer\ Thickness) \tag{5.8}$$

5.3.4. Bottom diameter

As observed on the Taguchi design and the previous measurement parameters, the molding temperature did have a significant effect on the fabrication

of through-holes. Tables 5.17 and 5.18 illustrate the results of the analysis of variance for through-holes located at radial locations of 0 and 40 mm, respectively.

Table 5.17. Analysis of variance for the bottom diameter of a through-hole located at the center of the polymer layer.

Source	DF	Adj SS	Adj MS	F-Value	P-Value
Molding Temperature	2	3660.35	1830.17	12231.36	0.001
Embossing Force	2	2319.38	1159.69	7750.40	0.001
Interaction	4	3398.26	849.56	5677.78	0.001
Error	18	2.69	0.15		
Total	26	9380.68			

Table 5.18. Analysis of variance for the bottom diameter of a through-hole located at 40 mm.

Source	DF	Adj SS	Adj MS	F-Value	P-Value
Molding Temperature	2	1904.05	952.02	460.82	0.001
Embossing Force	2	1721.37	860.68	416.61	0.001
Interaction	4	646.11	161.53	78.19	0.001
Error	18	37.19	2.06		
Total	26	4308.71			

The regression equations for the prediction of the bottom diameter at radial locations of 0 and 40 mm are presented in Equations 5.9 and 5.10, respectively. These equations could be used to predict the bottom diameter of the fabricated through-hole as a function of the molding temperature and the embossing force.

$$D_{b\,@0mm} = 739.2 + 0.091(Molding\ Temperature) + 1.79(Embossing\ Force) - 0.00913(molding\ Temperature * Embossing\ Force) \quad (5.9)$$

$$D_{b\,@40mm} = 787.5 + 0.165(Molding\ Temperature) + 0.322(Embossing\ Force) + 0.00067(molding\ Temperature * Embossing\ Force) \quad (5.10)$$

5.4. Summary

The Taguchi method was used to determine the S/N ratios and main effects of the factors and levels in the fabrication of through-holes. The molding temperature was identified as the main effect for the rollover diameter, top diameter, through-hole height, and bottom diameter. A molding temperature of 125°C reduced the variability of the measurement parameters leading to a reliable replication of through-holes in hot embossing.

The interaction effect between the molding temperature and the embossing force indicated that the two factor acting together significantly affected the advance of the polymer to fill the mold cavity. Leading to a more accurate replication of through-holes. Using a 95% confidence interval ($p > 0.05$), the molding temperature caused greater effect on the results of the measurement parameters. These results were correlated with the Taguchi orthogonal design.

6. MARKET OPPORTUNITY

6.1. Introduction

Diagnostic techniques are a critical component in life and health sciences. Microfluidic devices are systems designed to manipulate fluids on a microscale. Over the past decade, the microfluidic device technology has grown to develop Lab-on-a-Chip (LOC) devices. The ability to interconnect microfluidic devices would scale the functionality of microfluidic modular systems, fulfilling the gap between research and consumer market (Becker et al., 2002). However, replication technology for microfluidic devices is a critical feature to turn expensive microstructures into cost effective polymer devices.

Hot embossing has been proposed as suitable technology to fabricate through-holes allowing a fluidic sample to be transferred between multiple interconnected LOC devices. The development of a simulation tool that provides significant insight information for the fabrication of through-holes could have a positive impact in the manufacturing industry. The simulation tool could be used in the design and optimization of molding tools, microfluidic components, and process parameters without requiring additional testing.

In this chapter, the development of an initial approach on a business plan was discussed. The business plan was based on the development of a simulation tool capable of accurately analyzing the behavior of polymer substrates in the fabrication of micro fluidic devices.

6.2. The microfluidic market

Markets and Markets (2013), a market research company, estimated the market for polymer microfluidic devices at $2.6 billion for the United States and $8.53 billion worldwide in 2013. The polymer microfluidic devices industry is formed by three principal participants including pharmaceutical, in-vitro diagnostics, and drug delivery systems companies. In a market analysis study results indicated, the number of patent applications in microfluidic device technology has increased from 300 per year to around 4000 per year by 2013.

The estimated value of the microfluidics market was calculated based on the materials, (industry) products, and applications revenue. Based on materials, the market is classified into polymers, silicon, glass, and other materials. Based on industry, the market is classified into pharmaceutical, in-vitro diagnostics, and drug delivery devices.

The life science market can be divided into instrumentation, tools and service, clinical services, research devices, and medical supplies and consumables. The analytical tool segment is a broad category that require diagnostic devices at different scales. The segments of interest include testing devices and processes where microfluidic devices are the principal driver in the overall process. This is due to factors such as the rising demand for POC devices, quick return on investments provided by microfluidics devices which helps in cost reductions, and miniaturization of microfluidic chips.

Table 6.1. Principal companies in the polymer microfluidic device industry.

Name	Headquarters
Abbot Laboratories	Abbot Park, IL
Agilent Technologies	Santa Clara, CA
Caliper Life Sciences	Hopkinton, MA
Johnson & Johnson	New Brunswick, NJ
Life Technologies Corporation	Carlsbad, CA
Roche Diagnostics	Basel, Switzerland

However, factors such as difficulty in incorporation of emerging microfluidic technologies into existing workflows and complex and time consuming regulatory standards are hampering the growth of this market.

The patent application growth indicates an elevated adoption of microfluidic technology and the future opportunities in a competitive market for this emerging technology. This industry has a small number of participants, which are considered major players. Table 6.1 shows the principal companies in the microfluidics market. It is important to note that 5 out of 6 participants are located in North America, increasing the interest of the development of new technologies and adoption rates.

The large share of this segment is attributed to the increased adoption of microfluidics in Point-of-Care diagnostics by major diagnostic companies such as Roche Diagnostics (Switzerland), Becton Dickinson and Company (U.S.), Abbott Laboratories (U.S.), and Cepheid (U.S.).

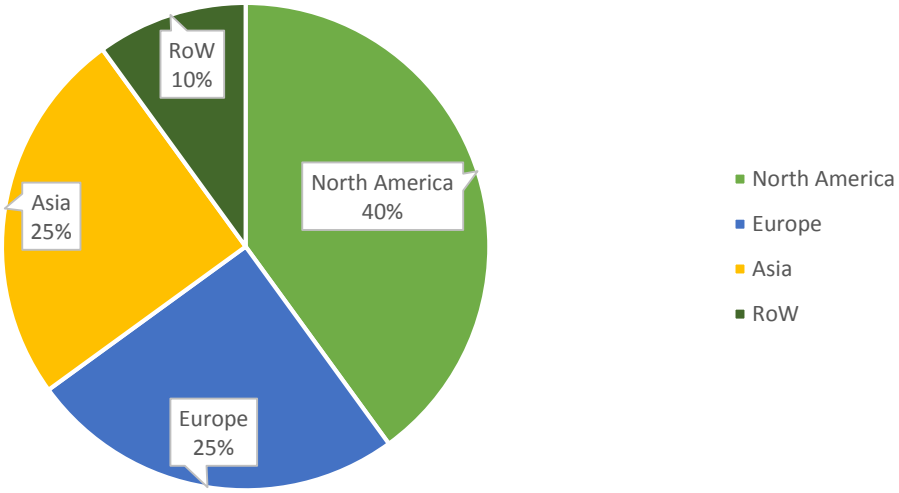

Figure 6.1. Microfluidic device market shares.

The polymer micro fluidic device market is predicted to grow 17.6 percent annually through the next five years with a total market size of $14 billion by 2016. North America dominates the market, accounting for 40% of the share as shown in Figure 6.1. The leading market share is attributed to the presence of large manufacturers in the region. Market growth could be directly attributed to an increasing demand for LOC devices, quick return on investments which help in cost reduction, and miniaturization of microfluidic chips. The microfluidic device market is segmented into materials, products, and applications.

6.3. Compliance

Microfluidic devices designed to be used in humans are considered medical devices under the Food and Drug Administration (FDA) approval process (Kroll, 2007). LOC devices manufactured for diagnostics, monitoring, surgical, and

therapeutic applications are covered must comply with the regulations established by the FDA (Bonnema, 2012).

7. CONCLUSIONS AND FUTURE WORK

7.1. Conclusions

The fabrication of through-holes for the interconnection of polymer microfluidic devices was investigated by FEA and hot embossing experiments. The effect of the process parameters was studied to determine the significance in the fabrication of thorough-holes. The Taguchi method was used to analyze the variation in the measurement parameters. S/N ratios were used to determine the relationship between the process parameters organized in an orthogonal array. The results of the statistical analysis were used to determine the main effect which led to the process parameter combination required for the reliable fabrication of through-holes.

A secondary polymer, PSU, was used as a buffer layer to reduce wear from the pins. The buffer layer could increase the replication fidelity and the life cycle of the mold insert. The buffer acted as a receptor for the pins as a result of its higher glass transition temperature (T_g) compared to PMMA.

Numerical analysis using DEFORM 2D, predicted the effect of the molding temperatures and embossing forces during embossing. Simulations at molding temperatures below T_g were not able to produce through-holes. Complete Through-holes were achieved at molding temperatures of 125 and 150°C and embossing forces of 10, 30, and 50 kN. The molding temperature significantly affected the advance of the flow front, allowing the pin to move into the polymer causing fracture of the residual layer.

The stress evolution and displacement of the polymer and the pin were investigated during cooling and demolding to analyze the effect of thermal stress and shrinkage on the fabricated through-hole. Simulation results predicted stress concentration at the bottom of the pin and at the contact area between the pin and the polymer.

Experimental trials in hot embossing correlated with the results of the simulations. Complete through-holes were observed at molding temperatures of 125 and 150°C, embossing forces of 10, 30, and 50 kN, and in polymers with a thickness of 0.8, 1.5, and 3.0 mm. Temperatures below T_g were not suitable to fabricate complete through-holes as observed in the results of the simulations and the results of experiments. The low molding temperature increased the flow resistance of the polymer, generating higher stress concentration on the pin that could lead to failure. Results of hot embossing showed that the pins were able to produce clean and round through-holes.

The Taguchi method was used to determine the S/N ratios and main effects of the factors and levels in the fabrication of through-holes. The molding temperature was identified as the main effect for the rollover diameter, top diameter, through-hole height, and bottom diameter. A molding temperature of 125°C reduced the variability of the measurement parameters leading to a reliable replication of through-holes in hot embossing.

Compared to previous hot embossing processes, this technique requires no alignment tools, which facilitates the manufacturing process, and introduces the capability of simultaneous through-hole fabrication in a single-operation process.

7.2. Future work

7.2.1. Hot embossing simulations

Simulations have been widely used for the design and consequent fabrication of components containing microfeatures including microfluidic devices. However, the process have not been thoroughly analyzed in regards of manufacturing processes and technologies. The fatigue of the mold insert could be included in future simulations. By doing so, life cycle analysis could be performed to determine the longevity of the mold in a manufacturing process. This could provide a critical insight on the development of cost-effective process parameters.

The integration of the microfluidic channel and the pin to fabricate through-hole in one single mold could reduce the manufacturing time. The ability to fabricate microfluidic devices containing interconnecting ports in hot embossing could be analyzed by FEA to determine the proper location of the through-hole.

7.2.2. Hot embossing experiments

Hot embossing experiments could be performed to validate the integration of the microfluidic channel with the through-hole developed in the simulations. A flow analysis should be executed to determine the flow characteristics and requirements for the microfluidic device. A surface roughness analysis of the through-hole should be included in future experiments to determine the flow characteristics of the fluid across the device. The effect of the process parameters could be studied as well.

Finally, to develop the complete implementation of a functional microfluidic device, microscale injection molding should be considered in FEA and experiments to scale up the manufacturing process of through-holes.

REFERENCES

Becker and Locaicio 2002. Polymer microfluidic devices – review. Talanta **56** 267-287.

Bonnema, Lisa. "Accelerating Medical Accuracy." Electronic Controls and Embedded Systems. Appliance Magazine, Sept. 2012.

Chen, You, Park, Park, Nikitopoulos, Soper, and Murphy 2006 Replication of reliable assembly features for polymer modular microfluidic systems *Proc. IMECE 2006.*

Chou, Du, Ou, Floriano, Chirstodoulides, and McDevitt 2013 Hot embossed polyethylene through-hole chips for bead-based microfluidic devices *Biosensors and Bioelectronics* **42** 653-660.

Chun, You, and Song 2012 Injection Molding Analysis of a Needle Cover – Optimum Filling for Gate Location Design *Fibers and Polymers* **13** 1185-1189.

Chun, You, and Song 2012 Injection molding analysis of a needle cover – optimum filling for gate location design *Fibers and Polymers* **13** 1185-1189.

Dirckx and Hardt 2011 Analysis and Characterization of Demolding of Hot Embossed Polymer Microstructures *J. Micromech. Microeng.* **21** 085024.

Dyer, Waldeck, and Roberts 1997 Fine-hole drilling in upilex polyimide and glass by TEA CO_2 laser ablation *J. Phys. D: Appl. Phys* **30** L19-L21.

Farshchian, Amirsadeghi, Hurst, Kim, and Park. 2012. Deformation behavior in 3D molding: experimental and simulation studies. *J. Micromech. Microeng.* **22** 115027.

G'Sell, Souahi 1997 Influence of Crosslinking on the Plastic Behavior of Amorphous Polymers at Large Strains *J. Eng. Mater. Technol.* **119** 223-227.

Gomez, Conner, Chun, Kim, Song, and You 2014 Mold Filling Analysis of an Alignment Structure in Micro Hot Embossing *Fibers and Polymers* **15** 1197-1201.

Gomez, Conner, Song, Chun, Kim, and You 2012 Cavity Filling Analysis for the Fabrication of an Alignment Structure in Micro Hot Embossing *Proc. IMECE 2012* IMECE2012-88441.

Gomez, Conner, Song, Kim, and You 2013 Finite Element Analysis for Reliable Replication of Alignment Structures in Micro Hot Embossing *Proc. IMECE 2013* IMECE2013-64829.

Gomez, Lek, Song, Chun, and You 2014 Study on Stress and Thermal Contraction During Cooling and Demolding in Hot Embossing *Proc. IMECE 2014* IMECE2014-39203.

Guo, Liu, Xiong, and Tian 2006 Study of the demolding process – implications for thermal stress, adhesion and friction control*. J. Micromech. Microeng.* **17** 9-19.

Gurung 2007 Passive alignment of micro-fluidic chips using the principle of elastic averaging *Master Dissertation* Louisiana State University, Baton Rouge, LA.

He, Fu, and Chen 2007 Research on Optimization of the Hot Embossing Process *J. Micromech. Microeng.* **17** 2420-2425.

Heckele and Schomburg 2004 Review on Micro Molding of Thermoplastic Polymers *J. Micromech. Microeng.* **14** R1-R14.

Heckele, Bacher, and Muller 1998 Hot Embossing – The Molding Technique for Plastic Microstructures *Microsystem Technologies* **4** 122-124.

Heyderman, Schift, David, Gobrecht, and Schweizer 2000 Flow Behavior of Thin Films Used for Hot Embossing Lithography *Microelect. Eng.* **54** 229-245.

Hirai, Konishi, Yoshikawa, and Yoshida. 2004. Simulation and experimental study of polymer deformation in nanoimprint lithography. *J. Vac. Sci. Technol.* **B 22.**

Horng, Han, Chen, Lin, Tsai, and Zen 2005 PMMA-based capillary electrophoresis electrochemical detection microchip fabrication *J. Micromech. Microeng.* **15** 6-10.

Jin, Gao, Liu, Tan, Wang, and Zhou 2009 Simulation and Experimental Study on Recovery of Polymer during Hot Embossing *Japanese Journal of Applied Physics* **48** 06FH10.

Joo, Oh, and Jeon 2001 Development of Micro Punching System *CIRP Ann* **50** 191-4.

Joo, Rhim, and Oh 2005 Micro-hole fabrication by mechanical punching process *Journal of Materials Processing Technology* **170** 593-601.

Joudkazis and Misawa 2004 Controlled through-hole ablation of polymer microspheres *J. Micromech. Microeng.* **14** 1244-1248.

Juang, Lee, and Koelling 2002 Hot Embossing in Microfabrication. Part I: Experimental *Polymer Engineering and Science* **42** 539-550.

Juang, Lee, and Koelling 2002 Hot Embossing in Microfabrication. Part II: Rheological Characterization and Process Analysis *Polymer Engineering and Science* **42** 551-566.

Kim, Yamanaka, and Altan 2004 Prediction and elimination of ductile fracture in cold forgings using FEM simulations *Scientific Forming Technologies* **103.**

Kroll, Mark W. ICD Using MEMS for Optimal Therapy. Pacesetter, Inc., assignee. Patent US 7,181,281. 20 Feb. 2007.

Kwon, Kang, Chun, and Youn 2001 Prediction and measurement of residual stresses in injection molded parts *Fibers and Polymers* **2** 203-211.

Li, Liu, Dai, Chen, Liang, Sun, Tian, and Ding 2006 PMMA microfluidic devices with three-dimensional features for blood cell filtration *J. Micromech. Microeng.* **18** 095021.

Luo, Xu, Wang, and Liu 2006 Finite Element Analysis of PMMA Microfluidic Chip Based on Hot Embossing Technique *J. Phys.: Conf. Ser.* **48** 1102-1106.

Markets and Markets 2013 Microfluidics Market By Materials (Polymers, Silicon, Glass), Pharmaceuticals (Microreactors, Toxicity Screening, Lab on Chip, Proteomic & Genomic Analysis) Drug Delivery Devices (Microneedles, Micropumps), IVD (POC) - Global Trends & Forecast to 2018.

Omar, Brousseau, Elkaseer, Kolew, Prokopovich 2014. Development and experimental validation of an analytical model to predict the demoulding force in hot embossing. *J. Micromech. Microeng.* **24** 055007.

Pan, Wu, Tsai, Chou, and Wu 2008 Fabrication of a micro-punching head using LIGA and stacking processes *J Micromech. Microeng.* **18** 095012.

Park, Song, Brumfield, Amirsadeghi, and Lee 2009 Demolding Temperature in Thermal Nanoimprint Lithography *Appl Phys A* **97** 395-402.

Rapp, Schneider, and Worgull 2009 Hot punging on an 8 inch substrate as an alternative technology to produce holes on a large scale *Microsyst Technol* **16** 1201-1206.

Roy 2010. A primer on the Taguchi method. Society of Manufacturing Engineers. Second Edition, USA.

Song, You, Lee, and Park 2008 *Microsyst. Technol.* **14** 1593.

Taguchi and Konishi 1993 Taguchi Methods – Design of Experiments. The American Supplier Institute. Tokyo, Japan.

Taylor, Boning, and Iliescu 2011. A razor-blade test of the demolding energy in a thermoplastic embossing process. *J. Micromech. Microeng.* **21** 067002.

Werner 2005 Hot Embossing of Through-holes in Cyclo-Olefin Copolymer (TOPAS®) *Diploma Thesis* University of applied sciences Oldenburg.

Worgull 2009 Hot Embossing, Theory and Technology of Microreplication *Micro & Nano Technologies* 137-147.

Worgull and Heckele 2004 New Aspects of Simulation in Hot Embossing *Microsystem Technologies* **10** 432-437.

Worgull, Hetu, Kabanemi, and Heckele 2006 Modeling and Optimization of the Hot Embossing Process for Micro and Nanocomponent Fabrication *Microsyst. Technol* **12** 947-952.

Xu, Guo, Shan, Wang, Li, Liu, and Qu 2012 Development of a micro-system for micro-punching of micro-hole arrays in brass foil *Journal of Materials Processing Technology* **212** 2238-2246.

Yao, Virupaksha, and Kim 2005 Study on Squeezing Flow During Nonisothermal Embossing of Polymer Microstructures *Polymer Engineering and Science* **45** 652-660.

You, Chen, Park, Park, Nikitopoulos, Soper, and Murphy 2009 Passive micro-assembly of modular, hot embossed, polymer microfluidic devices using exact constraint design *J. Micromech. Microeng.* **19** 120525.

Young 2005 Analysis of the Nanoimprint Lithography with a Viscous Model *Microelectronic Engineering* **77** 405-411.

Zhang, He, and Fu 2011 Simulation Research on Stress of Polymeric Patterns During Micro Hot Embossing *Applied Mechanics and Materials* **80** 339-345.

Zhu and Cui 2011 Fabrication of polymer via holes by a combination of hot embossing and indentation processes *J. Micromech. Microeng.* **21** 045032.